FORMATION FLIGHT
OF EARTH SATELLITES
ON KAM TORI

THESIS

Christopher T. Craft, First Lieutenant, USAF

AFIT/GA/ENY/09-S01

DEPARTMENT OF THE AIR FORCE

AIR UNIVERSITY

AIR FORCE INSTITUTE OF TECHNOLOGY

Wright Patterson Air Force Base, Ohio

AFIT/GA/ENY/09-S01

FORMATION FLIGHT OF EARTH SATELLITES ON KAM TORI

THESIS

Presented to the Faculty of the

Department of Aeronautics and Astronautics

Graduate School of Engineering and Management

Air Force Institute of Technology

Air University

Air Education and Training Command

in Partial Fulfillment of the Requirements for the

Degree of Master of Science in Astronautical Engineering
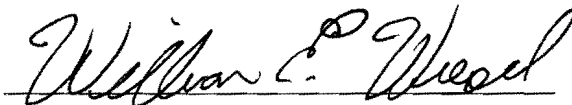
Christopher T. Craft, B.S.

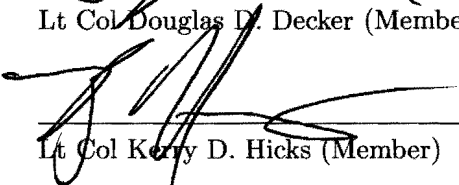First Lieutenant, USAF

September 2009

FORMATION FLIGHT OF EARTH SATELLITES ON KAM TORI

Christopher T. Craft, B.S.

First Lieutenant, USAF

Approved:

_____ _____
Dr. William E. Wiesel (Chairman)   Date   31 Aug 09

_____ _____
Lt Col Douglas D. Decker (Member)   Date   31 Aug 09

_____ _____
Lt Col Kerry D. Hicks (Member)   Date   31 Aug 09

AFIT/GA/ENY/09-S01

Abstract

Komolgorov, Arnold and Moser (KAM) theory provides that orbits of satellites whose dynamics are representable by an integrable Hamiltonian plus a small, real perturbation lie on tori in phase space and remain upon the KAM tori for all time, unless acted on by a non-conservative force. A refined technique for constructing KAM tori for Earth-orbiting satellites is developed and implemented using numerically integrated orbital data for hypothetical satellites and involving methods of Fourier analysis and spectral decomposition. Definition of satellite formations on the KAM tori is performed and analyses conducted to investigate both constellations with large separations and clusters with small separations. Cluster formations with physical secular drift rates on the order of nanometers to micrometers per second are obtained. A brief discussion of effects of non-conservative forces (such as atmospheric drag) on KAM tori is given.

Acknowledgements

"Contemplate the workings of this world, listen to the words of the wise, and take all that is good as your own. With this as your base, open your own door to truth. Do not overlook the truth that is right before you."

-Morihei Ueshiba Sensei

List of Figures

x

List of Abbreviations

FORMATION FLIGHT OF EARTH SATELLITES ON KAM TORI

I. Introduction

There is no question that the advent and utilization of Earth-orbiting satellites in the last half century has afforded the human race unprecedented benefits and enhancements in almost every aspect of its increasingly technologically-based existence. Among the facets of modern humanity most profoundly affected by satellite-based technology are communications, navigation, surveillance and reconnaissance, geographic analysis and deep space exploration.

1.1 *Motivation*

In many applications of satellite technology, the relative motion between two or more separate entities orbiting about a primary body is increasingly vital. This has become all the more apparent with the relatively recent focus on development and implementation of small satellite or microsatellite formations – groups or systems of smaller, less expensive satellites designed to perform or improve the function of a previous larger, more expensive satellite – for scientific, commercial and military purposes.

Current methods of determining satellite relative motion and designing satellite constellation orbits typically employ only estimates of the true orbital dynamics, to include the two-body motion along with the harmonic terms of Earth's gravitational potential to perhaps degree/order m,n = 4 (see sections 2.1 and 2.2.1). While the truncation of the potential is sometimes necessary due to computational complexity, especially during long numerical integrations, it causes an increase in residual error over time due to the ignored higher-order gravitational harmonic contributions, except in very specific cases. A definite accuracy advantage could obviously be realized in orbit design if there exists a way of describing more fully and accurately the flight dynamics of the satellite about the primary.

1

1.2 Approach

In the course of this work, the author attempts to demonstrate that, using the concepts and results of KAM theory, it is possible to significantly enhance the effectiveness of satellite formation orbit design. This stems in large part from the fact that one can achieve a better representation of the true dynamics of a satellite's orbit by using KAM theory. According to the Kolmogorov, Arnold and Moser (KAM) theorem, the solution of a near-integrable Hamiltonian system will lie on an invariant torus in the phase space ([1],[8],[15]). In the case of Earth-orbiting satellites, if one assumes that the only perturbations away from the integrable two-body problem (2BP) experienced in the orbit stem from Earth's gravitational field harmonics (i.e. that nonconservative perturbations and non-primary potential effects such as third-body interactions are zero), it has been demonstrated that the satellite's motion may indeed lie on a so-called KAM torus for both observed satellite data and integrated orbital data ([24], [25],[11]).

This work will proceed by first demonstrating the determination of KAM tori representing various Earth satellite orbits in the presence of the Earth's extended gravitational potential. This will be accomplished using techniques based upon those outlined in previous works by Laskar in [9],[10] and Wiesel in [24],[25] . The application of KAM theory to satellite formation flight will then be investigated by exploring satellite relative dynamics on calculated KAM tori.

1.3 Problem Statement

Given the previously demonstrated strong probability of the existence of a KAM torus upon which each satellite's orbit is constrained, the application of KAM theory to satellite formation flight naturally arises. If the dynamics of earth orbits are indeed accurately represented by KAM tori, the investigation of the relative motion of two individual satellites constrained to separate but proximate locations on the same KAM torus should demonstrate acceptably small secular drift between the bodies during orbital propagation.

1.4 Results

The current work demonstrates that KAM tori may be constructed to represent orbits with unprecedented accuracy given certain constraints and accurate enough trajectory information. Additionally, largely separated formations of satellites with secular drifts on the order of 0.5 percent of the original separation distance over 10 days are demonstrated for multiple orbit altitude and inclination combinations under the influence of the geopotential expansion to order and degree 20. Tight formations analyses yield secular drift rates between satellites on the order of 4 nanometers to 1 micrometer per second.

II. Background

This chapter will briefly investigate the current methods of analysis of satellite formations/constellations. Then, exposition of the major perturbations experienced by satellites in Earth orbit will be given. A description and short history of KAM theory will be provided. Finally, the chapter will end with an introductory explanation of the formulation of the dynamics used throughout the rest of the work.

2.1   Satellite Formations and Relative Motion

One of the first methods developed for the description of satellite relative motion, and that which is predominantly used in the design of rendezvous missions and satellite formations, involves using the Hill-Clohessy-Wiltshire (HCW) equations, created originally for the Gemini Program [2]. These equations are given in the relative frame as

$$\ddot{x} - 2\omega\dot{y} - 3\omega^2 x = f_x \tag{2.1}$$

$$\ddot{y} + 2\omega\dot{x} = f_y \tag{2.2}$$

$$\ddot{z} + \omega^2 z = f_z \tag{2.3}$$

where x, y and z are the coordinates in the target-centric frame, ω is the orbital angular velocity of the chief satellite (which is equivalent to the mean motion n in this circular case) and the f_n are external forces [19]. These equations are the result of the investigation of the relative motion between a 'chief' (or 'target') spacecraft and a 'deputy' (or 'chaser') spacecraft, after ignoring nonlinear gravity terms and assuming the chief is in a circular orbit [19].

In their original form, the HCW equations provide an acceptable depiction of spacecraft relative motion to first order when the satellites in question are relatively close to one another. It is commonly known that the most potent perturbative effect not included in these linearized HCW equations is due to the terms in the geopotential expansion containing potential forces higher than zeroth order two-body motion. There have been a variety of techniques used to combat this source of error, ranging from designing orbit constellations which are essentially invariant to higher-order geopotential terms [17] to

modifying the HCW equations to include the higher-order terms to some degree, usually only including the coarsest oblateness effect, or J_2 zonal harmonic term (c.f. §2.2.1 for a more detailed explanation of the geopotential field's effects). Some missions, such as the canceled USAF TECHSAT 21, were to use formations that were "close enough" to remain within the linear regime of the HCW equations [12]. Modified versions of the HCW equations, including both Earth J_2 harmonic effects and nonlinear differential gravity effects, have been developed (as in [6],[18]) and applied to obtain better approximations over larger separating distances and have allowed for more efficient orbital designs – i.e. orbit designs which require fewer on-orbit corrections (and, thus, less fuel) to stay within certain relative position constraints. However, it is certainly preferable, if the possibility exists, to more accurately represent the true dynamics of the satellites' respective motions around the primary. This would enable the 'capture' of all nuances of the primary's influence which would cause secular growth in the separation between the orbiting bodies.

2.2   Perturbations in Earth-orbit

Satellites in orbit around the Earth experience a number of perturbations which tend to force their dynamics away from those which can be precisely described by typical Keplerian two-body motion. The types of perturbations which are dominant depend upon the altitude of the satellite above the Earth's surface. Objects in low-Earth orbit (LEO - up to about 800 km altitude) mostly experience conservative perturbative forces due to Earth's nonsphericity, along with the non-conservative force due to atmospheric drag. Conversely, objects in mid-Earth orbit (MEO – 800km to 30,000km altitude) and geosynchronous orbit (GEO – 35,780km altitude) experience relatively little perturbative force from Earth's nonsphericity, as the Keplerian term dominates at high radii, and relatively little resistive force from atmospheric drag, which falls off exponentially with altitude. Rather, as a satellite's altitude increases, its perturbations away from Keplerian become dominated by third-body effects from the Sun and Moon and by the non-conservative force imparted by as solar radiation pressure. This thesis will focus solely on satellites in LEO and mainly upon the effects of the geopotential, although atmospheric drag will be discussed in brief; hence, the dynamics of bodies in MEO, GEO and above are beyond the scope

of this thesis; however, the methodology developed and applied here may be extended to arbitrary potential fields which meet the KAM criteria as mentioned below and in Chapter III, and would hence, in theory, be applicable to Earth orbit classes including third body effects, given adequate trajectory knowledge.

2.2.1   The Earth's Geopotential.   This subsection provides a general overview of the geopotential field through discussion of the terms in the geopotential expansion. For a full treatment of the geopotential, c.f [19] and [23].

The derivation of the geopotential expansion around a solid body may begin with the familiar *Poisson's equation* for the gravitational potential V:

$$\nabla^2 V = 4\pi G\rho \qquad (2.4)$$

where G is the gravitational constant, ρ is the density of the body and $\nabla^2 = \nabla \cdot \nabla$ is the standard Laplacian operator. After evaluating Poisson's equation in spherical coordinates (c.f. [23]) for positions outside of the gravitating body, the potential becomes

$$V = -\frac{\mu}{r}\sum_{n=0}^{\infty}\sum_{m=0}^{n}(\frac{r}{R_\oplus})^{-n}P_n^m(sin\delta)\left[C_{nm}cos(m\lambda) + S_{nm}sin(m\lambda)\right] \qquad (2.5)$$

which is termed the "expansion of the geopotential in spherical harmonics", and in which μ is the gravitational parameter, r is the radius of the satellite from the Earth's center, $R_\oplus$ is the radius of the Earth, n and m are the degre and order of the expansion (respectively), P_n^m are the associated Legendre polynomials, C_{nm} and S_{nm} are the gravity field coefficients given by an Earth-gravity model, δ is the geocentric latitude and λ is the east longitude. The potential given in Eq. (2.5) may be most intuitively considered as a combination of three types of effects: zonal, sectoral and tesseral harmonics.

2.2.1.1   Zonal Harmonics.   Zonal harmonics are encountered when order m = 0 and $1 \leq n \leq n_{max}$. The first zonal harmonic, $n = 1$, has the effect of moving the center of mass of the geoid north or south; as such, it is not usually included in Earth geopotential models, since we desire the center of our coordinate system to coincide with

the center of mass. The first nonzero zonal harmonic term, then, occurs when $n = 2$; this term accounts for the direct oblateness (or equatorial bulge) of the Earth due to its spin about the 3-axis. The potential associated with $n = 2$, $m = 0$ then assumes the form

$$V_{20} = \frac{\mu R_{\oplus}^2 J_2}{2r^3}(3cos^2\theta - 1), \tag{2.6}$$

where J_2 is the C_{20} coefficient, with a value ≈ 0.001082. This effect is the second largest in magnitude, with a value of approximately one thousandth of the Newtonian potential term $-\frac{\mu}{r}$ (where $n, m = 0$). Increasing the order while maintaining a zero degree represents zonal harmonic functions with successively more "nodes", which in turn allows for the increasingly refined modeling of mass distribution irregularities. This idea of zonal harmonics is shown pictorially in Figure (2.1), with both side and top views, for $n = [2, 6]$.

    2.2.1.2 Sectoral Harmonics. The sectoral harmonics describe the effect that occurs when $n = m$. The associated Legendre polynomials $P_n^n[sin(\delta)]$ have zeros only when $\delta = \pm\pi$, i.e. when the satellite is over the poles. The field terms $cos(m\lambda)$ and $sin(m\lambda)$ are zero at $2m$ lines of longitude λ around the geoid; hence, the sectoral harmonics divide the globe into slices, much like a typical beach ball's colored panels. The $n, m = 1$ term is set to zero, since it has the effect, as the analogous term in the zonal harmonics, of shifting the planet's center of mass away from the center of our coordinate frame. The C_{22}, S_{22} sectoral harmonic then separates the earth into four slices: two slices opposite each other with higher potential and two slices opposite each other with lower potential. As was the case regarding the zonal harmonics, increasing the order and degree divides the Earth into higher and higher "resolution" slices. Figure (2.2) shows sectoral harmonics for $n, m = 2$ and $n, m = 3$.

    2.2.1.3 Tesseral Harmonics. Tesseral harmonics refer to the "off-diagonal," non-zonal terms: those determined by $n \neq m$, where $n, m > 0$. The potential contributions from tesseral harmonics are due to mass distribution differences manifested in a tiled or grid pattern. In general, much as before, the higher the degree and order of the expansion,
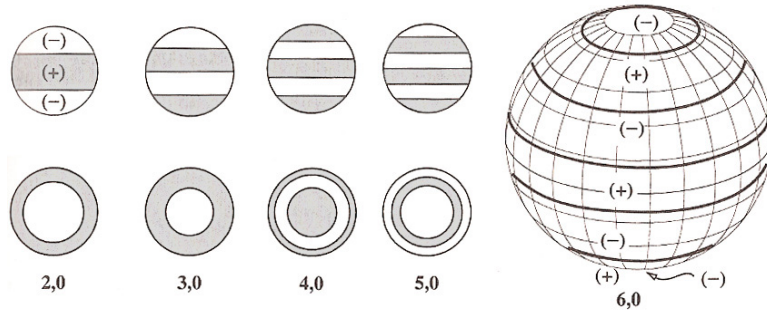
Figure 2.1.   Depiction of Zonal Harmonics (from ref. [19]).
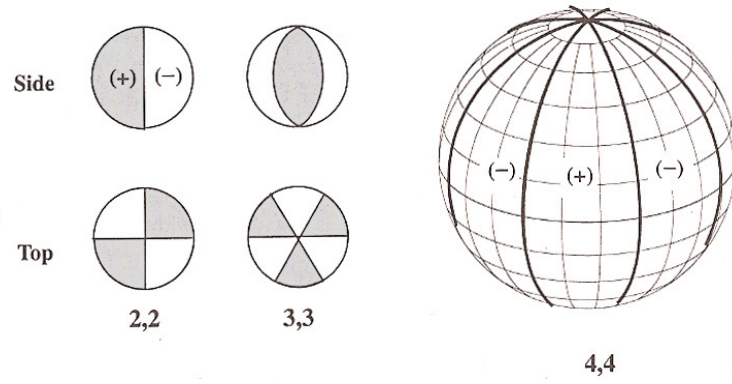
Figure 2.2.   Depiction of Sectoral Harmonics (from ref. [19]).
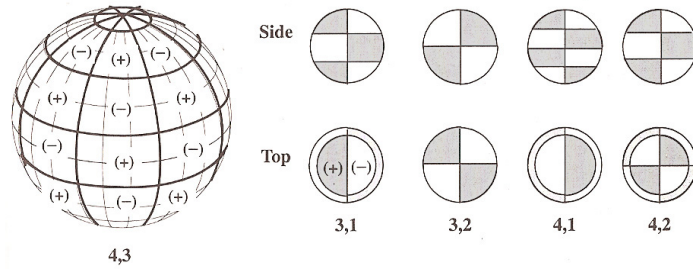
Figure 2.3.   Depiction of Tesseral Harmonics (from ref. [19]).

the 'finer' the grid and the higher the resolution of the gravitic model. Figure (2.3) shows representative examples of tesseral harmonics for $m = 3, 4$ and $n = [1, 3]$.

2.2.1.4 Earth Gravity Model.   To obtain a usable geopotential expansion, the C_{nm} and S_{nm} coefficients must be empirically determined. This has been accomplished using satellites instrumented with highly accurate equipment capable of detecting and documenting very small perturbations in the satellites' motion due to differential gravity forces. Such a set of coefficients is termed a *gravity model*. The current standard gravity model, complete to order and degree 360, is called the *Earth Gravity Model of 1996* (EGM96) [19]. The EGM96 is highly accurate and has been augmented and verified using data from multiple satellites. Although the model includes terms up to order/degree 360, the current work uses only terms to $m, n = 20$ in order to decrease computational burden while still maintaining very high accuracy; recall the steep decline of the potential magnitude as order and degree increase.

2.2.2 Orbital Atmospheric Drag.   As mentioned above, the main source of dynamical perturbation for satellites in LEO aside from the Earth's nonsphericity is atmospheric drag. The current work is concentrated on the KAM tori resulting from the conservative perturbations due to the geopotential; thus, only a brief discussion of the drag effects and their associated inclusion into KAM theory will be given.

Atmospheric drag manifests as a non-conservative force on a satellite, in a direction opposing that of the satellite's velocity vector and with a magnitude which depends on several key physical parameters of the satellite and its altitude. A standard form of the drag force equation on a satellite is given as

$$\bar{f}_d = -\frac{1}{2} C_d A \rho \left| \bar{V}_{rel} \right| \bar{V}_{rel} \tag{2.7}$$

where C_d is the drag coefficient of the satellite, A is its cross-sectional area, ρ is the atmospheric density at the position of the satellite and $\bar{V}_{rel}$ is the velocity of the satellite relative to the local atmosphere. Often, however, it is convenient to rewrite the drag effect

as an acceleration, rather than a force:

$$\bar{a}_d = -\frac{1}{2}\frac{\rho}{\beta}\left|\bar{V}_{rel}\right|\bar{V}_{rel} \tag{2.8}$$

In Eq. (2.8), β is known as the *ballistic coefficient* and is given in terms of the above parameters and the satellite mass m by

$$\beta = \frac{m}{C_d A} \tag{2.9}$$

so that a larger ballistic coefficient is, of course, preferable when possible, since it reduces the overall effect of drag on the orbiting vehicle.

The drag force on a satellite is often one of the most difficult aspects of the dynamics to predict, largely because of the density term, ρ. The density varies not only with altitude but can vacillate wildly with respect to solar activity; that is, in periods of maximum solar flux, the atmosphere reaches a state of excitement in which the atmosphere can expand to encompass a much larger volume and hence leads to a greater apparent density at any particular altitude.

The effects of drag on a satellite orbit can be quite profound. In the case of a satellite with an elliptical orbit, increased drag at its periapsis will cause a lowering of the apoapsis altitude in an effect termed "circularization," with only a slight lowering of the periapsis altitude. This phenomenon will continue until the orbit is virtually circular, at which time the semi-major axis a will continue to decrease, lowering the orbital altitude until the satellite disintegrates or impacts the planet's surface. Figure (2.4) below shows the lifetime of an example 320km altitude orbit inclined at $i = 30°$ with a nearly zero eccentricity, for a satellite with a ballistic coefficient of $\beta \approx 318$ (corresponding to $m = 500kg$, $A \approx 0.785m^2$ and $C_d = 2$; see §4.3 for more detailed discussion regarding inclusion of drag in numerical integration). The reason for the nonlinear decline after a certain point in the orbit's decay is due to a simple aerodynamic phenomenon: as the atmospheric density grows exponentially with descent, the drag force bleeds energy from the system and causes the satellite to lower ever faster until impact .
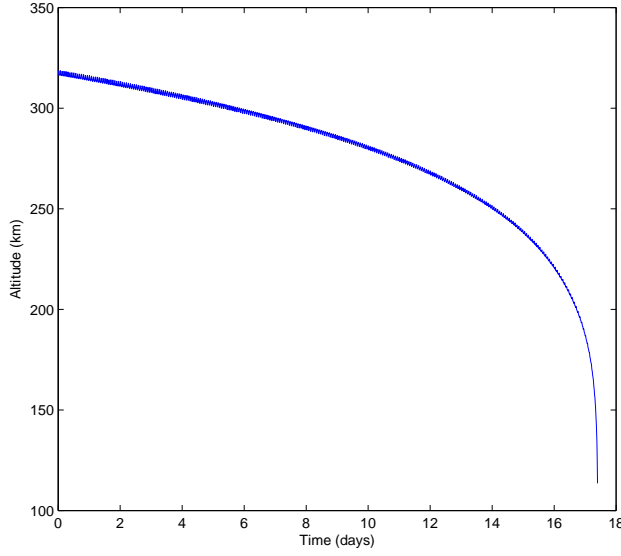
Figure 2.4.   Example of orbital decay due to atmospheric drag for a nearly circular orbit at 320km, $i = 30°$

Certain of the orbits examined in the current work are circular with initial altitudes on the order of 320km. The author notes that satellites in such orbits will not, without further boosting, have lifetimes significant enough to apply KAM theorem. However, they are utilized in the current work because, with respect to KAM modeling in the conservative perturbations, they represent a sort of "upper bound"- i.e. a satellite at 320km will be experiencing the full effect of the geopotential perturbations; thus, it stands to reason that if such a "worst case" can be accurately modeled using KAM theorem while ignoring drag, it should be possible to extend the methodology to less perturbed, higher altitude orbits with no loss of accuracy. See Chapters III and IV for details regarding the methodology and results for varying orbit parameters.

2.3 KAM Theory

The theorem posited by Kolmogorov [8], and later proved by Arnold [1] and Moser [15] possesses the possibility for far-reaching application in classical mechanics. Celletti and Chierchia have shown that KAM theory serves to adequately describe the dynamics of celestial bodies [3] and have also applied it to the dynamics of the Sun-Jupiter-Victoria sys-

11

tem, which is a Restricted, Circular, Planar Three Body Problem (RCPTBP) [4]. McGill and Binney have demonstrated development of KAM tori to model dynamical systems in generalized potentials with promising results, as in [13]. Kaasalainen and Binney have shown KAM torus development in Stäckel potentials and in loop and box orbits [7]. Additionally, KAM theory has been utilized in the field of quantum mechanics to describe the motion of particles in magnetic potentials, such as those experienced in a particle accelerator (c.f. [5], [20],[21] and [22]).

KAM theory has newly been applied to Earth-orbiting satellites by Wiesel in [24] and [25] and Little in [11]. Wiesel demonstrated a least-squares method for obtaining KAM tori from numerically integrated data in [24], where he showed the torus construction for an Earth satellite, and later a refined method using Fourier analysis in [25], where he showed the construction of a torus for a restricted three body problem resembling the Earth-Moon system. Little employed observed data from the *GRACE* and *Jason-1* satellites to show that Earth satellites likely lie on KAM tori [11].

As mentioned in §1.2, KAM theory, at its core, concerns the dynamical behavior of a system describable as an integrable Hamiltonian subject to some small perturbation; i.e.

$$H_\epsilon(I, \varphi) = H_0(I) + \epsilon H_1(I, \varphi) \tag{2.10}$$

where H_ϵ is the perturbed Hamiltonian, I and φ are the coordinates in an Action-Angle representation, H_0 is the integrable Hamiltonian, H_1 is the perturbing Hamiltonian and ϵ is some small, real value. H_0 and H_1 must be smooth, real-analytic functions. According to KAM theory, the motion of a body in a system which satisfies these conditions will lie on a torus in the system's phase space; i.e. the motion is 'constrained' to some locus of points in the phase space. The dimension of the torus depends upon the number of degrees of freedom of the system: Hamilton-Jacobi theorem mandates that, for a Hamiltonian with N degrees of freedom, the associated KAM torus is N-dimensional and occupies a phase space of $2N$ dimensions.

2.3.1   On The Visualization of Tori.   One may think of tori topologically as the products of circles; i.e.:

$$\mathbb{T}^n = \underbrace{S^1 \times S^1 \times \ldots \times S^1}_{n} \tag{2.11}$$

where S is a topological space which is the subspace $\left\{ (x_1, x_2) \in \mathbb{R}^2 : x_1^2 + x_2^2 = 1 \right\}$ of $\mathbb{R}^2$. Tori of dimensions 1 and 2 are then rather easily visualized; a 1-torus is simply a circle – a 1-dimensional torus existing in 2-dimensional space. For example, $\mathbb{T}^1$ is depicted in Figure (2.5) below. The 2-torus, then, is a shape similar to a donut: a 2-dimensional torus existing in 4-dimensional space, for one needs four parameters to define a point on its surface- two actions I_k and two angles φ_k (c.f. figure (2.6)). KAM tori manifest in shapes topologically similar to this when one examines systems with two degrees of freedom, such as the restricted three-body problem.
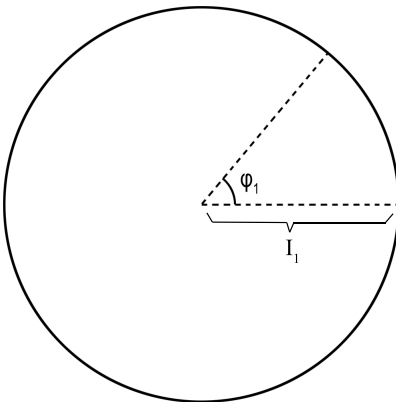
Figure 2.5.   Example of a 1-torus.

Tori of higher dimensions ($\mathbb{T}^n, n \geq 3$) are much more difficult for us to visualize, and so we must be satisfied with describing them almost entirely in the language of mathematics. However, one can obtain a very basic idea of system behavior by investigating higher-dimensional tori using a method loosely reminiscent of Henri Poincare's well-known "method of sections:" in the case of an invariant 3-torus (such as those examined in the current work), if one ignores one of the angle coordinates and its associated action, one can obtain a two-dimensional "projection" of the 3-torus in the form of 2-torus. Of course,
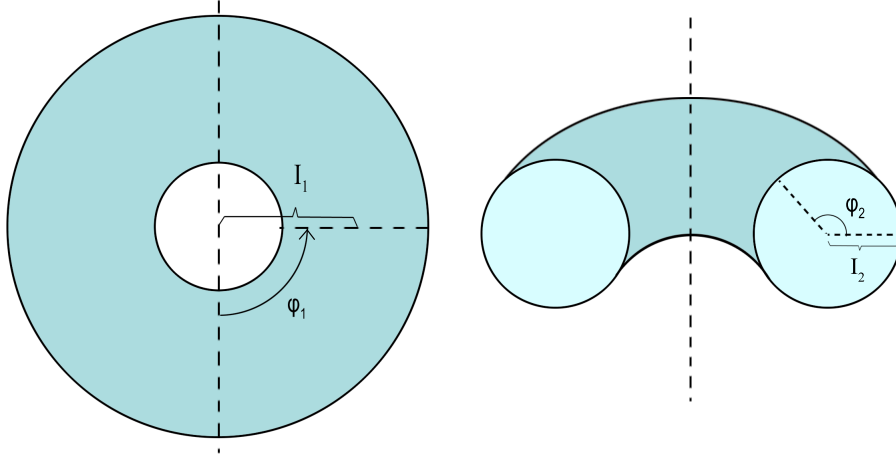
Figure 2.6.   Top(left) and perspective (right) views of a 2-torus.

the amount of information one gains from such an exercise is only useful insomuch as it provides a very general idea of torus action proportions and frequency trends. Shown below in Figure 2.7 is such a 2-torus "projection" obtained during the present work for a KAM 3-torus of an Earth-orbiting satellite, where the smallest frequency and its associated action are ignored.
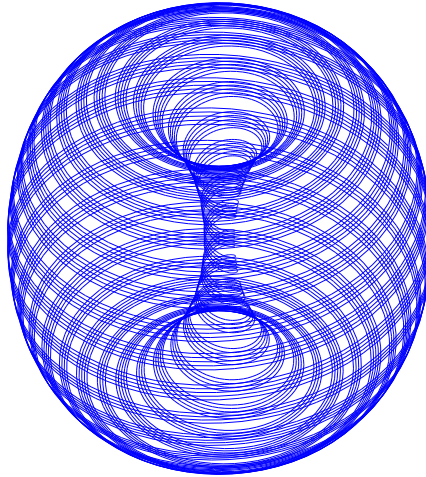
Figure 2.7.   Example of a 2-toroidal "projection" of the KAM 3-torus for an Earth-orbiting satellite.

2.4   Dynamics Formulation

In order to choose an appropriate coordinate frame in which to formulate the system dynamics and construct KAM tori, one must strive to find the frame which affords the largest number of integrals of the motion. In the general case (posed in Cartesian coordinates in an inertial frame) of a satellite moving in Earth's full potential field, there are no integrals of the motion readily available. However, we may find a constant of the motion in this case by choosing a frame which rotates with the Earth- namely, the Earth-centered rotating frame, also called the Earth-centered, Earth-fixed (ECEF) frame, in which the 1-axis points from the center of the earth through the intersection of prime meridian and the equator, the 3-axis points along the axis of rotation, and the 2-axis completes the right-handed orthonormal basis. In the ECEF frame, the elements of nonsphericity which cause the differential gravitational contributions in the Earth's potential are fixed; i.e., the position vector of a specific infinitesimal piece of the Earth's mass will always remain constant. We take advantage of this fortunate fact to greatly simplify our equations of motion. We begin our Hamiltonian formulation, following Wiesel [24], by writing the expressions for the specific momenta p_n as

$$p_x = \dot{x} - \omega_\oplus y \tag{2.12}$$

$$p_y = \dot{y} + \omega_\oplus x \tag{2.13}$$

$$p_z = \dot{z} \tag{2.14}$$

where x, y and z are the coordinates of the satellite in the ECEF frame and $\omega_\oplus$ is the angular rate of rotation of the Earth. We may then find the Lagrangian for the system

$$L = T - V \tag{2.15}$$

where T and V are the kinetic and potential energies, respectively. We can use the Lagrangian to calculate the Hamiltonian using:

$$H = \sum_i p_i \dot{q}_i - L \tag{2.16}$$

15

After substituting the appropriate expressions for kinetic and potential energies, the Hamiltonian may be written in its final form

$$H = \frac{1}{2}(p_x^2 + p_y^2 + p_z^2) + \omega_\oplus(yp_x - xp_y)$$
$$- \frac{\mu}{r} \sum_{n=0}^{\infty} \sum_{m=0}^{n} (\frac{r}{R_\oplus})^{-n} P_n^m(sin\delta)$$
$$\times [C_{nm}cos(m\lambda) + S_{nm}sin(m\lambda)] \tag{2.17}$$

where μ is the gravitational parameter, r is the radius of the satellite from the Earth's center, $R_\oplus$ is the radius of the Earth, P_n^m are the associated Legendre polynomials and C_{nm} and S_{nm} are the gravity field coefficients given by an Earth-gravity model, as described in the previous section. The radius r, the geocentric latitude δ and the east longitude λ of the satellite may be found by elementary geometry to be:

$$r = \sqrt{x^2 + y^2 + z^2}$$
$$sin\delta = \frac{z}{\sqrt{x^2 + y^2}}$$
$$tan\lambda = \frac{y}{x} \tag{2.18}$$

After following the above method, we may obtain the one achievable constant of the motion in this problem: the Hamiltonian. Again we note that this approach includes only the potential perturbations and ignores all non-conservative forces.

Throughout this work, a variety of units and constants are used in calculations and resulting displays. Most of the units are common, such as the standard degree, radian, meter and kilometer. A few are not quite so usual, such as the *time unit* (TU) and the *Earth radius* (ER). The values of these units and of assorted constants used throughout

this work are listed below [19]. Minutes and seconds given are in solar time.

$$1 \ TU = 13.446852 \ min$$

$$1 \ ER = 6378.137 \ km$$

$$\omega_\oplus = 0.0588335998 \ rad/TU$$

$$\mu_\oplus = 398600.4418 \frac{km^3}{s^2} = 1 \ ER^3/TU^2$$

III. Method

The core of utilizing KAM theory for orbital mechanics lies in calculating the KAM tori for orbits in question. This chapter will begin with a discussion of the process of application of KAM theorem to satellite orbits. It will then proceed with details of the methods used to obtain the requisite propagated orbital data. Finally, an explication of methodology used for formation analysis on the torus will take place.

3.1 Describing Orbits as KAM Tori

As mentioned before, the KAM torus for an Earth satellite exists as a 3-torus in 6-space in terms of three angle variables and their associated actions. However, in order to use orbital data to gain any utility from the concept of a KAM torus, we must find a formulation of the torus which involves the physical coordinates. Ideally, what we would seek is a map

$$\mathcal{M} : (q, p) \rightarrow (I, \varphi) \tag{3.1}$$

which would allow us ultimately to find the torus actions I_k and angles φ_k, having as the input a state containing the physical coordinates q_k and momenta p_k. Unfortunately, there does not seem to exist so simple a homeomorphism between the physical space and torus space. To circumvent this problem, we must obtain the states at a number of points along the orbital path (through satellite observation or numerical propagation) and perform an analysis upon these data to find two separate types of information: the *fundamental* or *basis frequencies* with which the system oscillates (which are related to the torus angle variables along with their temporal development) and the amplitudes with which each of the frequencies and combinations thereof manifest in the orbital motion (related to the torus actions). In an isoenergetic system (one where the only forces are conservative, or potential, forces), the torus actions I will be constant – indeed, one of the beauties of representing the dynamics as a torus is that the I_k are constant and the φ_k increment linearly with time. What is found through the below method, in fact, is the reverse of the map described above, manifested as a series involving torus parameters used to calculate physical coordinates and then their associated momenta.

3.1.1 KAM Series Representation. According to KAM theorem and Hamilton-Jacobi theorem, a nearly integrable system of 3 degrees of freedom (such as that in the current problem) should also have three fundamental frequencies, which, it has been established, are intimately related to the representative angle coordinates of the tori. Due to the conservative and nearly integrable nature of this system, and since we seek a function that is periodic in the angle variables φ_k, it is natural to seek a representation of the orbit coordinates as a Fourier series:

$$\bar{q}\left(\bar{I}, \bar{\varphi}\right) = \sum_{\bar{j}} \bar{D}_{\mathbf{j}}\left(\bar{I}\right) e^{i\bar{j}\cdot\bar{\varphi}} \tag{3.2}$$

Again, what we work to find through frequency analysis will be the complex series coefficients $\bar{D}_{\mathbf{j}}$ and their associated frequency combinations $\bar{j}\cdot\bar{\varphi}$. The φ_k can be described using the basis frequencies and time t through

$$\varphi_k = \Omega_k t + \varphi_{k_0} \tag{3.3}$$

where Ω_k is the kth fundamental frequency and φ_{k_0} is the initial kth angle value (φ_k at $t = 0$). In Eqn. 3.2, each $\bar{j}$ is a vector of integers, which, when the inner product $\bar{j}\cdot\bar{\varphi}$ is taken, allows for specification of integer combinations of the different basis frequency contributions. The details and mechanics of this will be discussed below.

3.1.2 Spectral Analysis. The problem of finding the basis frequencies for an orbit is best solved using a method similar to that of Laskar as given in [9] and [10], known as the Numerical Algorithm of the Fundamental Frequency (NAFF). Per Laskar, we may take the finite fourier transform of coordinate data $f(t)$ at a frequency ω by

$$\phi(\omega) = \frac{1}{2T} \int_{-T}^{T} f(t) e^{-i\omega t} \chi(t, T) dt \tag{3.4}$$

Laskar's method is obviously quite similar to normal Fourier analysis, but uses instead a *weight* or *window* function $\chi(t)$ to circumvent accuracy losses caused by the fact that the orbital data $f(t)$ is likely not truncated perfectly to contain an integer number of periods

over the time span $[-T, T]$. The aforementioned losses are due to a phenomenon known as *frequency leakage*- c.f. §3.1.2.2.

        3.1.2.1   The Power Spectral Density.   The goal of Laskar's method, when searching for a basis frequency, is to find the maximum of Eqn (3.4) in the neighborhood of a rough initial guess of the basis frequency in question. This, in essence, allows for the determination of the frequency value (accurate to within computational uncertainties) at which the spectral power is the highest. The spectral power, defined as $\mathcal{P} = |\phi|^2$, is the most common way to quantify contributions from different frequencies inherent in a signal. A plot of the power values for a range of frequencies, or spectrum, is aptly termed a *Power Spectral Density* (PSD) plot and is a useful way of rather intuitively examining the periodic characteristics of the signal. An example of a PSD plot for an orbit is shown in Figure (3.1) below. By simple observation, it is obvious for a non-chaotic orbit that there are a number of peaks in the PSD at various frequencies. These power peaks correspond, in the case of our perturbed orbit data "signal", to combinations of the three basis frequencies.
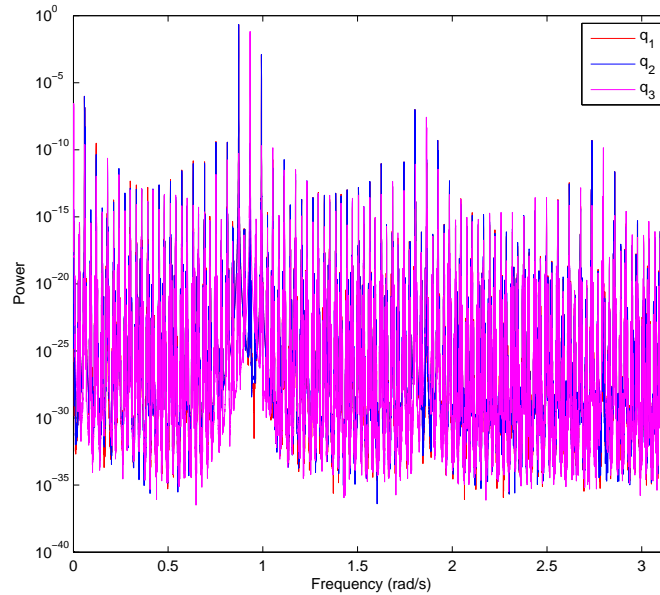
Figure 3.1.   Example of Power Spectral Density plot of an orbit for $\omega = [0, \pi]$ with window power $p = 2$.

3.1.2.2 Window Function and Window Power. The window function used in the current work for $\chi(t,T)$ in Eqn. (3.4) is known as the *Hanning window,* and is given by

$$\chi(t,T) = \frac{2^p \, (p!)^2}{(2p)!} \left[1 + cos\left(\frac{\pi t}{T}\right) \right]^p \tag{3.5}$$

where p is the *window power* and t and T are the current time step and the end time, respectively, as discussed above. Essentially, this window function serves to "smooth" the ends of the data set so that the values taper down to zero with varying speeds (related to the values of p). Such a tapering of the data eliminates the frequency leakage mentioned above by eliminating the discontinuity encountered if one "ties" the beginning and end of the data set together and treats it as one continuous periodic system. Laskar demonstrates efficient use of the Hanning window with powers of $3-5$ and states that powers above $p = 5$ tend to decrease accuracy [9]; Wiesel [24] and Little [11] use $p = 2$ almost exclusively. The author has found in the current work that a general statement about appropriate values for p cannot be made; that is, the choice of power depends upon the accuracy of the signal data, the length of the signal sampling period and the "stiffness" of the dynamics (related, in this case, to the order and degree of the geopotential expansion considered), among other factors. Wiesel shows an instructive example of the effects on the PSD of a spectral line by increasing window powers in [25]; essentially, as one increases the value of p, the values of the sidelobes around the spectral line fall off more and more quickly, with the potential sacrifice of frequency accuracy due to the broadening of the true frequency's peak in the PSD. See, for example, Figure (3.2) below. As in Wiesel, a value of $p = 2$ is a good general-purpose power; however, as mentioned by Laskar [9], it is advantageous to explore higher window powers until accuracy gains cease. In the current work, a power $p = 2$ proved sufficient for analysis of orbit integrations including $n, m \leq 5$; however, for 1-year integrations with $n, m = 20$, gains in accuracy of the fundamental frequencies continued in some cases up to $p = 7$, allowing the Ω_k to be determined to within an error of a few parts in 10^{12}.

3.1.2.3 Fourier Coefficients. As previously mentioned, the torus actions I_k are indirectly reflected in the complex Fourier coefficients $\bar{D}_j$ in Eqn. (3.2). It is sometimes
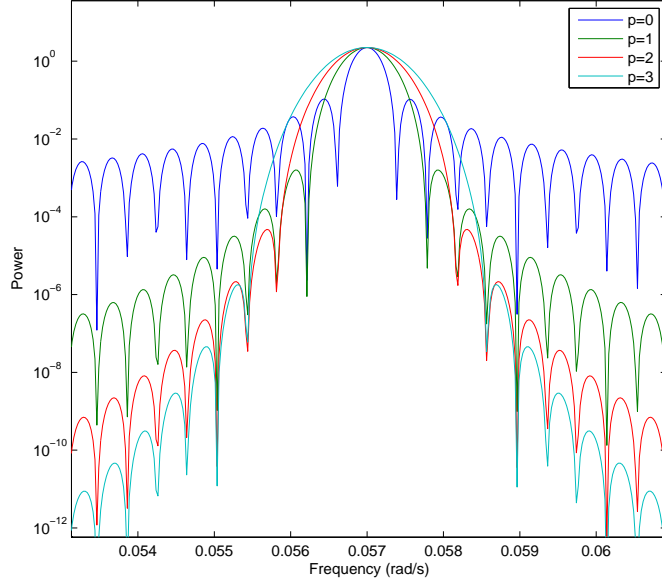
Figure 3.2.   Effects on the PSD for a spectral line of $\omega = 0.057\ rad$ from increasing Hanning window power p in Eqn.(3.5)- based on example from Wiesel, [25]

advantageous to rewrite the series (3.2) in real form as

$$\bar{q}\left(t\right) = \sum_{\bar{j}} \left[\bar{C}_{\bar{j}} cos\left(\bar{j} \cdot \bar{\varphi}\right) + \bar{S}_{\bar{j}} sin\left(\bar{j} \cdot \bar{\varphi}\right)\right] \tag{3.6}$$

so that we seek, from our spectral analysis, the coefficients $C_{\bar{j}_k}$ and $S_{\bar{j}_k}$, obtainable from Eqn. (3.4) by

$$C_k = 2\Re\phi\left(\omega_{\bar{j}}\right) \tag{3.7}$$

$$S_k = 2\Im\phi\left(\omega_{\bar{j}}\right) \tag{3.8}$$

where $\omega_{\bar{j}}$ is the frequency combination (or the PSD bin associated with the $\bar{j}$ in question), calculated with

$$\omega_{\bar{j}} = \bar{j} \cdot \bar{\Omega} \tag{3.9}$$

The constant term for each coordinate, C_{0_k}, may be found by evaluating Eqns. (3.7) and (3.8) with $\omega = 0$.

22

3.1.2.4 Spectral Decomposition. Finding the values of the Fourier coefficients mentioned in §3.1.2.3 has proven to be somewhat of an art. The author of the current work has found that simple Fourier analysis, i.e. obtaining the amplitudes of the spectral peaks per Eqns. (3.7) and (3.8), is only effective to a certain accuracy level due to two phenomena: spectral "shadowing" and frequency folding. Spectral shadowing occurs when one is dealing with a system where there is one very small frequency among the basis frequency set; i.e.

$$\exists \ (\Omega_m, \Omega_n) \in \bar{\Omega} \mid \Omega_m \ll \Omega_n, \ m \neq n \tag{3.10}$$

where the frequency proportion considered "small" depends upon the accuracy of the signal data and computational precision. The effect this has on the spectral analysis can be quite profound, because when one is analyzing the amplitudes of integer combinations of the elements of $\bar{\Omega}$, there will be circumstances in which one is interested in some frequency combination involving the largest frequency plus or minus the smallest frequency; for example, in a [not uncommon] case where we have an index and basis frequency set such that

$$\bar{j} = [1 \ 0 \ 1] \tag{3.11}$$

$$\bar{\Omega} = [0.98 \ 0.060 \ 0.0018] \, rad/s \tag{3.12}$$

we would then then be seeking the amplitude of a frequency

$$\omega_j = \bar{j} \cdot \bar{\Omega}$$

$$= 0.9818$$

In this case, the power of the basis frequency at $\Omega_1 = 0.98$ will almost certainly have a higher amplitude than ω_j, and since ω_j is so near to Ω_1, it will be very difficult to distinguish the true value of the amplitude at ω_j. This issue is even further exacerbated when using a window function, which, as mentioned above in §3.1.2.2 and shown in Fig. (3.2), has the effect of widening the peak, thus further obscuring the contributions of any frequencies in near proximity.

The second malicious effect, and an issue inherent in any practical signal analysis application, is frequency folding, which involves the "reflection" of spectral peaks about the *Nyquist frequency* or *Nyquist limit*,

$$\omega_{Nyquist} = \frac{\pi}{t_{sample}} \tag{3.13}$$

where t_{sample} is the sampling time interval of the [orbital] signal data. For example, consider the simple periodic function

$$X(t) = \sin(\nu_0 t) \tag{3.14}$$

where the frequency of oscillation $\nu_0 = 0.55 \ rad/TU$ and we obtain "propagation" data for times $t = [-T : \delta t : T]$, where we take $T = 8000 \ TU$ and $\delta t = 0.5 \ TU$. The PSD for this case after Fourier transform per Eqn. (3.4) is shown in Fig. (3.3) over the Fourier domain $\omega = [0, 4\pi]$; it is clear that the frequency domain representation of this function is merely a single spectral line at $\omega = \nu_0$. The reader is invited to notice, however, the aforementioned frequency folding manifested here: the signal in question has a Nyquist frequency of

$$\omega_{Nyquist} = \frac{\pi}{t_{sample}} = 2\pi \tag{3.15}$$

and it is easily seen that there are reflections evident in the PSD plot over the given domain. One "false" peak occurs at $\omega_{r_1} = \omega_{Nyquist} - \nu_0$, one at $\omega_{r_2} = \omega_{Nyquist} + \nu_0$ and one at $\omega_{r_3} = 2\omega_{Nyquist} - \nu_0$. The pattern of false peaks thus established continues on *ad infinitum* as one examines the powers of higher and higher frequencies. In general, however, we are only interested in those frequencies at or below $\omega_{Nyquist}$, as the Nyquist frequency represents the highest frequency that can be accurately sampled. We are left, then, with the issue of the reflection peak at $\omega_{r_1} = \omega_{Nyquist} - \nu_0$, since it poses a problem when we are trying to determine powers of the real frequency combinations inherent in the dynamical system.

Conveniently, it seems that the solution to both the spectral shadowing and frequency folding problems lies in a *spectral decomposition* method. Spectral decomposition

24
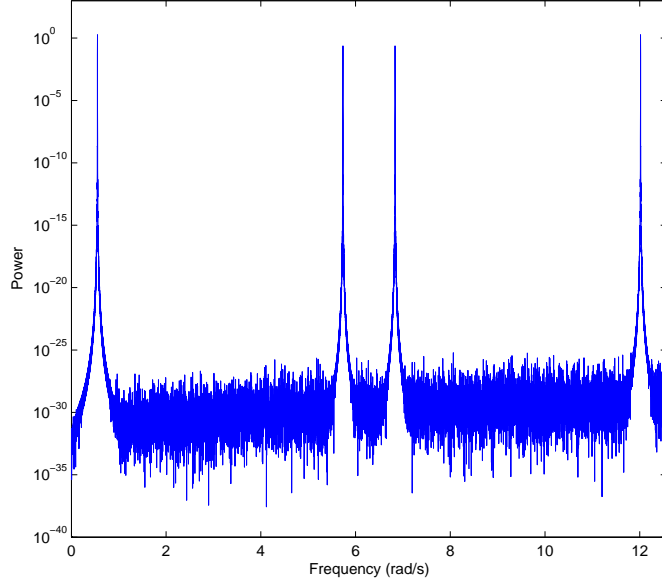
Figure 3.3. PSD of a spectral line at $\nu_0 = 0.55 \ rad/TU$ and sampling time $\delta t = 0.5 \ TU$ demonstrating frequency folding.

consists of proceeding through the spectral content of a signal, starting with the frequency combination having the largest power $\mathcal{P}(\omega)$, and removing the signal contribution of each spectral line before proceeding to the next highest. In essence, if one considers the frequencies and their associated powers composing the spectrum of a signal, organized into a set,

$$\mathbb{W} = [\omega_1, \omega_2, \ldots, \omega_m] \mid \mathcal{P}(\omega_{n+1}) < \mathcal{P}(\omega_n) \tag{3.16}$$

where m is the total number of frequencies to be analyzed in the spectrum, the spectral decomposition process proceeds iteratively through $\mathbb{W}$ to find the complex amplitudes ϕ_n using the equation

$$\phi_n = \phi(\omega_n) = \frac{1}{2T} \int_{-T}^{T} f_n(t) e^{-i\omega_n t} \chi(t, T) dt \tag{3.17}$$

where $f_n(t)$ represents the "decomposed" orbital signal data, having removed from the original data f_0 the contributions of all frequencies $\omega < \omega_n$ in $\mathbb{W}$; that is,

$$f_n(t) = f_0(t) - \sum_{h=1}^{n-1} D_h e^{i\omega t} \tag{3.18}$$

25

In the case of spectral shadowing, the use of this decomposition method allows the analyst to distinguish the separate contributions from two proximate frequencies with a much higher accuracy than is possible with mere Fourier analysis. In the case of frequency folding, spectral decomposition may be applied with one important caveat: in all cases observed so far by this author, the "true" peak will have a higher power in the PSD than any of its dependent reflections under $\omega_{Nyquist}$; that is,

$$\mathcal{P}(\omega_{r_n}) < \mathcal{P}(\nu_0) \; \forall \omega_{r_n} < \omega_{Nyquist} \tag{3.19}$$

This is evident in Fig. (3.3) when comparing the peak at ν_0 to the peak at $\omega_{r_1} = \omega_{Nyquist} - \nu_0$. This relationship betwen the powers of a frequency and its reflections allows the analyst to use the iterative process given in Eqns. (3.17) and (3.18), since the conditions on $\mathbb{W}$ as given in Eqn. (3.16) are met. In essence, after one removes the contribution of the *true* peak at $\omega = \nu_0$, the reflection peaks disappear from the remaining signal and cause no further confusion in determination of peaks and their frequencies.

3.1.2.5 Fourier Indices. The spectral analysis process outlined in the above sections requires, upon mechanization in a numerical routine, a somewhat unusual consideration regarding the integer indices $\bar{j} = j_1 + j_2 + j_3$. Following Wiesel [25], the current work utilizes an index coding strategy in which the first non-zero term in $\bar{j}$ is never negative; this precaution serves to eliminate repetition due to the nature of negative arguments in trigonometric functions- namely, $sin(-x) = -sin(x)$ and $cos(-x) = cos(x)$.

3.1.3 Nature of the Basis Frequencies. The fundamental frequencies manifest as combinations of the frequencies of commonly observed effects in Earth orbit [24]. The first and largest fundamental frequency is known as the *anomalistic frequency* and is given approximately by

$$\omega_1 \approx \sqrt{\frac{\mu}{a^3}} \left\{ 1 - \frac{3J_2 R_\oplus^2}{2a^2(1 - e^2)^{3/2}} \left(\frac{3}{2}sin^2 i - 1 \right) \right\} \tag{3.20}$$

where a is the semi-major axis, e is the orbital eccentricity, i is the orbital inclination and J_2, $R_\oplus$ and μ are as given previously in Chapter II, and where only effects of the first

26

zonal harmonic are included (hence its approximate nature). It is clear that this is the largest frequency due to its containing the Keplerian (or two-body) frequency (also the mean motion in our circular case),

$$\omega_{TB} = \sqrt{\frac{\mu}{a^3}} \tag{3.21}$$

as its first term. The second fundamental frequency is the combination of the earth's rotational frequency with the orbit's nodal regression rate:

$$\omega_2 \approx \omega_\oplus + \frac{3\sqrt{\mu}J_2 R_\oplus^2}{2a^{7/2}(1-e^2)^2}cos(i) \tag{3.22}$$

The nodal regression rate in this equation refers to the tendency of the orbital plane to rotate about the primary's *Earth-centered inertial* (ECI) frame's 3-axis due to the oblateness of the primary, most easily seen as a secular change in the angle between the inertial 1-axis and the line of nodes. The third, final and smallest fundamental frequency is found to be the *apsidal regression rate*:

$$\omega_3 \approx -\frac{3\sqrt{\mu}J_2 R_\oplus^2}{2a^{7/2}(1-e^2)^2}\left(sin^2 i - 2\right) \tag{3.23}$$

which accounts for the tendency of the orbit to rotate within its own plane about the orbit normal; this manifests as a secular change in the argument of perigee used in the classical orbital elements.

Depicted in Figures (3.4)-(3.6) below are the relationships between the fundamental frequencies (as approximated by Eqns. (3.20)-(3.23)) and the inclination i and altitude for nearly circular orbits ($e \approx 0.00108$). The first basis frequency Ω_1, shown in Fig. (3.4), shows the expected behavior in that the anomalistic frequency should decrease in value as the orbit increases in altitude, which is a direct corollary of Eqn. (3.21) above. Additionally, for a given altitude, the first basis frequency decreases slightly as the inclination of the orbit increases. This follows from Eqn. (3.20), as the total contribution from the second term depends on $sin(i)$, and the magnitude is thus fully subtracted when $i = 90°$.
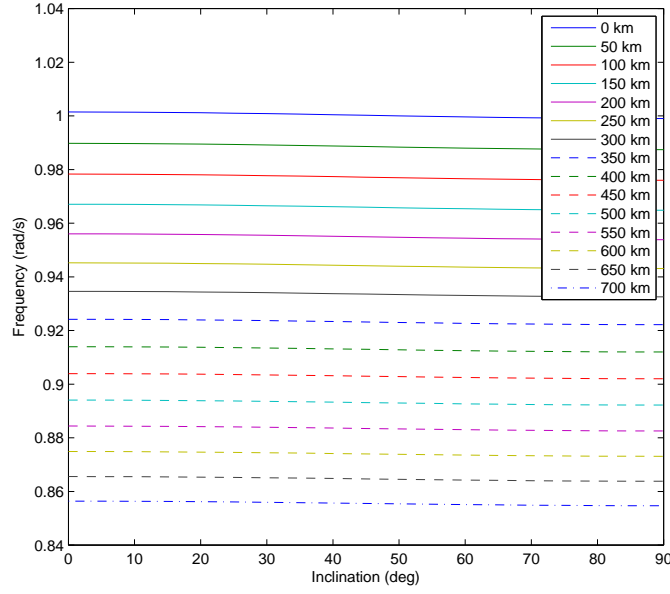
Figure 3.4.   Behavior of Ω_1 for a near-circular orbit with varying altitudes and inclinations.

Figure (3.5) shows that Ω_2 decreases in value for increasing altitude; again, this follows logically from the fact that the difference between the true geopotential and the two-body potential decreases as radius increases. The figure also demonstrates the well-known behavior of the orbits' nodal regression rates; these rates decrease nonlinearly as the orbit inclinations increase, so that the nodal regression is a maximum at $i = 0°$ and is zero at $i = 90°$, in agreement with Eqn. (3.22). It is important to note that the frequency shown along the vertical axis of Fig. (3.5) is, as stated above, the combination of the earth's rotation rate $\omega_\oplus = 0.0588336 rad/TU$ with the nodal regression; this explains why the fundamental frequency tends towards $\omega_\oplus$ as $i \to 90°$. Also of note is that the nodal behavior for retrograde orbits (orbits with $i > 90°$) is not shown in Fig. (3.5). For retrograde orbits, the nodal regression rate becomes negative, which means that the orbit precesses westward rather than eastward as in prograde orbits.

The third basis frequency, Ω_3, depicted in Fig. (3.6), shows another commonly characterized and utilized orbital trend. This apsidal regression rate has a so-called *critical inclination* at $i^* \approx 63.4°$; that is, the argument of perigee essentially does not grow secularly

28
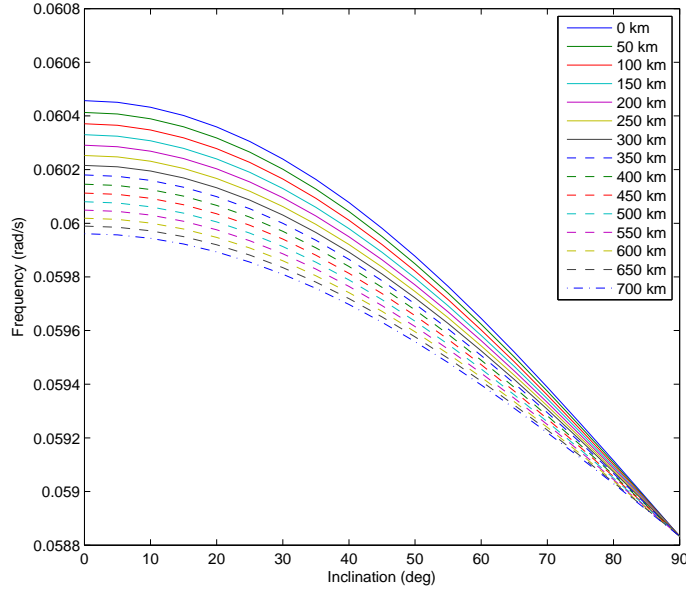
Figure 3.5.   Behavior of Ω_2 for a near-circular orbit with varying altitudes and inclinations.

for an orbit at this inclination. A common historical usage of the critical inclination has been the *Molniya orbit* used by the former USSR and now Russia in order to allow maximum coverage of the northern hemisphere by a satellite with a highly elliptic orbit (c.f. [19] for more details). Figure (3.6) also shows the relationship of the apsidal regression rate of circular orbits to varying altitude and inclination when $i \neq i^*$. When $i < i^*$, increasing altitude decreases the regression frequency, whereas the opposite is true for $i > i^*$.

The fundamental frequencies described in the equations and plots of this section represent, again, merely approximations of the true frequencies of the system, as they include only the J_2 term of the geopotential expansion. In order to find the true values of the basis frequencies, frequency analysis must be utilized on the propagated orbital data including the other geopotential terms using the methodology outlined earlier in this chapter.
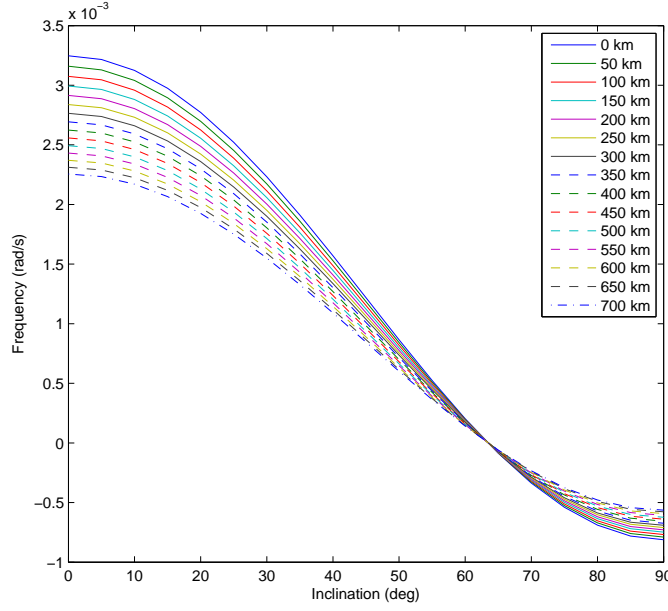
Figure 3.6.   Behavior of Ω_3 for a near-circular orbit with varying altitudes and inclinations.

3.2   Orbital Propagation

The principles of §3.1 make it clear that the beginning of KAM torus construction lies in the acquisition of orbital data in some fashion. Judging from the literature, there has been considerable success in this area. As mentioned in Chapter II, Little has demonstrated fitting of KAM tori to observed orbital data for Earth satellites with reasonable accuracy [11]. Additionally, Wiesel has demonstrated incontrovertible evidence that a general Earth satellite lies on a KAM torus through the least-squares fitting of numerically integrated data [24] and also shown the fitting of numerical data for the restricted three-body problem, a system with 2 degrees of freedom, using an improved method of Fourier Analysis [25]. The current work builds upon the methodology used by Wiesel and Little and extends it to formation design.

3.2.1   Equations of Motion.   Orbital data for the orbit examined in the current work are obtained through numerical integration of the equations of motion derived from the Hamiltonian derived in Chapter II with orbit geometry determined by judicious choice of initial conditions. The equations of motion may easily be derived from the Hamiltonian

by:

$$\dot{q}_k = \frac{\partial H}{\partial p_k}$$
$$\dot{p}_k = -\frac{\partial H}{\partial q_k} \tag{3.24}$$

The derivative of the state vector at any position then becomes, after substitution and differentiation,

$$\dot{\bar{\xi}}(q,p) = [\dot{q} \;\; \dot{p}]^T \;\; = \begin{bmatrix} p_1 + \omega_\oplus q_2 \\ p_2 - \omega_\oplus q_1 \\ p_3 \\ \omega_\oplus p_2 - \frac{\partial U(\bar{q})}{\partial q_1} \\ \omega_\oplus p_1 - \frac{\partial U(\bar{q})}{\partial q_2} \\ -\frac{\partial U(\bar{q})}{\partial q_3} \end{bmatrix} \tag{3.25}$$

where $U(\bar{q})$ represents the potential function at position $\bar{q}$ (as described in Ch. II), which implies that its derivative represents the geopotential force upon the satellite.

3.2.2 Numerical Integrator. The numerical integration for this work was performed using an explicit 8th order Runge-Kutta integrator, based upon that given by Dorman and Prince in [16], which performs 13 evaluations per time step and has a local error of order h^9. This integrator, like the Hamming integrator used by Wiesel in [24] and by Little in [11], is not symplectic; that is, it does not explicitly conserve the Hamiltonian (this system's constant of the motion). This fact allows for us to 'check' the accuracy of the integrator by calculating at every output time step the error value

$$\Delta H = H(t) - H(t_0) \tag{3.26}$$

and ensuring that this difference has remained suitably small. Figure (3.7) below shows the error growth for an archetypal numerical integration of an orbit at 320 km altitude, inclined at 30 degrees, over a total time period of approximately 1 year and including all geopotential terms up to order and degree $m, n = 20$. As seen in the figure, the error

31

for this typical case shows pseudorandom behavior with maximum amplitude near the accuracy bounds of machine double precision at approximately 4×10^{-13}, establishing a high confidence in the accuracy of the integration results. Figure (3.8) shows the same Hamiltonian error array after the application of the Hanning window (Eqn. (3.5)) with $p = 6$. This represents the apparent error seen by the spectral analysis algorithm. Comparison of the two figures reveals two important realizations: first, the maximum error is decreased from approximately 4×10^{-13} to approximately 2.4×10^{-13}; second, the tradeoff comes in that the local error closer to the center of the windowed data set is slightly higher than the associated error in the unwindowed data.
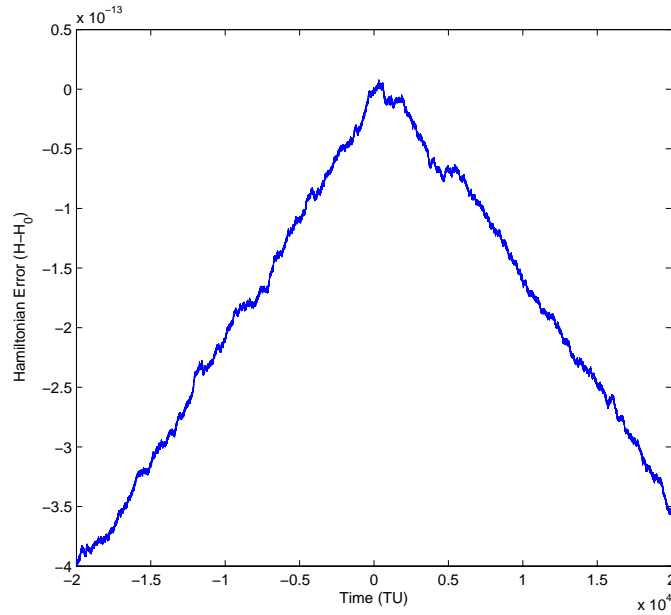
Figure 3.7.   Example of Hamiltonian error over integration time of approx. 1 year for an Earth orbit with $m, n = 20$, 320km altitude, 30 deg inclination.

3.2.3 Integration Characteristics.   The method of spectral analysis (and thereby KAM torus construction) outlined above requires integrated data with certain characteristics to function properly and with the desired accuracy. First, the integration time must be symmetrically split around $t = 0$; that is, the final set of data consists of a backwards integration over the timescale $-T \leq t \leq 0$ combined with a forward integration over $0 < t \leq T$, consistent with Eqn. (3.4). This formulation, as described in [9] and [25] allows the user to

32
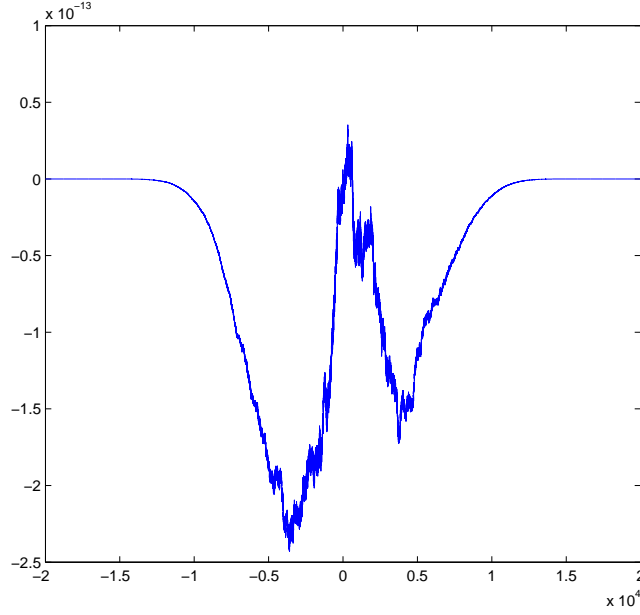
Figure 3.8.   Hamiltonian error as in Fig. (3.7) after application of a window function with $p = 6$, per Eqn. (3.5).

take advantage of the finite accuracy available from any real-world numerical integration, as the total error growth over the interval $[0, T]$ is (in these and similar systems) smaller than the error growth over the interval $[0, 2T]$. Second, and unfortunately, the method of KAM torus construction as it currently stands requires integration of long periods of orbital data (large T) with very fine temporal resolution in the outputs (small δt).

3.3   Formation Analysis on the Torus

Using KAM theorem to design a satellite formation or constellation requires, of course, that the designer obtain the KAM torus for a particular orbit by applying the methodology previously outlined in this chapter (§3.1) to orbital data, either observed or integrated (per §3.2). After the torus series given in Eqns. (3.2) and (3.6) is known in terms of the series coefficients $C_{\bar{j}_k}$ and $S_{\bar{j}_k}$ and the basis frequencies Ω_k, the astrodynamicist can displace the initial condition of a satellite while constraining it to the same torus by using the equation:

$$\varphi_k^* = \varphi_k + \delta\varphi_k \tag{3.27}$$

33

where φ_k is the kth angle variable as defined in Eqn. (3.3). In effect, Eqn. (3.27) serves to replace each φ_k with a new φ_k^*, perturbed by some KAM displacement angle $\delta\varphi_k$. The displacement manifests in the KAM series as

$$
\begin{aligned}
\bar{q}(t) &= \bar{C}_0 + \sum_{\bar{j}} \left[\bar{C}_{\bar{j}} cos \left(\bar{j} \cdot \{\bar{\varphi} + \delta\bar{\varphi}\} \right) + \bar{S}_{\bar{j}} sin \left(\bar{j} \cdot \{\bar{\varphi} + \delta\bar{\varphi}\} \right) \right] \\
&= \bar{C}_0 + \sum_{\bar{j}} \left[\bar{C}_{\bar{j}} cos \left(\bar{j} \cdot \bar{\varphi} + \bar{j} \cdot \delta\bar{\varphi} \right) + \bar{S}_{\bar{j}} sin \left(\bar{j} \cdot \bar{\varphi} + \bar{j} \cdot \delta\bar{\varphi} \right) \right]
\end{aligned}
\tag{3.28}
$$

Eqn. (3.28) describes in general terms a new state at time t with the aforementioned displacement. What we usually seek in formation design, however, is initial conditions for two satellites in physical coordinates, $(\bar{q}, \bar{p})$, which will allow for the desired relative motion. We may use Eqn. (3.6) to find the initial coordinates for some *Satellite 1* at an initial time $t_0 = 0$ simply by:

$$
\bar{q}_{S1}(t_0) = \bar{C}_0 + \sum_{\bar{j}} \bar{C}_{\bar{j}}
\tag{3.29}
$$

Given some initial desired KAM angular separation vector $\delta\bar{\varphi}$ between the satellites, the initial coordinates for *Satellite 2* may be found from Eqn. (3.28) as

$$
\bar{q}_{S2}(t_0) = \bar{C}_0 + \sum_{\bar{j}} \left[\bar{C}_{\bar{j}} cos \left(\bar{j} \cdot \delta\bar{\varphi} \right) + \bar{S}_{\bar{j}} sin \left(\bar{j} \cdot \delta\bar{\varphi} \right) \right]
\tag{3.30}
$$

In order to find the initial values of the momenta for satellites 1 and 2 from the series, we realize that, for a satellite S_n in the ECEF frame [25],

$$
\bar{p}_{S_n}(t) = \mathcal{R}_2 \, \dot{\bar{q}}_{S_n}(t) + \mathcal{R}_1 \, \bar{q}_{S_n}(t)
\tag{3.31}
$$

where $\mathcal{R}_2$ is the identity matrix $\mathbb{I}_{3\times3}$ and

$$
\mathcal{R}_1 = \begin{bmatrix} 0 & -\omega_\oplus & 0 \\ \omega_\oplus & 0 & 0 \\ 0 & 0 & 0 \end{bmatrix}
\tag{3.32}
$$

34

The values of $\dot{\bar{q}}_{S_n}(t)$ in Eqn. (3.31) may be found from the series (3.6) by simply differentiating with respect to time, so that

$$\dot{\bar{q}}(t) = \sum_{\bar{j}} \left[-(\bar{j} \cdot \bar{\Omega}) \bar{C}_{\bar{j}} sin\left(\bar{j} \cdot \bar{\Omega} t\right) + (\bar{j} \cdot \bar{\Omega}) \bar{S}_{\bar{j}} cos\left(\bar{j} \cdot \bar{\Omega} t\right) \right] \tag{3.33}$$

For a description of the implementation of the above process, continue to the next chapter.

IV. Results and Findings

This chapter will present some of the results of the current work. It will begin with the outcomes of the KAM torus fitting process for various orbits, including an analysis of accuracy gains as a function of the number of KAM series terms included. Next, the nature of satellite separations in the torus angles φ_k will be discussed, followed by the results of the actual satellite formation analyses. Finally, a brief sketch on the effects on KAM tori of non-conservative forces will be given.

4.1 KAM Torus Fitting

This section shows results from the process of fitting KAM tori to integrated data of four satellite orbits which are combinations of two altitudes (320 km and 630 km) and two inclinations ($i = 15°, 30°,$) . The orbits were chosen as representative orbits of common Earth satellites and serve to demonstrate the method in question. The method may, of course, be generalized (within certain bounds) to obtain KAM tori for a much greater range of orbit altitudes and inclinations. The intricacies of the KAM tori for the examined orbits show definite patterns, thus allowing the analyst to make useful statements about the general case. It is, however, beyond the scope of this work to complete a full survey of KAM tori for all possible inclination/altitude combinations, as the fitting and decomposition process can be quite time-consuming and computationally intensive.

4.1.1 Torus series terms and accuracy gains.   When fitting KAM tori to orbital data, the issue of how far to extend the approximation naturally arises. While, in general, including more terms in the series given by Eqn. (3.6) tends to increase the accuracy of results, a point is reached similar to that encountered in other approximation analyses where the dynamicist encounters the law of diminishing returns – that is, there is a certain number of terms for each orbit after which gains in accuracy come extremely slowly, if at all. In an effort to numerically characterize the relationship between the number of Fourier series terms and the accuracy of an orbit reconstructed from the series, the following procedure was utilized. First, the orbit for a satellite at a specific altitude/inclination combination was numerically integrated to obtain approximately 12 months of orbital data

with a windowed integration error similar in order to that shown in Figure (3.8). Then, the basis frequencies are determined to a very high accuracy using an appropriate window function, as in Chapter III. Next, a first-pass KAM torus approximation was calculated by using Laskar's and Wiesel's methods of Fourier analysis, using a certain index limit vector. This approximation gives us a good starting-point for the future spectral decomposition, as it identifies the locations of the highest peaks. Also, one may use this torus approximation as a check to determine whether or not the index limits are sufficient to capture the spectral behavior of the dynamics: finding the power spectral density plot of the orbit "calculated" from the approximate series and then comparing that PSD to the PSD calculated from the "true", integrated orbital data supplies the analyst with critical knowledge of missing peaks. For an example of this, see Fig. (4.1) below; in this figure, the red curve represents the partial PSD of the integrated ("true") data and the blue curve represents the partial PSD of the orbit constructed using the fitted torus series with index limits $\bar{j}_{lim} = [5, 5, 1]$. The black diamonds in the figure show the locations of the frequency combinations included in the analysis – i.e., combinations of the basis frequencies up to the limits in $\bar{j}_{lim}$. In this case, the basis frequency set was determined to be $\Omega \approx [0.93243, 0.060025, 0.0018922]$. The figure clearly shows that the largest peaks in this partial frequency window occur at the combinations of Ω_k (e.g. the peak at $\omega \approx 0.874$ is the combination $\omega = \Omega_1 - \Omega_2$, etc.). It is also clear that, due to the limitations of the series indices included, there are peaks that are "missed" in the analysis. Please note that this $\bar{j}_{lim}$ is merely an example case and does not represent a typical index limit to obtain a highly accurate KAM torus. For informational purposes, the coordinate residuals for the approximate torus determined with these index limits as compared to the integrated data are given in Fig. (4.2) below.

After finding the approximate torus series, we may input said calculated series along with the original orbital data into the spectral decomposition routine, where the signal is decomposed into its true frequency contributions up to some maximum series term limit. The resulting "refined" series provides a much higher accuracy than the approximate Fourier analysis can, and we may use the series to investigate the title question of this subsection: how the accuracy depends on the number of series terms. We proceed to reconstruct orbital data from the KAM series by calculating the coordinates and momenta
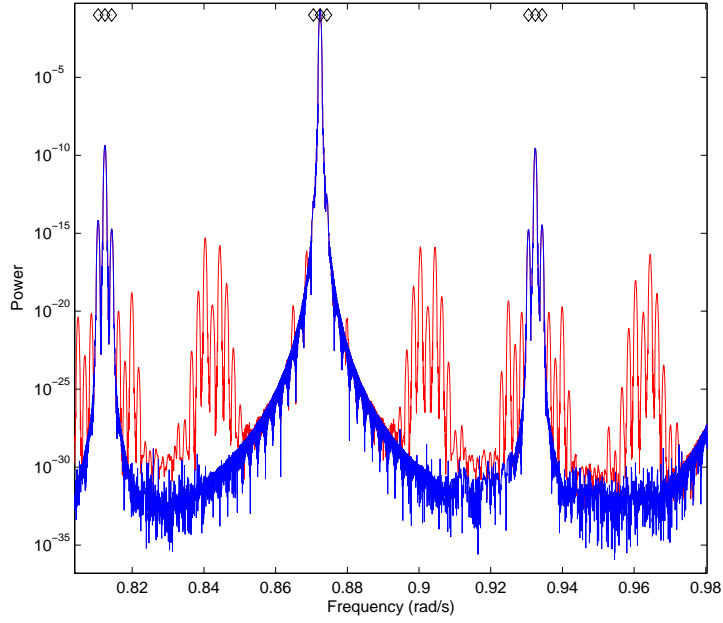
Figure 4.1. Partial PSDs of 320 km, $i = 30°$ orbit (red) and approximate series with $\bar{\bar{j}}_{lim} = [5, 5, 1]$ (blue)
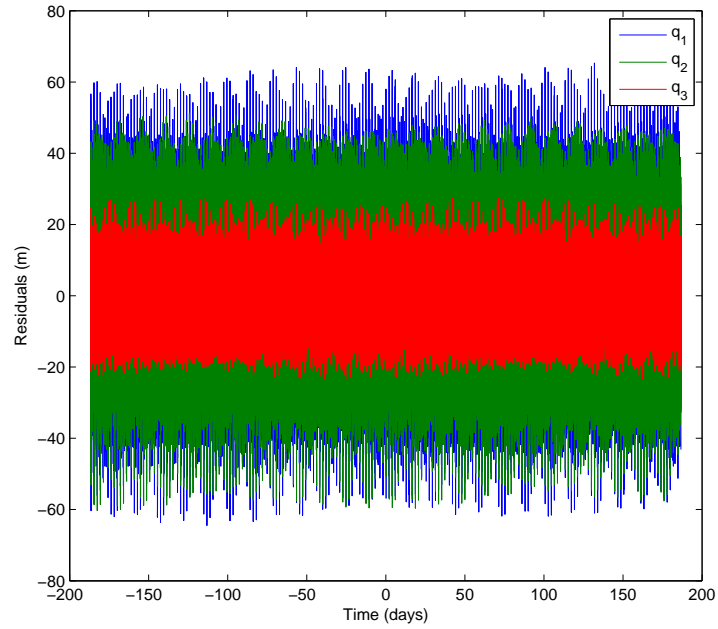
Figure 4.2. Residuals of fitting 320 km, $i = 30°$ orbit with approximate series found by $\bar{\bar{j}}_{lim} = [5, 5, 1]$

at every time t using Eqns. (3.6), (3.31) and (3.33) and the Ω_k, $\bar{C}_{\bar{j}}$ and $\bar{S}_{\bar{j}}$ from the refined series. These calculations may be conveniently performed to include any number of the terms analyzed in the spectral decomposition; the results of the 12-month RMS residuals for each coordinate are shown versus the number of included series terms in Fig. (4.3) below. The orbit is the same 320km, 30° orbit discussed above, but the KAM fitting was
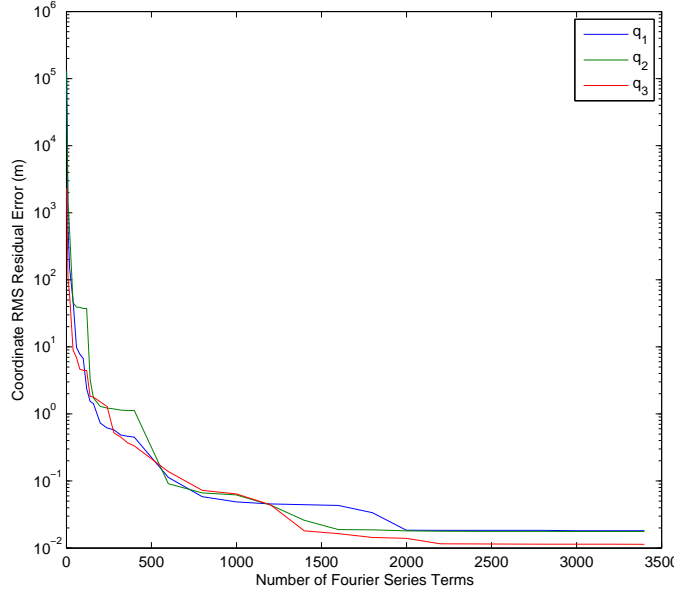
Figure 4.3.   Coordinate RMS residuals over 1 year vs. number of series terms for 320km, 30° orbit

performed with $\bar{j}_{lim} = [20, 25, 2]$ to obtain frequency combinations up to the Nyquist limit. To be clear regarding convention, the "number of series terms" in the figures below refers not to the $\bar{j}_{lim}$, but rather is related to the number of terms included from the ordered set $\mathbb{W}$ of frequency combinations discussed in §3.1.2.4. The "number of series terms" in the plots specifically refers to the number of C and S coefficients used and is calculated from the number of frequency combinations as

$$N_{terms} = 2N_{\omega} \tag{4.1}$$

since there are two trigonometric coefficients for each frequency combination (i.e. a real and imaginary part of each complex amplitude). The RMS residuals for each coordinate

39

are determined in the usual fashion as

$$r_{RMS_k} = \sqrt{\frac{1}{M} \sum_{m=1}^{M} q_k(t_m)} \tag{4.2}$$

Similarly, the RMS errors in the momenta for the aforementioned 320km, 30 degree orbit can be seen in Figure (4.4). It is easily seen from Figs. (4.3) and (4.4) that, for the
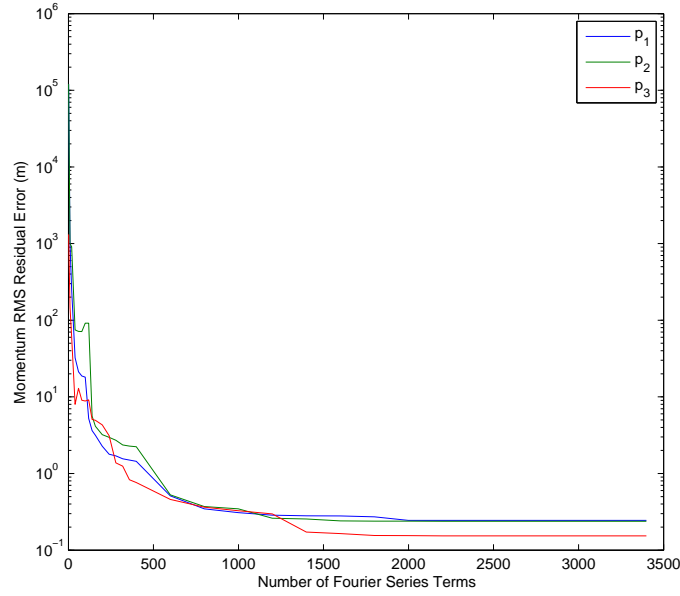
Figure 4.4. Momentum RMS residuals over 1 year vs. number of series terms for 320km, 30° orbit

orbit examined, there is little relative accuracy gain after approximately 1500 terms in the momenta and after approximately 2000 terms in the coordinates. It is instructive to note that, as mentioned previously, 1500 terms correspond to roughly $N/2$ or 750 frequency combinations; similarly, 2000 terms correspond to 1000 frequency combinations.

Extension of this methodology to an orbit of 630 km and $i = 30°$ gives the expected result: a higher altitude orbit is affected less by the geopotential perturbations, and may thus be represented to the maximum possible accuracy by fewer terms than the equivalent low-altitude case. Figures (4.5) and (4.6) below show the RMS residuals for the coordinates and momenta, respectively, for the 630 km orbit over a period of 1 year. As seen in the

figures, the accuracy reaches its steady state after approximately 1200 terms (600 sets of C and S coefficients) in both the coordinates and momenta.
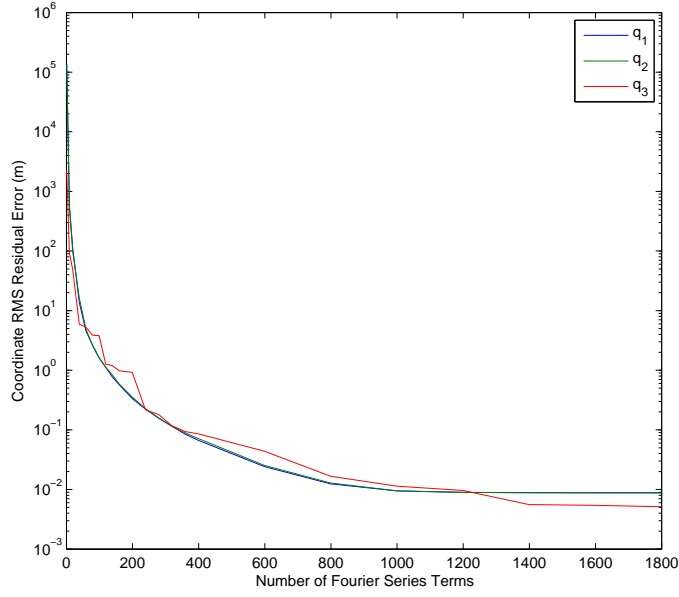
Figure 4.5.   Coordinate RMS residuals over 1 year vs. number of series terms for 630km, 30° orbit

It is important to note that, in the torus construction process utilized in this work, the accuracy of the calculated momenta is always lower than that of their associated coordinates. This is due to the fact that the error in the momenta is a compound error composed of the errors of the coordinates q_k and the coordinate's derivatives $\dot{q}_k$, as is obvious from cursory examination of Equations (3.31) and (3.33).
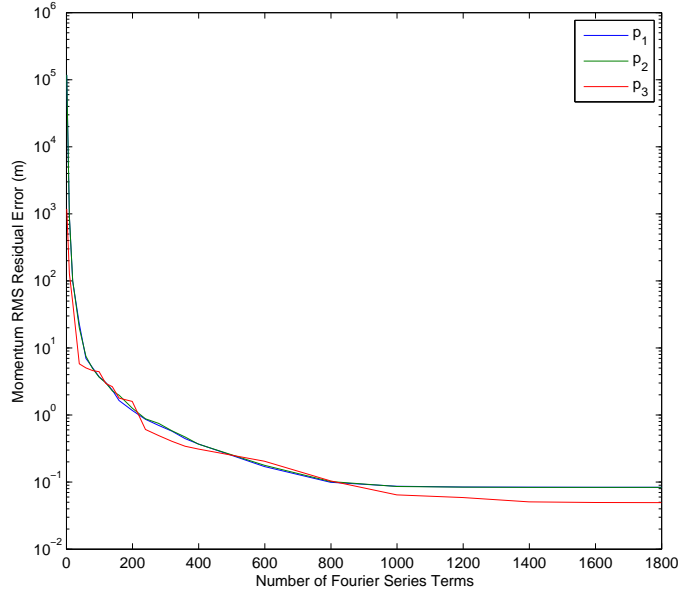
Figure 4.6.   Momentum RMS residuals over 1 year vs. number of series terms for 630km, 30° orbit

4.1.2 Orbit 1: Nearly circular, 320km Altitude and $i = 30°$.   The first orbit, involving an altitude of 320km and an inclination of 30°, is mentioned extensively in the previous subsection and is used in this work as a sort of base orbit. As stated above, the satellite's motion for orbit 1 was integrated per the methodology in Chapter III over a period of time $[-T, T]$ where $T \approx 6$ *months*, yielding a total integration period of approximately twelve months, or one year. Following the integration, a first-pass torus was constructed and then the data were spectrally decomposed using the method outlined in Chapter III and §4.1.1 above. The residuals were then found by subtracting the "calculated" steps using the KAM series at each time step from the "true" states of the integrated orbit. Figures (4.7) and (4.8) below show the coordinate and momentum residuals for the 320km, $i = 30°$ orbit before and after decomposition; i.e. with only the first-pass torus approximation (Fig. (4.7)) and with the more accurate decomposed torus (Fig. (4.8)). The torus used to obtain the residuals in the figures uses maximum index limits $\bar{j}_{lim} = [20, 25, 2]$. We note that the q_2 residuals in Fig (4.7) are not visible because they are practically equivalent to and, therefore, occluded by the q_1 curve.

42
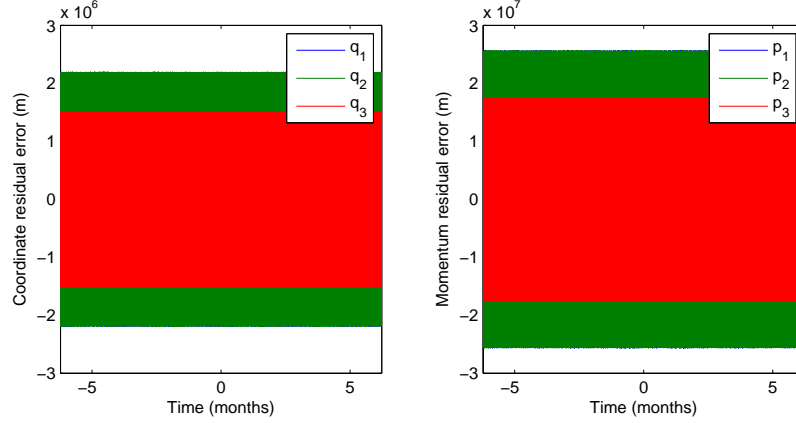
Figure 4.7.   Coordinate and momentum residuals over 1 year before spectral decomposition for nearly circular, 320km, 30° orbit
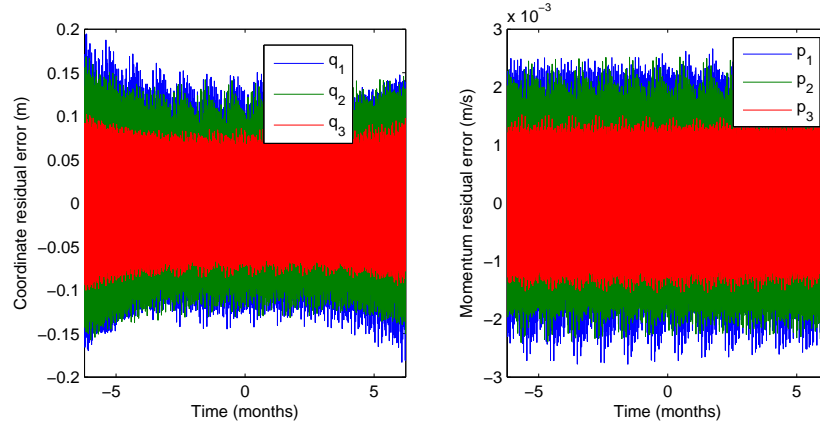
Figure 4.8.   Coordinate and momentum residuals over 1 year after spectral decomposition for nearly circular, 320km, 30° orbit

4.1.3   Orbit 2: Nearly circular, 320km Altitude and $i = 15°$.   An orbit at the same 320km altitude but at $i = 15°$ was analyzed to obtain the coordinate and momentum residuals in the below Fig. (4.9). With the lower inclination, the orbit proved to be much more easily analyzed. The coordinate residuals without any decomposition were practically identical to those shown in the figure; however, the decomposition improved the momentum residuals by several orders of magnitude. The series was decomposed to only 1400 terms in this case. There is an evident demonstrated trend towards generally easier calculation of tori with lower inclinations – see §5.1.1 *Limitations and considerations in the KAM fitting process* in Chapter V.

43
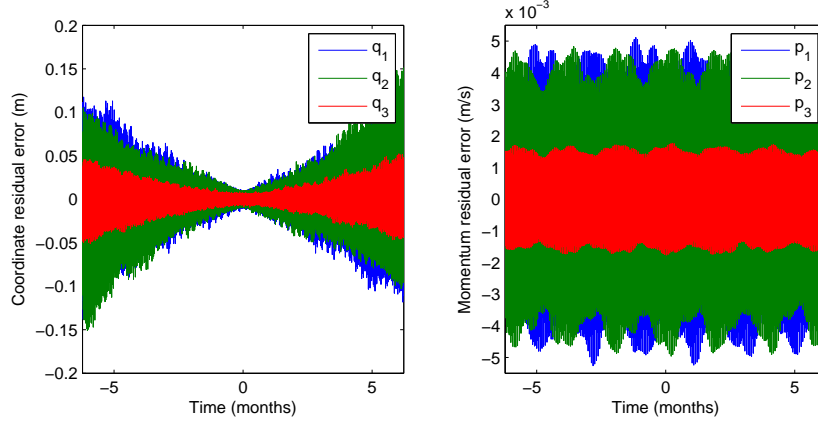
Figure 4.9.   Coordinate and momentum residuals over 1 year after spectral decomposition for nearly circular, 320km, 15° orbit

4.1.4   Orbit 3: Nearly circular, 630km Altitude and $i = 30°$.   The third orbit used throughout the rest of this work is an orbit at an altitude of 630km and $i = 30°$, and its residuals are displayed in Fig. (4.10). The residuals are generally about 1/3 the magnitude of those of the 320km orbit at the same inclination. It is the opinion of the author that this is a result of the orbit's higher altitude, which allows it to experience less of the perturbation from the geopotential.
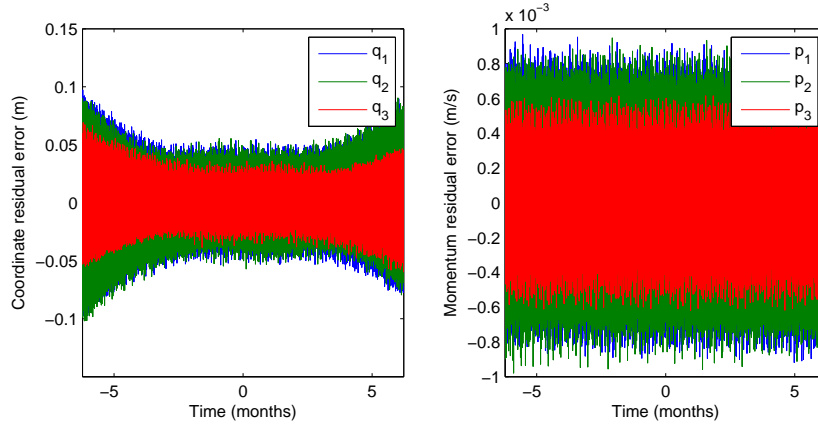
Figure 4.10.   Coordinate and momentum residuals over 1 year after spectral decomposition for nearly circular, 630km, 30° orbit

4.1.5   Orbit 4: Nearly circular, 630km Altitude and $i = 15°$.   The final orbit, at 630km and $i = 15°$, shows an unexpected result in that the residuals (shown in Fig. (4.11))

are along the same order as those of the higher inclination orbit at the same altitude. It is believed that the potential perturbations are just subtle enough at 630km that the KAM torus construction process is limited by the computational accuracy of the integration, which would account for the similar magnitudes between the orbits at the two different inclinations.
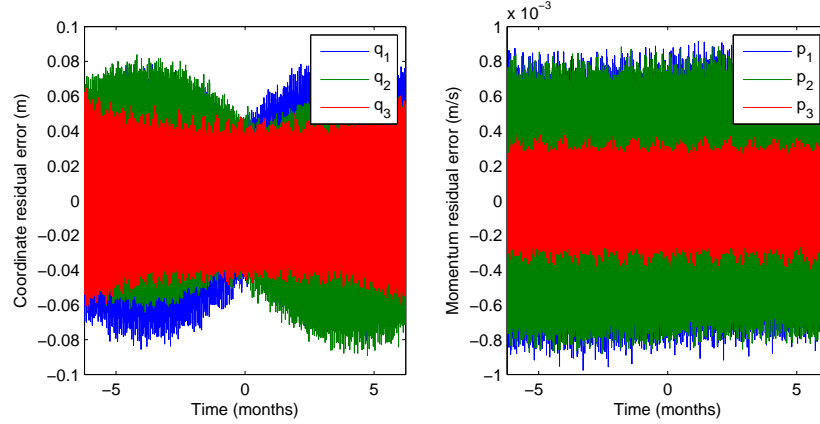
Figure 4.11.   Coordinate and momentum residuals over 1 year after spectral decomposition for nearly circular, 630km, 15° orbit

4.1.6   Torus actions and their constancy.   Since we have, by following the methodology outlined in this paper, ostensibly constructed tori in the Action-angle space (I, φ), a logical check is to calculate and examine the torus actions I. As mentioned in Chapter III, the torus actions should be constant for a system with only conservative perturbations. When one has in hand the torus parameters, the actions may be found using the Hamilton-Jacobi theorem (see e.g. [25], [14]) by the contour integral

$$I_i = \frac{1}{2\pi} \oint_{\Gamma_i} \bar{p} \cdot d\bar{q} \tag{4.3}$$

45

where $\bar{p}$ is the vector of the momenta as found by Eqn. (3.31) and the differential $d\bar{q}$ for contour Γ_i is found by

$$d\bar{q} = \frac{\delta\bar{q}}{\delta\varphi_i}d\varphi_i$$
$$= \sum_{\bar{j}}\left[-(\bar{j})\bar{C}_{\bar{j}}sin\left(\bar{j}\cdot\bar{\varphi}t\right) + (\bar{j})\bar{S}_{\bar{j}}cos\left(\bar{j}\cdot\bar{\varphi}t\right)\right] \tag{4.4}$$

To check the constancy of the actions, the above integral was taken over the full 2π range of φ_1 and φ_2 for the 320km, 30° orbit; specifically, the action was calculated using Eq. (4.4) around each irreducible contour Γ_i at 20 equally spaced locations around the torus (in intervals of $\pi/10$ from $\varphi_1, \varphi_2 = [0, 2\pi]$). Figure (4.12) below shows the result of the action calculations at these locations. The plot clearly shows that the torus actions are constant to within computational uncertainty. The graphical representation also shows the proportions of the actionsf: the two actions corresponding to the angles φ_1, φ_2 are four to five orders of magnitude greater than the action corresponding to φ_3. Indeed, these are the same action proportions used to construct the 3-toroidal "projection" into 2-toroidal space, given in Figure (2.7) in §2.3.1.
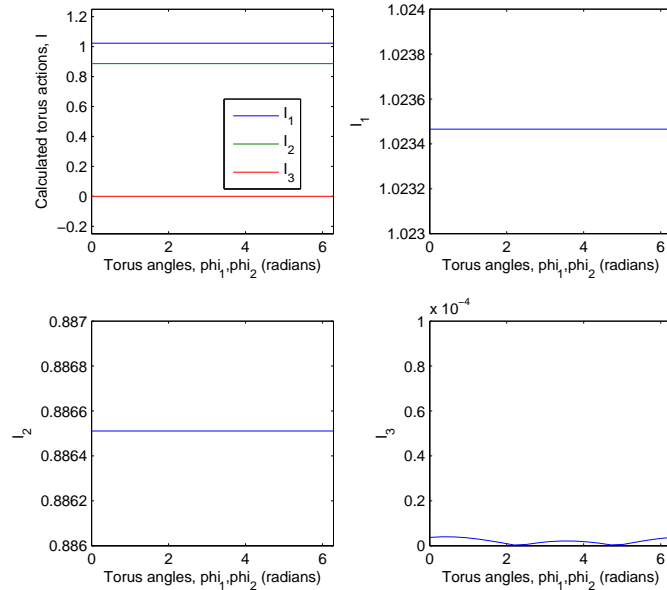
Figure 4.12.   Calculated torus actions at varying locations in φ_1 and φ_2 for 320km, 30° orbit

46

4.2 Satellite formations as KAM torus angle displacements

This section will give the nature and results of formation flight on the KAM tori. First, a description of the interpretation of torus angle displacements will be given, followed by the results of a survey of satellite drift after such separations. Then, the results of a more focused study on tight formations will be discussed.

4.2.1 Nature of φ_k displacements. To create a formation of two satellites, we choose a reference satellite in an orbit which lies on the torus and then create a second satellite whose orbit also lies on the torus, but separate it from the reference satellite by a change in one or more of the torus angles φ_k, per §3.3. Since, as mentioned in the section entitled *On the visualization of tori*, the torus space for 3-tori such as these are not easily intuitive, it is instructive to investigate the manifestations of torus-surface displacements in cartesian space. The following subsections give a short exposition of how these separations in the φ_k may, when possible, be interpreted in a physical sense.

4.2.1.1 Displacements in φ_1. Displacements in the torus angle φ_1 are perhaps the most intuitive and correspond to separations in the largest basis frequency, Ω_1. Following the discussion in Chapter III regarding the interpretations of the basis frequencies (c.f. §3.1.3), this φ_1 separation is, in physical space, roughly equivalent to a separation along the orbital path in the plane of the orbit. Figure (4.13) below displays an example of displacement along φ_1. In the figure, the coordinate frame is the Earth-centered inertial frame. The blue X represents the starting position of the reference "chief" satellite, the red X is the starting position of the displaced "deputy" satellite, and the blue and red lines represent the trajectories of the reference and displaced satellites, respectively. For demonstration purposes, the two satellites are propagated for less than one orbit to clearly show the initial separation.

4.2.1.2 Displacements in φ_2. Separations purely in the second torus angle, φ_2, manifest in the physical space as a rotation of the orbit plane itself around the ECI 3-axis, concordant with the discussion in §3.1.3; in other words, inducing a separation in φ_2 is to effectively "force" the regression of the node through a certain amount before placing
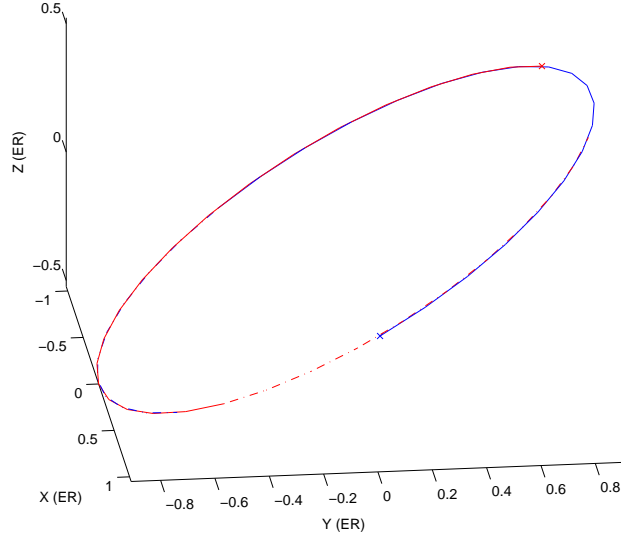
Figure 4.13.   Inertial trajectories of satellites after separation of $2\pi/3$ in φ_1

the second satellite. Figure (4.14) shows 3D plots of such a separation of magnitude $pi/4$ in the ECI frame: the left plot of Fig (4.14) gives a perspective view, while the right plot displays a "top-down" view, in which the angular separation of the lines of nodes for the two satellites is obvious. (Note: Although the orbits appear elliptical in the top view in Fig (4.14), they are in fact circular and inclined, which creates an elliptical projection on the ECI X-Y plane.) It is important to note that, regardless of the separation amount, the satellites' trajectories still lie on the same torus if they are created using the same KAM series.
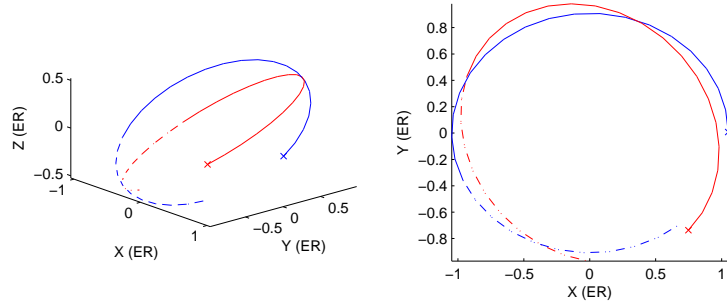
Figure 4.14.   Two views of inertial trajectories of satellites after separation of $pi/4$ in φ_2

48

4.2.1.3 Displacements in φ_3.   The third torus angle is arguably the most difficult to intuit and, since the magnitude of the third fundamental frequency Ω_3 is so small, is the most susceptible to modeling errors and is hardest to account for. Recall from §3.1.3 that the third fundamental frequency in our case, Ω_3, is representative of a motion akin to the apsidal regression rate. Since the orbits considered in this work are nearly, but not exactly, circular (meaning there is still some effective eccentricity), rotation through the third torus angle have the effect in physical space of displacement in the orbit's plane in a small ellipse with axes proportional to the residual eccentricity of the orbit. Figure (4.15) shows the inertial positions of the displacements resulting from varying φ_3 over the interval $[0, 2\pi]$, in the case of a 320km, $i = 30°$ orbit where the eccentricity $e \approx 0.0013$. The blue X marks represent the displacements after each equal increment of $\pi/10$ in φ_3 up to 2π. We note again that this figure is not an orbit itself, but rather for displacements in starting position from the reference ($\varphi_3 = 0$), marked with the red star in the figure.
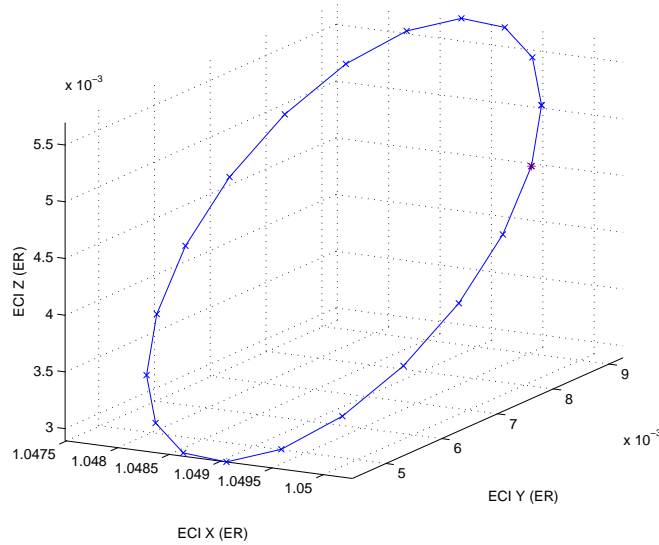
Figure 4.15.   Inertial displacements for $\varphi_3 = [0, 2\pi]$ manifested in physical space for a 320km, 30° orbit with $e \approx 0.0013$

4.2.2 Formation drift survey after initial toroidal angular displacements φ_k.   To begin the formation analysis, the separation drift of satellites was examined for varying

separations purely in the angles φ_k, as characterized in the previous section. As an example of the results, consider the case case involving φ_1 separations in the 320km, 30° orbit. Figures (4.16) and (4.17) show the magnitude of the satellites' relative distance minus the original separation distance over time for several different initial separation amounts. The initial separation listed at the top of each subplot is the direct distance from one satellite to the other found by subtracting the position vectors of the satellites at time t_0-this should not to be confused with the arc distance. The separation angle given for each subplot is in terms of φ_1 angle, which is what leads to the initial separation distance. Again, the distance given on the y-axis in the figures is the distance obtained by taking the magnitude of the vector from one satellite to the other at each time and then subtracting the initial separation vector magnitude. These figures clearly show a result which proved to be predominant throughout this work; it appears that when satellites are put into formation according to KAM torus angles, there are two main results: an oscillation in the satellite separation proportional to the initial separation between the satellites and a secular drift to some extent. In many cases, especially when investigating separations in φ_2, the secular drift is of such small magnitude compared to the magnitude of the oscillation that it is virtually undetectable in the plots.

To determine the secular drift in the satellite separation distance, the following simple technique was used: the separation data for each case (as plotted in the aforementioned figures) was fed into a routine which calculated the slope between each pair of peaks in the oscillating data, calculated the slope between each pair of valleys, took the average of each over the full time span, and then averaged the two slopes. The resulting data slope was then multiplied by the time span to determine the secular drift. As an example, for the 320km 30° orbit, Figure (4.18) shows the 10-day secular drift as a function of the φ_1 separation angle. As mentioned previously, the amount of secular drift seems to be proportional to the amount of initial separation. To gain a better idea of the relationship, the secular drift as a percent of the initial separation was plotted with respect to the initial φ_1 angle, shown in Figure (4.19). The secular drifts for the φ_1 case for this orbit remain less than one percent of the original separation distance for the angular separations examined.

50
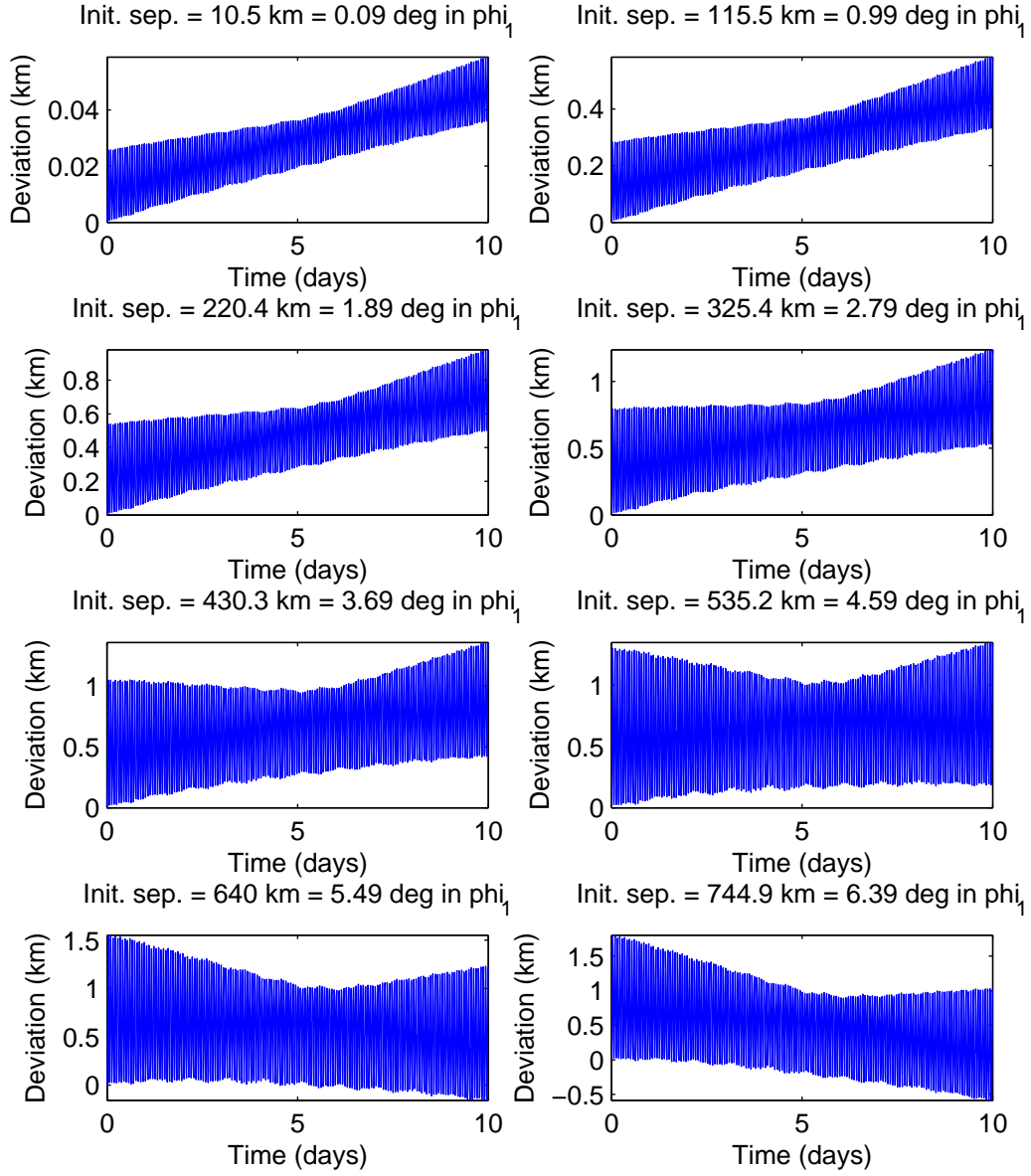
Figure 4.16.   Satellite separation deviation from initial value over 10 days after varying initial separations in φ_1

51
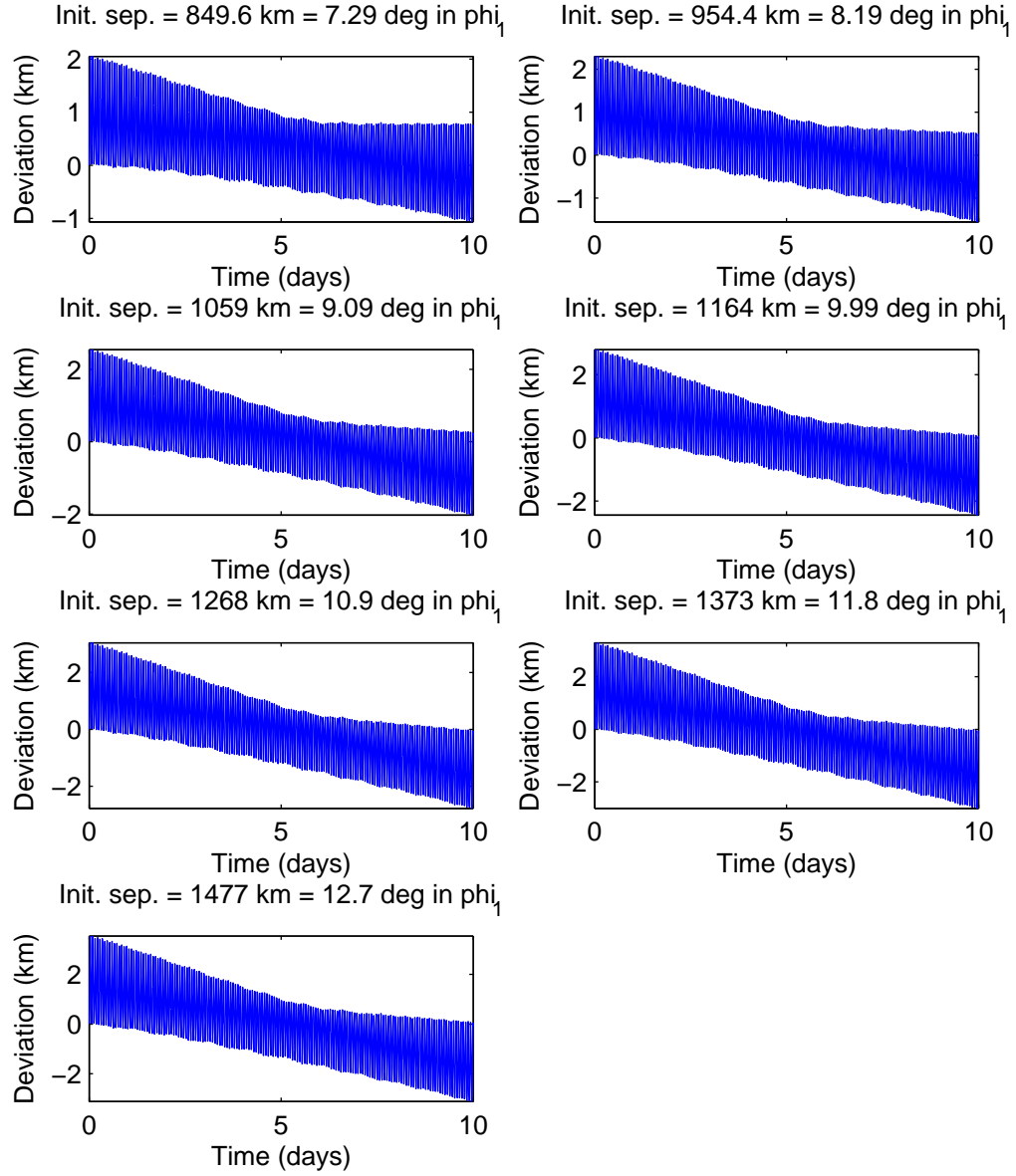
Figure 4.17.   Satellite separation deviation from initial value over 10 days after varying
initial separations in φ_1 (cont.)
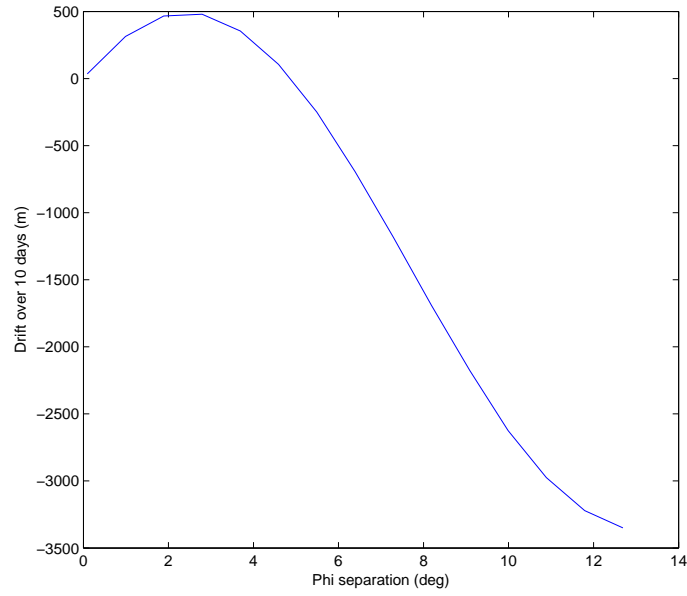
Figure 4.18.   Secular drift between satellites over 10 days vs. initial separations in φ_1 for 320km, $i = 30°$ orbit
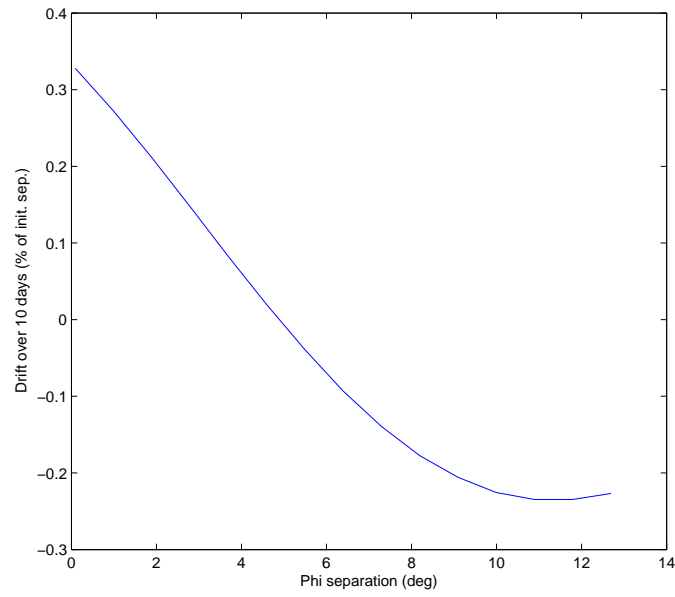
Figure 4.19.   Secular drift (in percentage of initial separation) between satellites over 10 days vs. initial φ_1 separation for 320km, $i = 30°$ orbit

The distance results for each of the four orbits and each φ_k are included in Appendices A through D for reference and, in the interest of simplicity and brevity, will not be shown here. However, Tables 4.1 through 4.4 give a summary of selected results from the drift analysis survey. There are several important points to note from these data. First, as shown above, the oscillatory amplitude and secular drift both increase with increasing initial separation distance; however, the drift as a percentage of the original separation stays relatively low, being always below 1 percent (and usually below 0.5 percent) for displacements in φ_1 and φ_2 in the cases surveyed. Second, as shown in the tables and in the figures in the Appendices involving φ_2, there is a seemingly bounded oscillation with very little relative secular growth. The oscillation is unavoidable and is a direct result of the separation of the orbital planes by rotation about the ECI z-axis (recall the example separation in Figure (4.14)). Third, drift and oscillation after φ_3 separations seem to be much more erratic and ill-behaved than after separations in φ_1 and φ_2. It is the speculation of this author that, as alluded to in §4.2.1.3, the very small but nonzero eccentricity causes a low magnitude oscillation from the change in position of the orbit's argument of perigee ω_p.

Table 4.1. Selected drift results of initial displacements in φ_k for 320km, 15° orbit over 10 days

Torus angle	Initial separation (deg)	Initial separation (m)	Oscillation amplitude (m)	Drift (m)	Drift (percent)
1	0.09	1.049e+004	27.04	1.73	0.01649
1	2.79	3.252e+005	838.2	-186.2	-0.05726
1	7.29	8.493e+005	2186	-1007	-0.1185
1	9.99	1.163e+006	2988	-1243	-0.1069
1	12.69	1.476e+006	3784	-1100	-0.07449
2	0.36	4.209e+004	1378	-7.473	-0.01775
2	5.76	6.732e+005	2.203e+004	281.1	0.04176
2	21.96	2.552e+006	8.358e+004	-2869	-0.1124
2	48.96	5.552e+006	1.818e+005	-2833	-0.05102
2	70.56	7.738e+006	2.534e+005	-4991	-0.06449
2	92.16	9.65e+006	3.161e+005	-9286	-0.09622
2	103	1.048e+007	3.433e+005	-1.012e+004	-0.09651
3	0.36	122.3	59.52	0.7927	0.6483
3	5.76	1941	952	12.56	0.6468
3	21.96	7126	3609	144.2	2.023
3	48.96	1.42e+004	7851	339.8	2.392
3	70.56	1.789e+004	1.095e+004	595.6	3.329
3	92.16	1.967e+004	1.365e+004	-962.7	-4.895
3	103	1.993e+004	1.482e+004	-267.3	-1.341

Table 4.2.   Selected drift results of initial displacements in φ_k for 320km, 30° orbit over 10 days

Torus angle	Initial separation (deg)	Initial separation (m)	Oscillation amplitude (m)	Drift (m)	Drift (percent)
1	0.09	1.05e+004	19.62	34.41	0.3278
1	0.99	1.155e+005	215.8	314.3	0.2722
1	2.79	3.254e+005	608.4	479.6	0.1474
1	7.29	8.496e+005	1589	-1183	-0.1393
1	9.99	1.164e+006	2175	-2624	-0.2255
1	12.69	1.477e+006	2756	-3350	-0.2268
2	0.36	4.209e+004	5416	221.6	0.5265
2	5.76	6.731e+005	8.656e+004	4463	0.6631
2	21.96	2.552e+006	3.285e+005	1.132e+004	0.4435
2	48.96	5.551e+006	7.148e+005	2.418e+004	0.4356
2	70.56	7.738e+006	9.964e+005	3.278e+004	0.4236
2	92.16	9.65e+006	1.243e+006	3.977e+004	0.4122
2	103	1.048e+007	1.35e+006	4.142e+004	0.3951
3	0.36	105.6	54.32	-0.7253	-0.6869
3	5.76	1662	868.6	-39.27	-2.363
3	21.96	5942	3292	-14.83	-0.2496
3	48.96	1.133e+004	7164	-141.6	-1.249
3	70.56	1.385e+004	9985	209.5	1.513
3	92.16	1.502e+004	1.246e+004	28.76	0.1915
3	103	1.531e+004	1.353e+004	-657.1	-4.291

Table 4.3. Selected drift results of initial displacements in φ_k for 630km, 15° orbit over 10 days

Torus angle	Initial separation (deg)	Initial separation (m)	Oscillation amplitude (m)	Drift (m)	Drift (percent)
1	0.09	1.098e+004	25.34	5.025	0.04577
1	0.99	1.208e+005	278.8	40.52	0.03354
1	2.79	3.404e+005	785.5	36.21	0.01064
1	7.29	8.888e+005	2049	-278.7	-0.03135
1	9.99	1.217e+006	2801	-468.8	-0.03851
1	12.69	1.545e+006	3548	-508.8	-0.03293
2	0.36	4.404e+004	1449	104.6	0.2376
2	5.76	7.043e+005	2.317e+004	2052	0.2914
2	21.96	2.67e+006	8.788e+004	5043	0.1889
2	48.96	5.809e+006	1.912e+005	1.305e+004	0.2246
2	70.56	8.096e+006	2.665e+005	1.826e+004	0.2256
2	92.16	1.01e+007	3.323e+005	2.254e+004	0.2233
2	103	1.097e+007	3.61e+005	2.304e+004	0.2101
3	0.36	116.8	57.24	-2.388	-2.046
3	5.76	1853	915.4	2.153	0.1162
3	21.96	6794	3468	-2.579	-0.03796
3	48.96	1.351e+004	7547	146.1	1.081
3	70.56	1.699e+004	1.052e+004	553.3	3.256
3	92.16	1.866e+004	1.312e+004	119.3	0.6394
3	103	1.89e+004	1.425e+004	180.8	0.9568

Table 4.4.   Selected drift results of initial displacements in φ_k for 630km, 30° orbit over 10 days

Torus angle	Initial separation (deg)	Initial separation (m)	Oscillation amplitude (m)	Drift (m)	Drift (percent)
1	0.09	1.098e+004	18.44	23.72	0.216
1	0.99	1.208e+005	202.8	237.5	0.1966
1	2.79	3.405e+005	571.5	504.9	0.1483
1	7.29	8.891e+005	1492	60.94	0.006854
1	9.99	1.218e+006	2043	-651.9	-0.05353
1	12.69	1.546e+006	2588	-1260	-0.08151
2	0.36	4.403e+004	5694	-46.43	-0.1054
2	5.76	7.042e+005	9.105e+004	-474.3	-0.06735
2	21.96	2.67e+006	3.456e+005	-7336	-0.2748
2	48.96	5.808e+006	7.517e+005	-1.392e+004	-0.2397
2	70.56	8.096e+006	1.048e+006	-1.955e+004	-0.2415
2	92.16	1.01e+007	1.307e+006	-2.451e+004	-0.2428
2	103	1.097e+007	1.419e+006	-2.791e+004	-0.2545
3	0.36	101.3	52.6	-1.822	-1.798
3	5.76	1594	841.3	32.33	2.028
3	21.96	5693	3188	-107.9	-1.895
3	48.96	1.084e+004	6936	-406.4	-3.751
3	70.56	1.323e+004	9669	87.26	0.6597
3	92.16	1.435e+004	1.206e+004	334.6	2.332
3	103	1.465e+004	1.31e+004	70.78	0.4831

4.2.3 Tight formation detailed analysis. While the behavior of satellites at large displacements on the torus is interesting, the real promise of KAM formation design seems to lie in analysis close-proximity formation flight. To further investigate the utility of a KAM approach to formation design, certain special cases were examined using similar methodology to that of the previous section. First, a tight formation of five satellites flying in a 320km, 15° orbit was analyzed. The satellites were separated in the torus space by , $\delta\varphi_0 = 0.0001°$ in the four cardinal torus 1-2 plane directions, which corresponds to approximately 11.5 meters of physical separation. Figure (4.20) shows the separations of the satellites both in the torus space and in physical cartesian space.   After defining
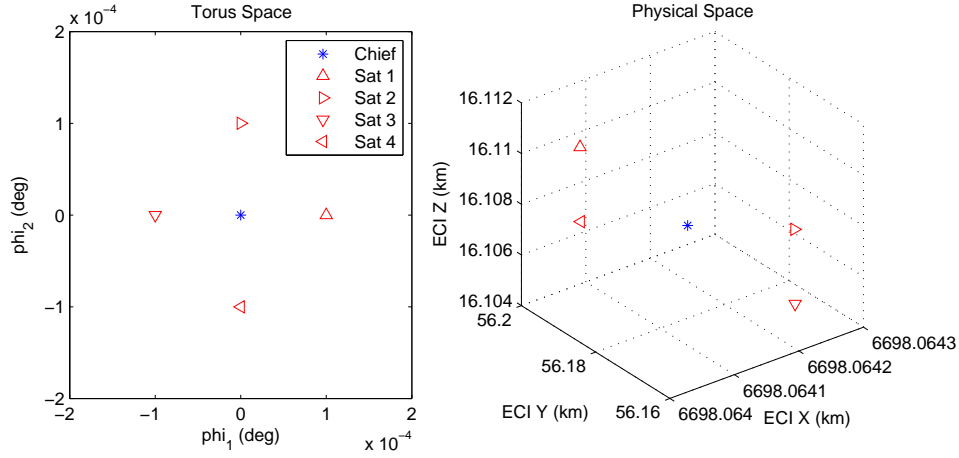
Figure 4.20.   Initial position in torus space and cartesian space of satellite cluster for first close formation analysis in 320km, 15° orbit, $\delta\varphi = 0.0001°$

the initial conditions of the satellite as such, the trajectory of each satellite was obtained through numerical integration over a period of 60 days. The position vector for each satellite was then compared to that of the chief (center) satellite at each time step to determine the relative motion of the satellite cluster. The drift results for each ancillary satellite with respect to the chief are shown in Figure (4.21), which shows the distance of each satellite from the chief, and in Figure (4.22), which shows the drift from the

59

Figure 4.21.   Cluster distance from chief satellite for first close formation analysis in 320km, 15° orbit, $\delta\varphi_0 = 0.0001°$

Figure 4.22.   Cluster drift from initial separations for first close formation analysis in 320km, 15° orbit, $\delta\varphi_0 = 0.0001°$

original separation distance. The two satellites separated purely along the φ_2 axis at $\varphi_2 = -0.0001°, 0.0001°$ show, as expected, the largest oscillation, concurrent with the previous discussion on the nature of φ_2 displacements. In general, however, the maximum secular drift of any satellite away from the chief is approximately 0.02 meters per 60 days, which corresponds to an extraordinarily small drift velocity of approximately 3.86 nanometers per second.

Another cluster investigated was in a somewhat dynamically harsher $i = 30°$ orbit at the same 320km altitude. The satellites were also in the same cruciform configuration in the torus space as the previous case, with $\delta\varphi_0 = 0.0001°$ as given on the left plot of Figure (4.20), with the positions changing in proportion in the physical space according to the different orbital configuration. The separation plots for this second case are shown in Figs. (4.23) and (4.24). The maximum secular drift experienced by the satellites in the cluster is noticeably higher because of the higher inclination, reaching approximately 0.25m over 60 days, corresponding to an average secular drift rate of approximately 48.2 nanometers per second.

Three additional trials of tight formations were examined: one for a 320km, $i = 15°$ with a larger separation of $\delta\varphi_0 = 0.001°$, one for a higher 630km, $i = 15°$ orbit at the small separation of $\delta\varphi_0 = 0.0001°$, and one for a 630km, $i = 30°$ orbit at a separation of $\delta\varphi_0 = 0.001°$. Table 4.5 shows a summary of the results from these runs, and the data may be seen in graphical form through plots in Appendix E. The table shows that the highest drift rate occurs in the last case mentioned, which is understandable due to its higher inclination and larger physical separation; however, the drift rate is still only on the order of 0.313 $\mu m/s$.
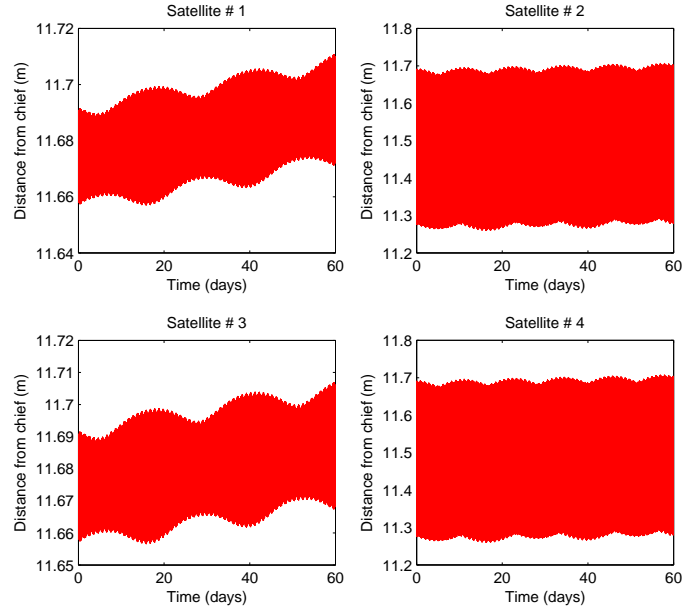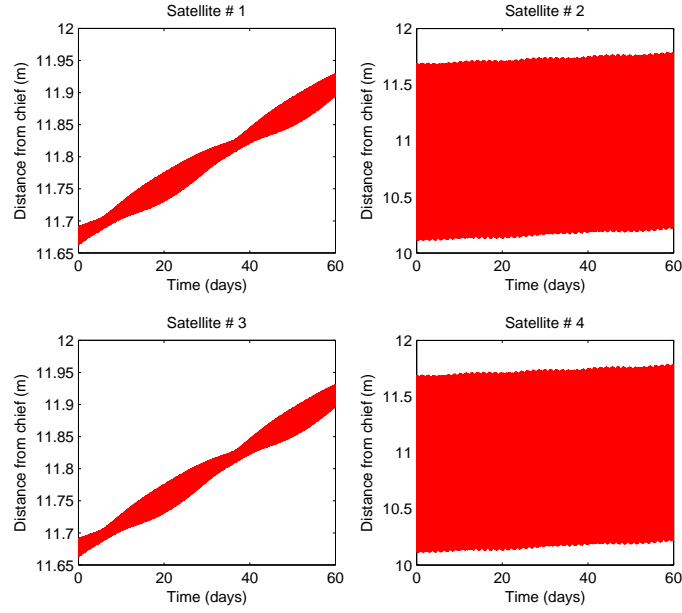
Figure 4.23.   Cluster distance from chief satellite for first close formation analysis in 320km, 30° orbit, $\delta\varphi_0 = 0.0001°$
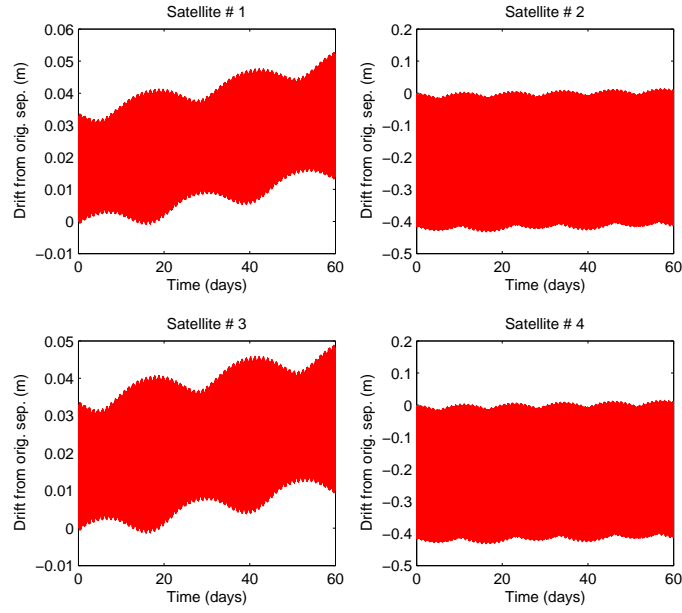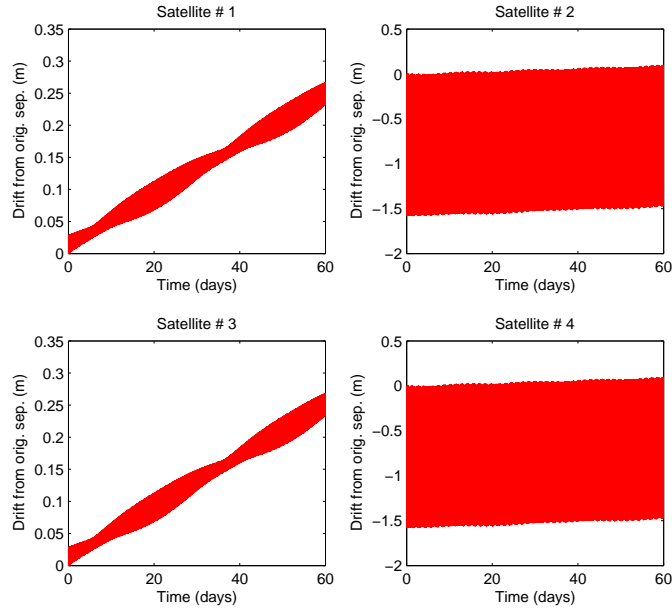

Figure 4.24.   Cluster drift from initial separations for first close formation analysis in 320km, 30° orbit, $\delta\varphi_0 = 0.0001°$

Table 4.5.   Results of tight formation analysis for various orbits and separations

Sat. No.	Initial sep. from chief (m)	Avg. Oscillation amplitude (m)	Drift over 60 days (m)	Drift rate (m/s)
Alt $= 320$km, $i = 15°$, $\delta\varphi_0 = 0.0001$
1	11.66	0.03379	0.01425	2.75e-009
2	11.69	0.3827	-0.01179	-2.275e-009
3	11.66	0.03378	0.01035	1.996e-009
4	11.69	0.3827	-0.01087	-2.097e-009

Sat. No.	Initial sep. from chief (m)	Avg. Oscillation amplitude (m)	Drift over 60 days (m)	Drift rate (m/s)
Alt $= 320$km, $i = 15°$, $\delta\varphi_0 = 0.001$
1	116.6	0.3378	0.1199	2.312e-008
2	116.9	3.827	-0.1161	-2.24e-008
3	116.6	0.3378	0.1164	2.246e-008
4	116.9	3.827	-0.1159	-2.235e-008

Sat. No.	Initial sep. from chief (m)	Avg. Oscillation amplitude (m)	Drift over 60 days (m)	Drift rate (m/s)
Alt $= 320$km, $i = 30°$, $\delta\varphi_0 = 0.0001$
1	11.66	0.03303	0.2361	4.555e-008
2	11.69	1.499	0.1301	2.509e-008
3	11.66	0.03303	0.2378	4.587e-008
4	11.69	1.499	0.128	2.47e-008

Sat. No.	Initial sep. from chief (m)	Avg. Oscillation amplitude (m)	Drift over 60 days (m)	Drift rate (m/s)
Alt $= 630$km, $i = 15°$, $\delta\varphi_0 = 0.0001$
1	12.2	0.03303	0.2361	4.555e-008
2	12.23	1.499	0.1301	2.509e-008
3	12.2	0.03303	0.2378	4.587e-008
4	12.23	1.499	0.128	2.47e-008

Sat. No.	Initial sep. from chief (m)	Avg. Oscillation amplitude (m)	Drift over 60 days (m)	Drift rate (m/s)
Alt $= 630$km, $i = 30°$, $\delta\varphi_0 = 0.001$
1	122	0.3048	1.626	3.137e-007
2	122.3	15.75	1.029	1.985e-007
3	122	0.3048	1.626	3.136e-007
4	122.3	15.75	1.028	1.984e-007

4.3 Atmospheric drag effects on KAM tori

When one examines only the relative motion between two satellites in circular orbits on the same KAM torus, atmospheric drag effects do not play an important role, as long as the satellites are identical in drag mass, cross-sectional area and shape and, if unsymmetric, tend to fly in the same attitude- these are certainly the case for many groups of satellites of interest in formation design. However, when positioning of the satellites in an "absolute" or an Earth-fixed sense is important, which is the case when, for example, a surveillance satellite must overfly some area of the Earth with some frequency, atmospheric drag begins to play a more important role in the orbital calculations. Though not the main focus of this paper, a limited study was performed to determine the effects of atmospheric drag on the KAM tori of Earth satellites.

Even before beginning any numerical analysis regarding drag, we may derive some of the its effects in general on the KAM torus by simple intuition. As mentioned in §2.2.2, the effect of drag on an orbit is a decrease in the semi-major axis through circularization and, once circularity has been reached, a lowering of the orbital altitude until impact. Elementary orbital mechanics shows that an orbiting object whose altitude is decreasing will experience an increase in velocity. We would expect, then, since the satellite is moving faster, that the fundamental KAM torus frequencies would increase as the orbit decays. However, the satellite's descent due to drag is a physical manifestation of energy degeneracy in the dynamical system; i.e., the system is no longer isoenergetic. This means that the satellite no longer lies on the KAM torus we have so carefully characterized and calculated, since one of the fundamental assumptions made in Chapter III involved an isoenergetic system with a small, conservative perturbation to a Hamiltonian system.

On the surface, it appears that atmospheric drag renders KAM representation of orbits useless. On the contrary, if the drag force can be characterized well enough, it should still be possible to gain information from the KAM torus. To very briefly investigate this, an analysis was performed in which a satellite began in a 320km, 30° inclination orbit. To include the effects of air drag, this author proposes the use of a Rayleigh dissipative function [14] in terms of the $\dot{q}_k$ inserted into the Hamiltonian, so that Hamilton's functions

64

become

$$\dot{q}_k = \frac{\delta H}{\delta p_k}$$

$$\dot{p}_k = -\frac{\delta H}{\delta q_k} - \chi \frac{\delta F_R}{\delta \dot{q}_k} \tag{4.5}$$

where χ is a coefficient dependent on spacecraft characteristics and the atmospheric density given as

$$\chi = \rho \frac{C_d A}{m} = \frac{\rho}{\beta} \tag{4.6}$$

and F_R is a Rayleigh function

$$F_R = \frac{1}{6} \left(\dot{q}_1 + \dot{q}_2 + \dot{q}_3 \right)^{\frac{3}{2}} \tag{4.7}$$

When integrating Eqns. (4.5) to provide trajectory data, the instantaneous atmospheric density ρ in (4.6) was calculated at every time step using a basic exponential atmospheric model for the Earth (c.f. [19] for a more detailed explanation). A more accurate density model, if available, could obviously be utilized in its place.

A reference trajectory was first integrated over $t = [-T, T]$ without drag and a KAM torus constructed for it. Next, the same initial conditions were integrated forwards with the drag acceleration included. Then, the state vectors of this "drag-perturbed" trajectory at each time from 1 to 64 time units were extracted. These state vectors were then used as initial conditions for new forward and backward integrations, again over $t = [-T, T]$, and KAM tori constructed for each trajectory. In this way, we have found, in essence, *osculating KAM tori*, in that the tori are what would be obtained if one could instantaneously "switch off" the drag force at any point in a trajectory and analyze the motion of the new orbit.

The tori basis frequencies are necessarily calculated in order to construct new KAM tori for each state of the drag-perturbed trajectory. The set of the basis frequencies for the constructed tori then will show the trend in the frequencies as drag acts upon the satellite. Figures (4.25) through (4.26) show the change in each of the three basis frequencies as found through the above analysis on a 320km, 30° orbit. Since this was purely a demonstrative investigation, for the sake of computational efficiency, the geopotential expansion was only

included to order and degree $m, n = 4$ rather than the usual $m, n = 20$ limit used elsewhere throughout this work.   It is clear from the figures that the fundamental frequencies display

Figure 4.25.   Change in Ω_1 due to drag in a 320km, 30° orbit, including geopotential expansion to $m, n = 4$

the expected increase due to the lowering of the orbit; also, all three display the same roughly linear behavior for this relatively short time, though they grow at different rates proportional to the initial frequency magnitude. The above results serve to illustrate that, even though the orbit of a satellite acted on by an energy-dissipative force like drag will not stay on the same KAM torus, the torus evolves in a way consistent with the expected and observed orbital deterioriation.
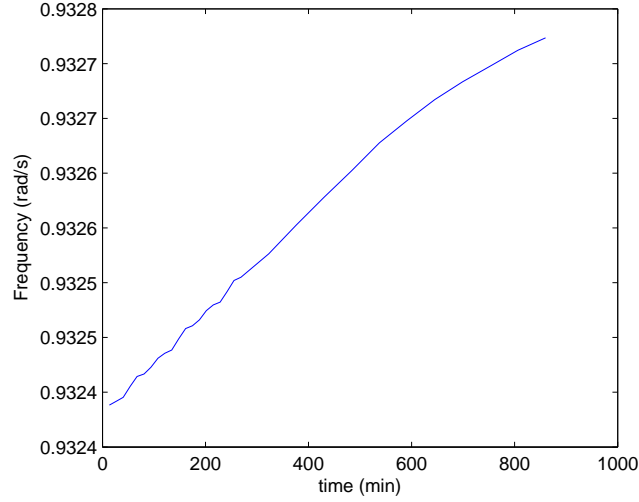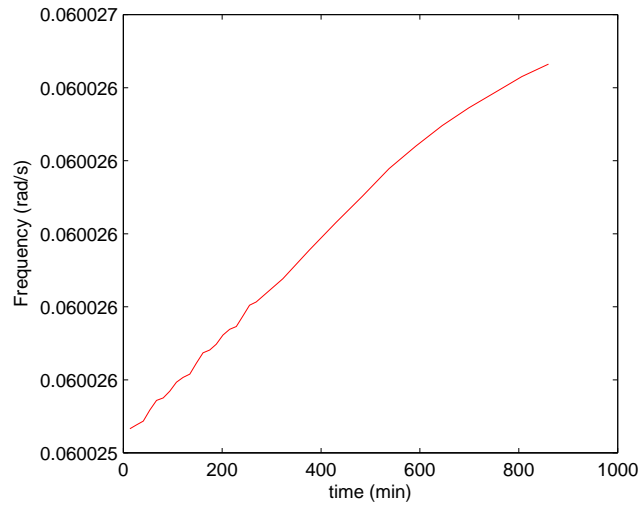
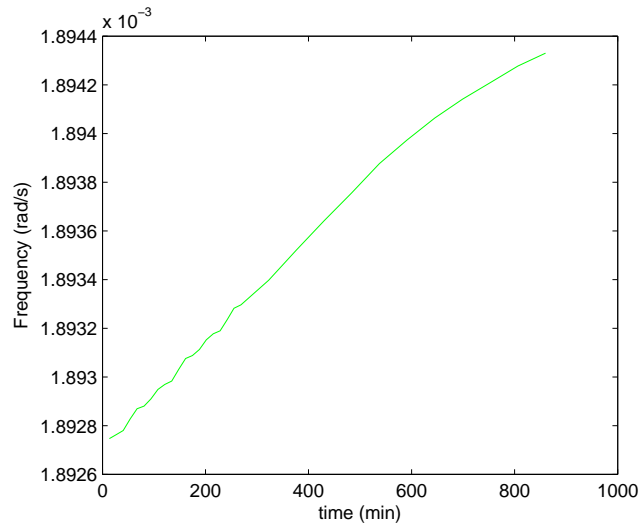Figure 4.26.   Change in Ω_2 due to drag in a 320km, 30° orbit, including geopotential expansion to $m, n = 4$

Figure 4.27.   Change in Ω_3 due to drag in a 320km, 30° orbit, including geopotential expansion to $m, n = 4$

67

V. Conclusions

This chapter will posit conclusions derived from the results of the work presented throughout Chapter IV. Torus construction, its limitations and applicability will be discussed, followed by the key conclusions of formation design on the torus. Finally, recommendations for future work will be given.

5.1 Torus Construction

As seen in Chapter IV, the KAM tori derived/calculated for this work have been utilized to accurately describe the positions of virtual satellites in their orbits to within 0.1 meter over one year in some cases- this obviously demonstrates that KAM is a powerful tool with some degree of utility in orbital mechanics and design. This section will describe the limitations of torus construction and thereby postulations regarding its applicability.

5.1.1 Limitations and considerations in the KAM fitting process. As mentioned above, the methods used in this work to construct KAM tori have yielded promising and potentially valuable results; these must be tempered, however, by the reality of limitations inherent in the process and their associated impacts on the potential usefulness of the system. For example, the results of Chapter IV showed a trend in which tori of orbits of higher altitudes were determinable to higher accuracy using fewer KAM series terms than their lower-altitude counterparts sharing the same inclination. However, the opposite trend was found with regards to changing inclination; as inclination increases, the orbit's torus is generally more difficult to obtain to any high degree of accuracy. Indeed, orbits at both 320km and 630km altitudes were examined by the current author whose inclinations were as high as $3\pi/4 \approx 43°$, the tori of which were only able to be calculated with residuals on the order of $650km$ over one year.

This author believes that the phenomenon of KAM tori becoming more difficult to determine accurately with increasing inclination is directly an effect of the shrinking of the third basis frequency as seen in Figure (3.6) as $i \to i^*$, where $i^* \approx 63.4°$ is the critical inclination discussed in §3.1.3. As Ω_3 falls closer and closer to a zero value, the trajectory knowledge must be more and more accurate over a longer and longer time to accurately

determine the basis frequencies with the methodology in Chapter III. In the limit where $i = i^*$, the basis frequency set $\bar{\Omega} = [\Omega_1, \Omega_2, \Omega_3]$ would be said to be *commensurable* (i.e., two or more elements of the set have a common divisor), violating the diophantine condition mentioned in [9] and leading to an exacerbated problem of small divisors. In this case, the torus would be practically incalculable. In this case, however, where $|i - i^*| \approx 0$, it is expected that the torus could be described with reasonable accuracy in terms of the set of only two fundamental frequencies, $\bar{\Omega} = [\Omega_1, \Omega_2]$. Such an investigation was beyond the scope of this work, but it was determined that the transition region where $0.0017 \, rad/s > \Omega_3 > 0$ leads to a severe decline in the accuracy of the results.

Similarly, one also encounters a commensurability issue when two of the Ω_k are very close to low integer multiples of each other, even if they are nowhere close to zero-valued. This would be most frequently encountered as a relationship between the two largest frequencies, and would only be soluble with trajectory knowledge of greater accuracy to resolve the two frequencies

5.1.2 Applicability of KAM theorem. Of pivotal importance in the KAM process, and intimately related to the commensurability considerations discussed above, is the trajectory knowledge of the orbit whose KAM torus is sought. In the current work, the trajectory knowledge was obtained through numerical integration, which is much more easily performed than physical on-orbit determination to a high degree of accuracy. In the author's estimation, the main limitation on the applicability of KAM torus construction to-date is the extremely long periods of accurate trajectory knowledge required to create usable KAM tori. It is indeed quite rare, due to the inherent error in any real-world tracking or position determination system and the necessity of spacecraft maneuvering, to know the true trajectory of a satellite well enough to very accurately implement KAM theorem. Little has shown the results of such investigations of actual satellites' tori. Even in the "ideal" case of numerically integrated data, there is a finite limit of accuracy (as discussed in Chapter III and above) which casts accuracy bounds on KAM torus determination.

5.2 KAM Formation Flight

The results of Chapter IV show that an accurate KAM torus for a given orbit can yield useful fundamental knowledge of the orbit's behavior, including its major modes of motion and their frequencies and proportions. Additionally, it was shown that formations may be configured on the KAM torus in both tight (close-lying) and wide formations to obtain physical separations with varying levels of relative oscillation and secular drift. In the survey of wide formations, the satellites generally experienced secular drifts of less than 0.5 percent of the original separations in torus angles φ_1 and φ_2 over 10 days, even with separations of as much as 1-5 million meters. It seems that the amount of secular drift between satellites and the oscillation distance amplitude is proportional to the amount of separation, which casts doubt on the utility of this method for designing constellations of satellites separated by large distances.

The KAM method seems to show promise, however, in genesis of satellite clusters with small $\delta\varphi_0$. Orbits of satellite clusters separated by ten to one hundred meters according to KAM tori showed drift rates in the nanometer to micrometer range over 60 day integration windows. If, in fact, satellites can be placed on a KAM torus with such angular separations, the low and accurate thrust of electric propulsive devices could easily overcome such a drift rate.

5.3 Recommendations for Future Study

It is the author's opinion that, in order to transform KAM theory into a viable tool for astrodynamicists, certain additional areas in this promising field should be investigated and characterized. First, a purely informational survey of torus construction for different altitude and inclination combinations should be performed, determining the steps and basis frequency number/characteristics required for each type of orbit. The envisioned result of such an effort would be a sort of database of KAM torus parameters for Earth orbits. Second, investigation of the possibility of applying KAM torus construction methodology to orbits of varying eccentricities should be executed. Third, additional work should be completed with a focus on developing new and more efficient techniques for determining torus frequencies and torus coefficients – in essence, to search for a more direct map

$\mathcal{M}: (q, p) \to (I, \varphi)$, the ideal map mentioned at the beginning of Chapter III. Such effort would seek to reduce or eliminate the need for extensive numerical integration and/or highly accurate trajectory knowledge over exceedingly long times in constructing KAM torus models for an orbit. Fourth, the problem of maneuvering onto KAM tori should be investigated. The author is aware of current work with some success in this area, and feels strongly that this is a vital area of continued research, with the ideal result of allowing for flight on specified KAM tori in spite of the intrinsically limited precision of launch and orbital insertion capabilities. Finally, in the area of KAM formation design, it would be beneficial to fully and extensively characterize the correlation between torus angle displacements and their associated displacements in the physical space, with a focus on the ability to "fix" satellites into the desired relative physical positions while harnessing the drift advantages of their being on the same KAM torus.
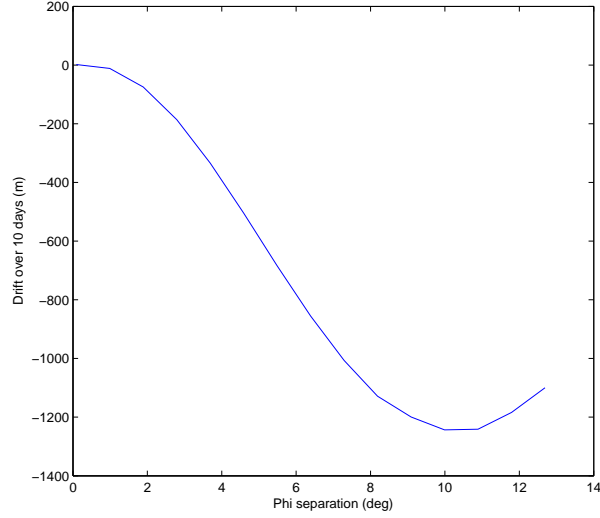
Figure A1.   Secular drift between satellites over 10 days vs. initial φ_1 separation for 320km, $i = 15°$ orbit

Table A1.   Drift results of initial displacements in φ_1 for 320km, $15°$ orbit over 10 days

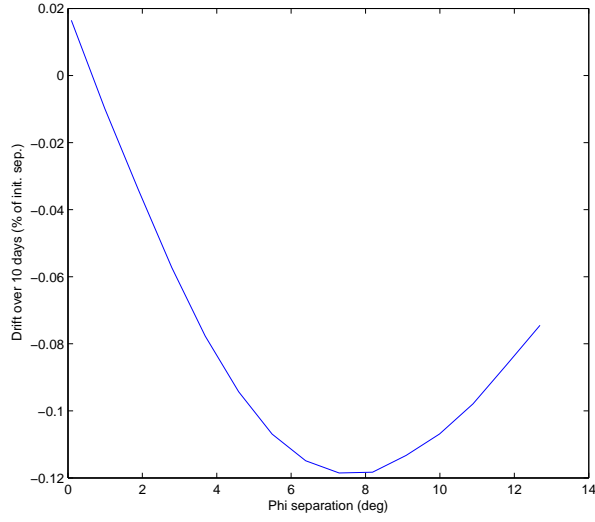| Torus angle	Initial sep. (deg)	Initial separation (m)	Oscillation amplitude (m)	Drift (m)	Drift (percent)
1	0.09	1.049e+004	27.04	1.73	0.01649
1	0.99	1.154e+005	297.4	-11.37	-0.009852
1	1.89	2.203e+005	567.8	-74.86	-0.03398
1	2.79	3.252e+005	838.2	-186.2	-0.05726
1	3.69	4.301e+005	1108	-334.2	-0.0777
1	4.59	5.35e+005	1378	-504.5	-0.09431
1	5.49	6.398e+005	1648	-684	-0.1069
1	6.39	7.446e+005	1917	-855.5	-0.1149
1	7.29	8.493e+005	2186	-1007	-0.1185
1	8.19	9.54e+005	2454	-1129	-0.1183
1	9.09	1.059e+006	2722	-1199	-0.1133
1	9.99	1.163e+006	2988	-1243	-0.1069
1	10.89	1.268e+006	3254	-1241	-0.09791
1	11.79	1.372e+006	3520	-1184	-0.08628
1	12.69	1.476e+006	3784	-1100	-0.07449

Figure A2.   Secular drift (in percentage of initial separation) between satellites over 10 days vs. initial φ_1 separation for 320km, $i = 15°$ orbit

Table A2.   Drift results of initial displacements in φ_2 for 320km, 15° orbit over 10 days

Torus angle	Initial sep. (deg)	Initial separation (m)	Oscillation amplitude (m)	Drift (m)	Drift (percent)
2	0.36	4.209e+004	1378	-7.473	-0.01775
2	5.76	6.732e+005	2.203e+004	281.1	0.04176
2	11.16	1.303e+006	4.263e+004	699.2	0.05367
2	16.56	1.93e+006	6.318e+004	-1301	-0.06745
2	21.96	2.552e+006	8.358e+004	-2869	-0.1124
2	27.36	3.169e+006	1.037e+005	-1465	-0.04625
2	32.76	3.778e+006	1.237e+005	-1730	-0.04579
2	38.16	4.38e+006	1.434e+005	-5276	-0.1205
2	43.56	4.971e+006	1.628e+005	-6069	-0.1221
2	48.96	5.552e+006	1.818e+005	-2833	-0.05102
2	54.36	6.12e+006	2.004e+005	-2946	-0.04814
2	59.76	6.675e+006	2.186e+005	-6848	-0.1026
2	65.16	7.214e+006	2.363e+005	-7495	-0.1039
2	70.56	7.738e+006	2.534e+005	-4991	-0.06449
2	75.96	8.245e+006	2.7e+005	-5605	-0.06799
2	81.36	8.733e+006	2.86e+005	-9124	-0.1045
2	86.76	9.202e+006	3.014e+005	-1.025e+004	-0.1114
2	92.16	9.65e+006	3.161e+005	-9286	-0.09622
2	97.56	1.008e+007	3.3e+005	-9012	-0.08942
2	103	1.048e+007	3.433e+005	-1.012e+004	-0.09651

Table A3.   Drift results of initial displacements in φ_3 for 320km, 15° orbit over 10 days

Torus angle	Initial sep. (deg)	Initial separation (m)	Oscillation amplitude (m)	Drift (m)	Drift (percent)
3	0.36	122.3	59.52	0.7927	0.6483
3	5.76	1941	952	12.56	0.6468
3	11.16	3723	1843	-65.99	-1.773
3	16.56	5455	2730	113.1	2.073
3	21.96	7126	3609	144.2	2.023
3	27.36	8725	4481	-44.89	-0.5146
3	32.76	1.024e+004	5344	-390.1	-3.81
3	38.16	1.166e+004	6196	-715.9	-6.138
3	43.56	1.299e+004	7034	150.5	1.159
3	48.96	1.42e+004	7851	339.8	2.392
3	54.36	1.53e+004	8653	476.4	3.113
3	59.76	1.629e+004	9439	267.1	1.64
3	65.16	1.715e+004	1.021e+004	-226.4	-1.32
3	70.56	1.789e+004	1.095e+004	595.6	3.329
3	75.96	1.851e+004	1.166e+004	-186.2	-1.006
3	81.36	1.901e+004	1.235e+004	-250.6	-1.319
3	86.76	1.939e+004	1.302e+004	-286.7	-1.478
3	92.16	1.967e+004	1.365e+004	-962.7	-4.895
3	97.56	1.984e+004	1.425e+004	87.19	0.4394
3	103	1.993e+004	1.482e+004	-267.3	-1.341

Figure A3.   Satellite separation deviation from initial value over 10 days after varying initial separations in φ_1 for 320km, $i = 15°$ orbit
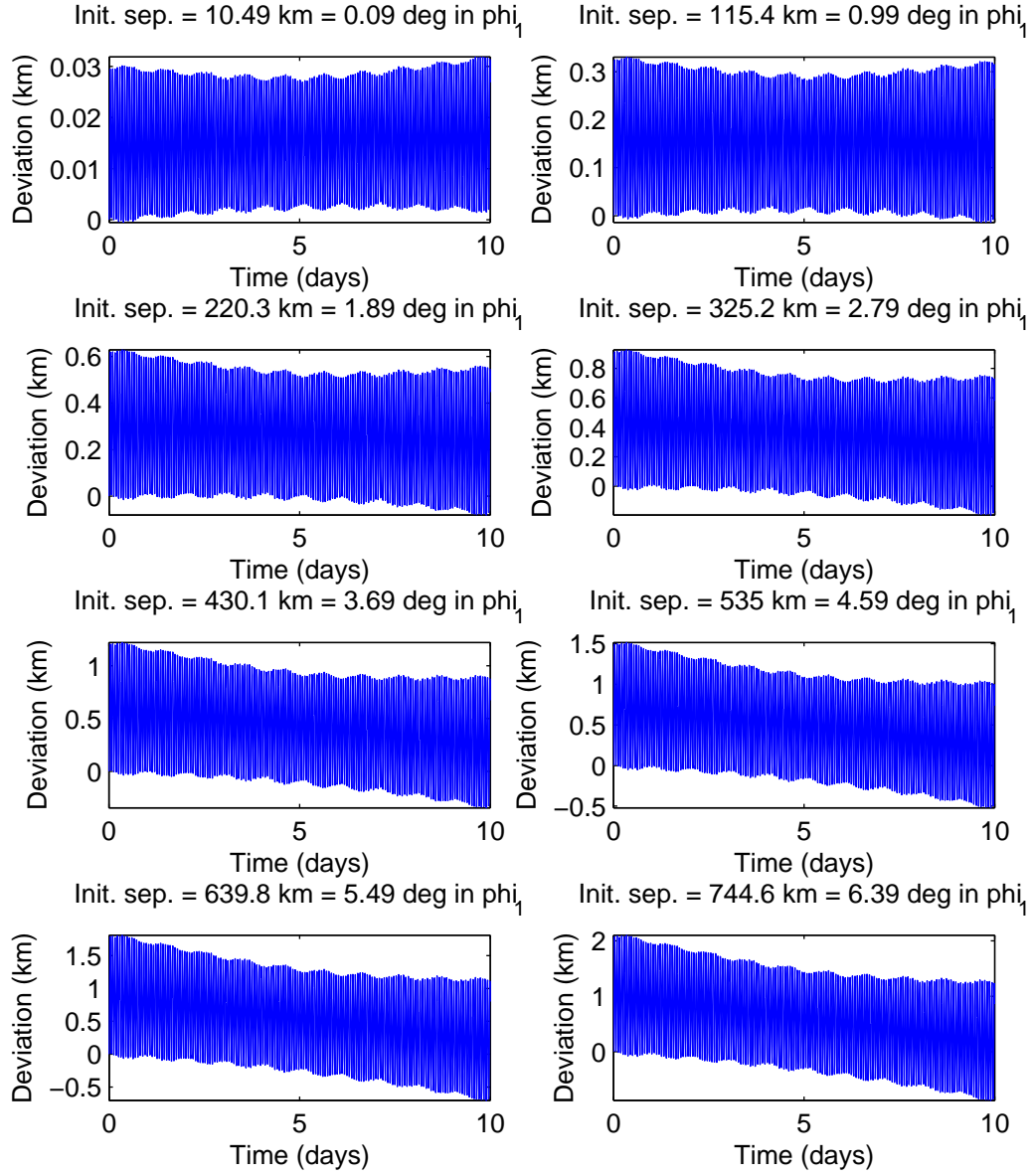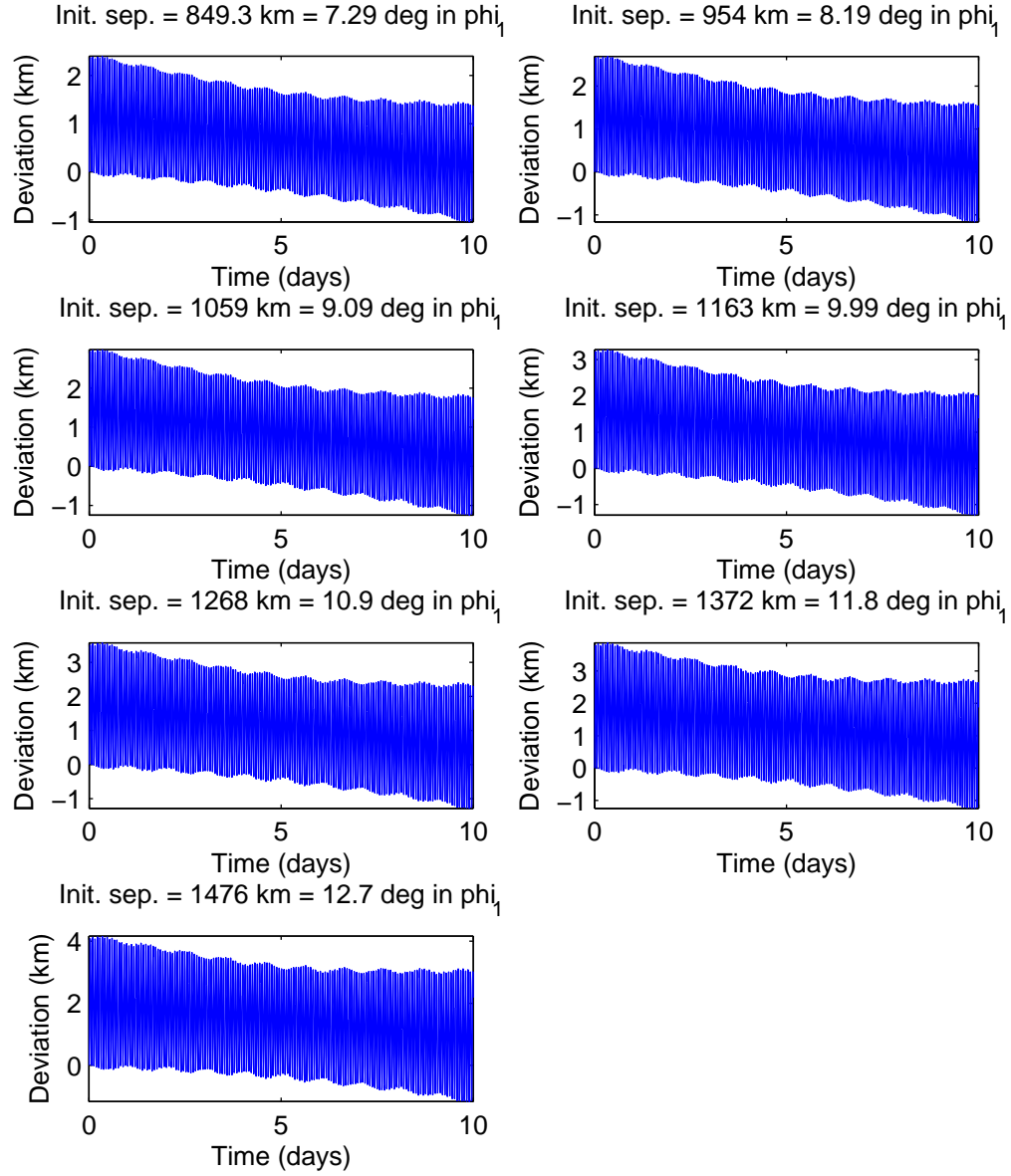
Figure A4.   Satellite separation deviation from initial value over 10 days after varying initial separations in φ_1 for 320km, $i = 15°$ orbit (contd.)
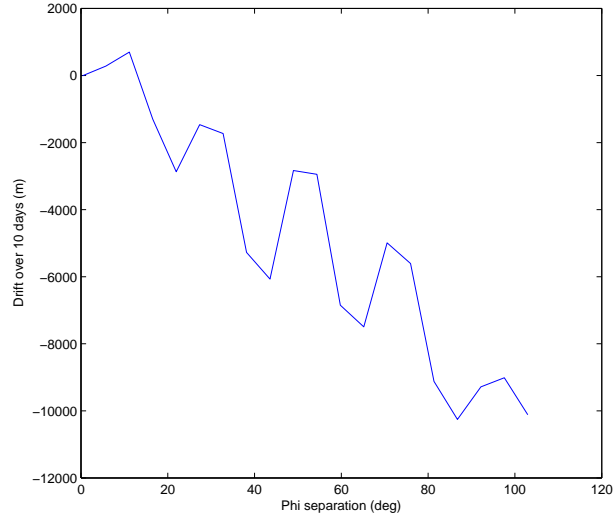
Figure A5.   Secular drift between satellites over 10 days vs. initial φ_2 separation for 320km, $i = 15°$ orbit
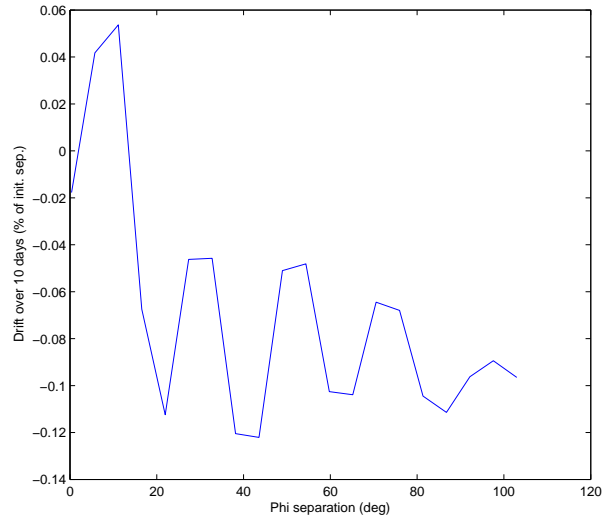

Figure A6.   Secular drift (in percentage of initial separation) between satellites over 10 days vs. initial φ_2 separation for 320km, $i = 15°$ orbit
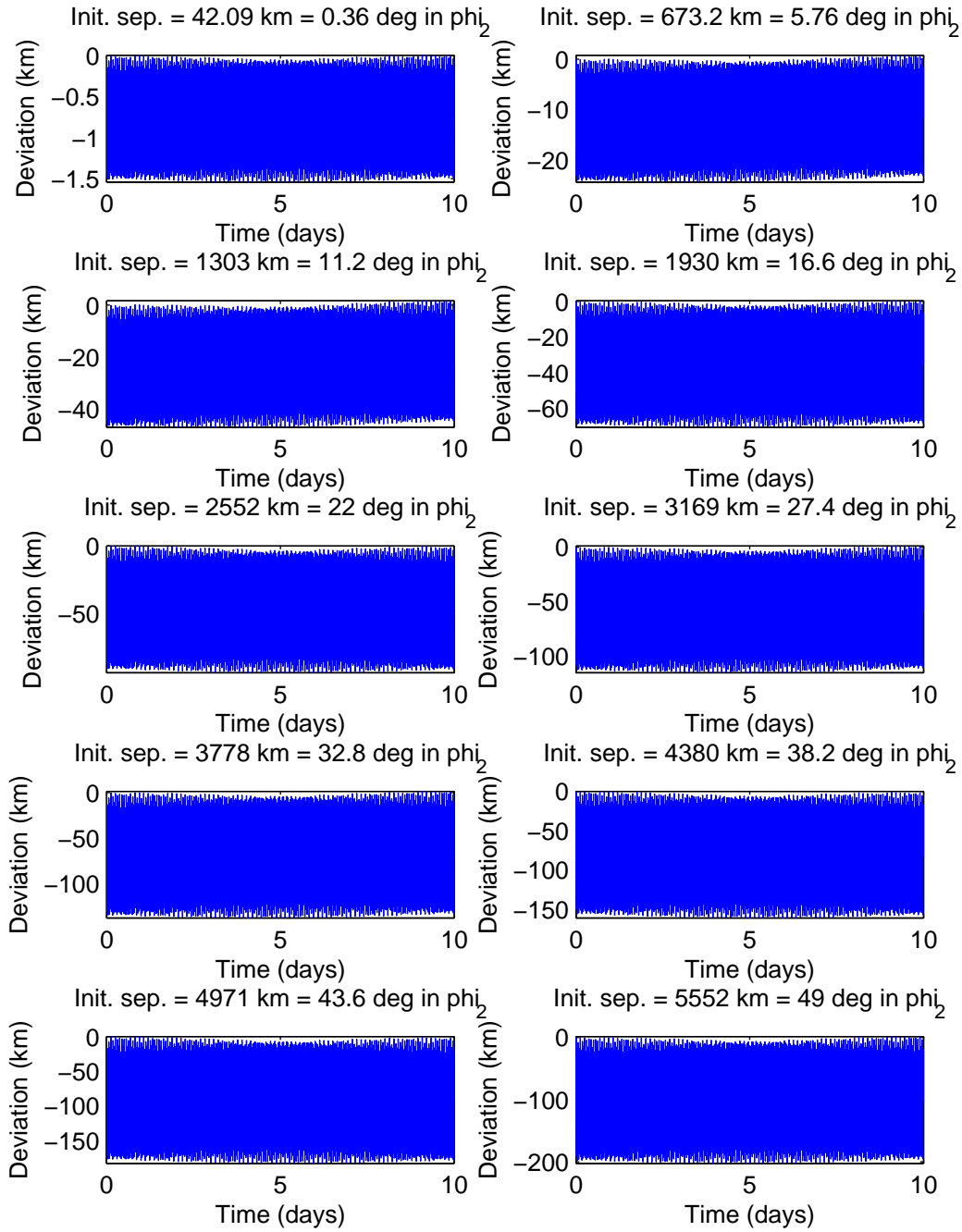
Figure A7.   Satellite separation deviation from initial value over 10 days after varying initial separations in φ_2 for 320km, $i = 15°$ orbit
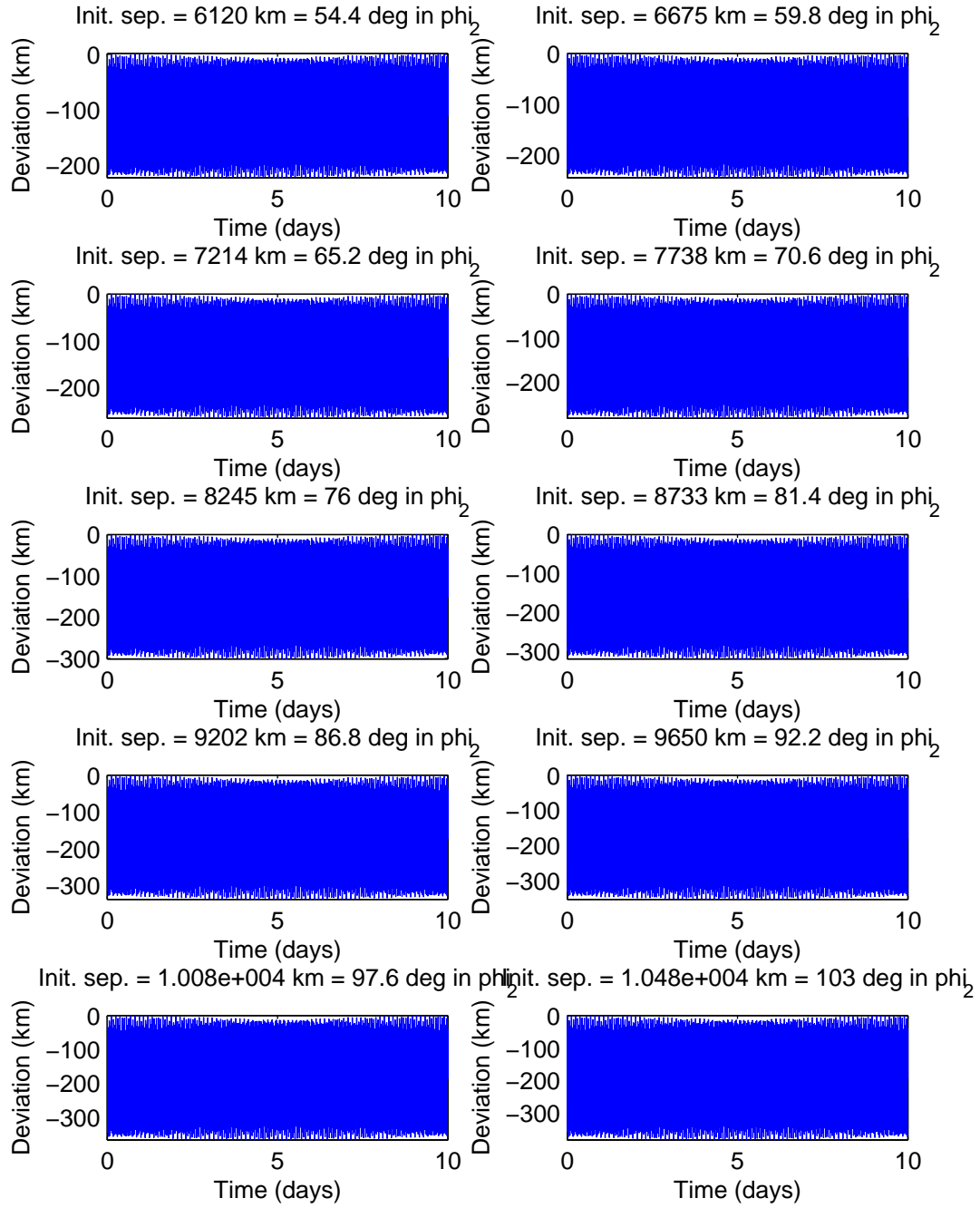
Figure A8.   Satellite separation deviation from initial value over 10 days after varying initial separations in φ_2 for 320km, $i = 15°$ orbit (contd.)

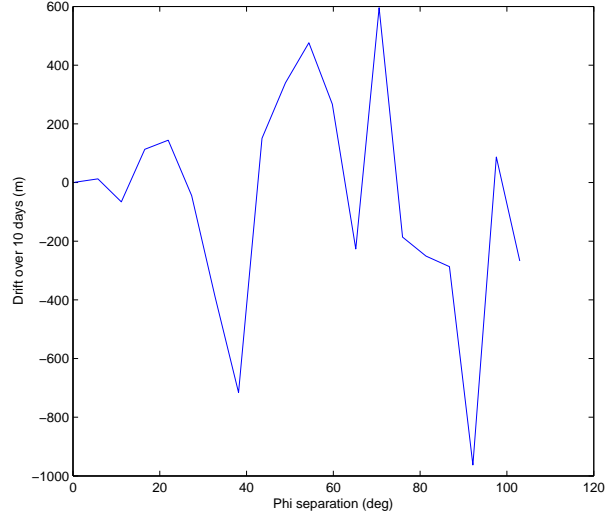Figure A9. Secular drift between satellites over 10 days vs. initial φ_3 separation for 320km, $i = 15°$ orbit
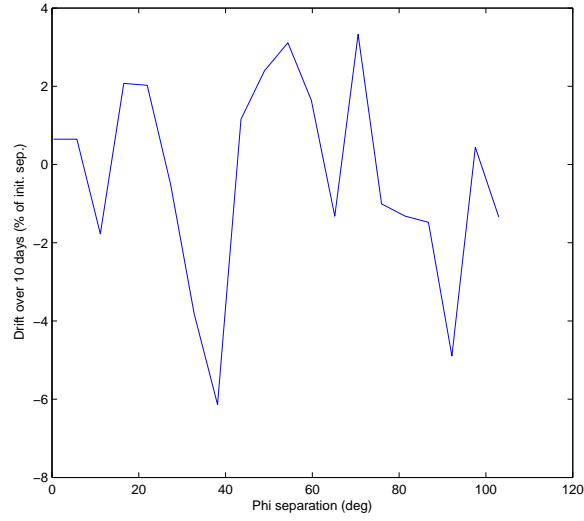

Figure A10. Secular drift (in percentage of initial separation) between satellites over 10 days vs. initial φ_3 separation for 320km, $i = 15°$ orbit
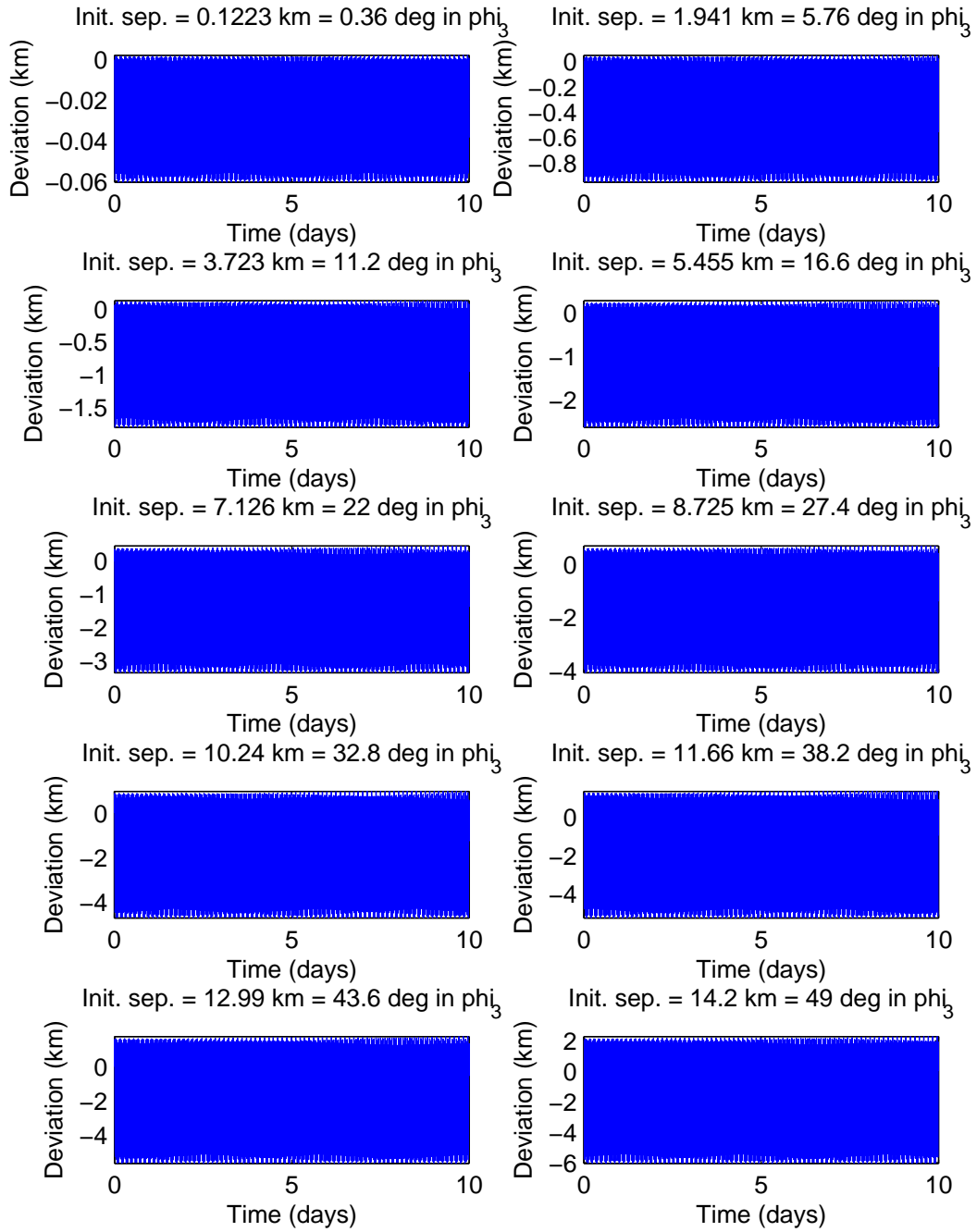
Figure A11.   Satellite separation deviation from initial value over 10 days after varying initial separations in φ_3 for 320km, $i = 15°$ orbit
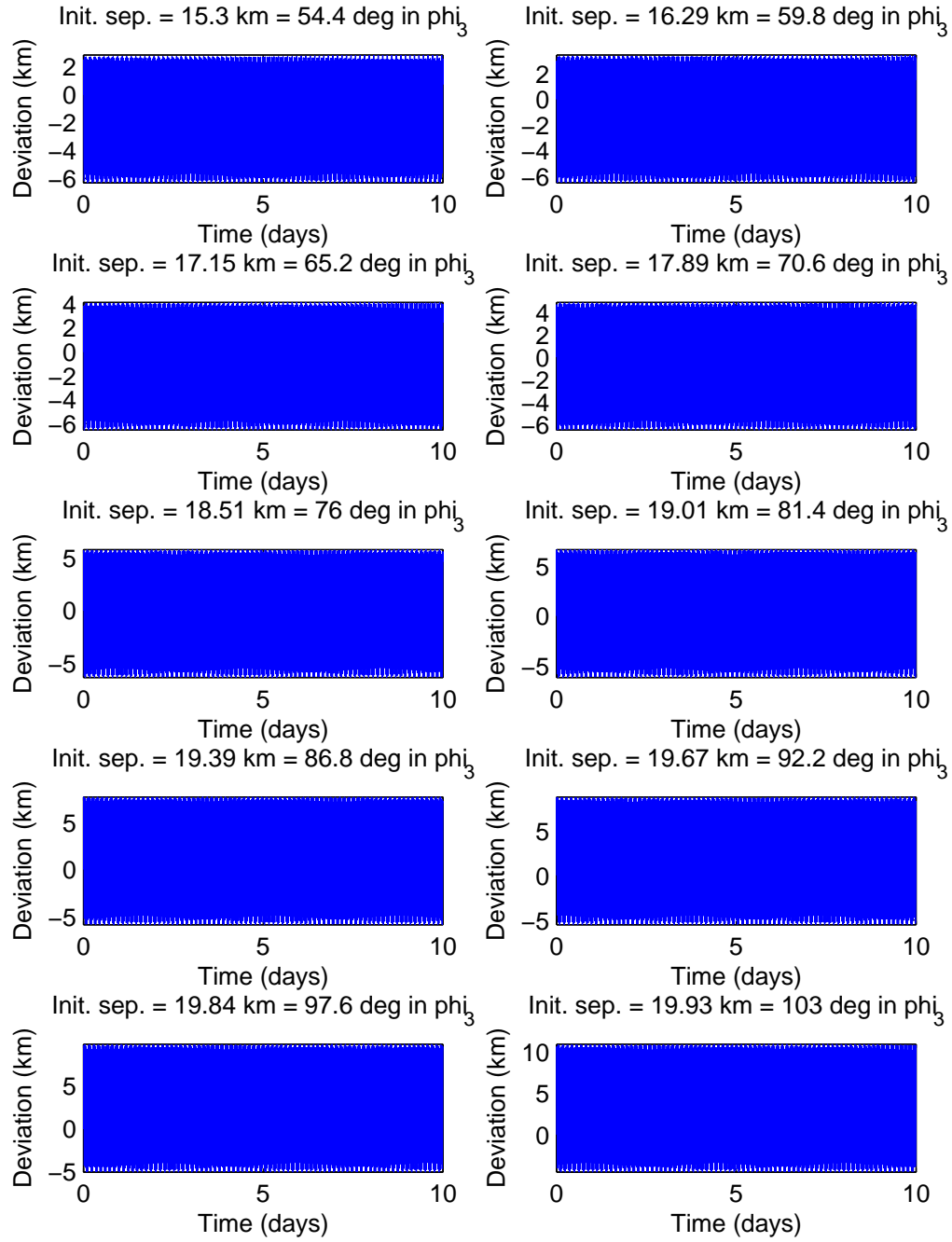
Figure A12.   Satellite separation deviation from initial value over 10 days after varying initial separations in φ_3 for 320km, $i = 15°$ orbit (contd.)
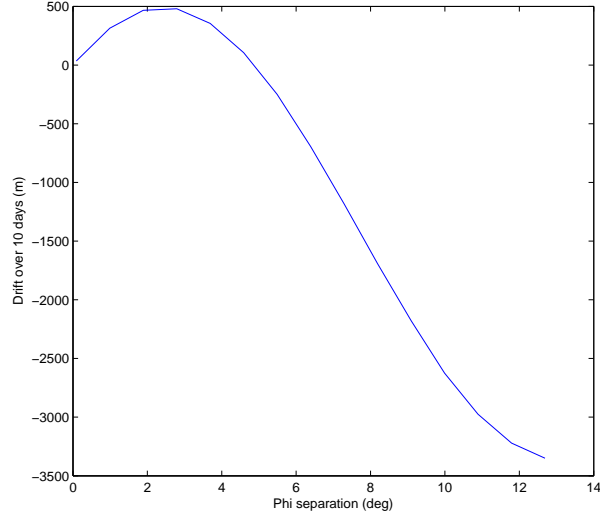
Figure B1.   Secular drift between satellites over 10 days vs. initial φ_1 separation for 320km, $i = 30°$ orbit

Table B1.   Drift results of initial displacements in φ_1 for 320km, 30° orbit over 10 days

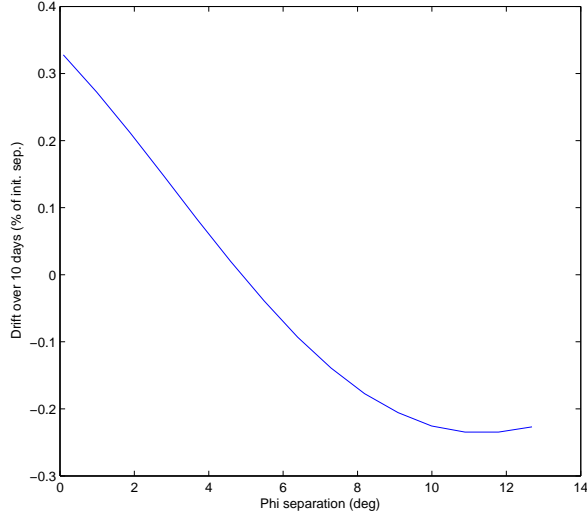| Torus angle	Initial sep. (deg)	Initial separation (m)	Oscillation amplitude (m)	Drift (m)	Drift (percent)
1	0.09	1.05e+004	19.62	34.41	0.3278
1	0.99	1.155e+005	215.8	314.3	0.2722
1	1.89	2.204e+005	412.1	466.4	0.2116
1	2.79	3.254e+005	608.4	479.6	0.1474
1	3.69	4.303e+005	804.7	354.9	0.08249
1	4.59	5.352e+005	1001	106	0.01981
1	5.49	6.4e+005	1197	-249.5	-0.03898
1	6.39	7.449e+005	1393	-694	-0.09318
1	7.29	8.496e+005	1589	-1183	-0.1393
1	8.19	9.544e+005	1785	-1692	-0.1773
1	9.09	1.059e+006	1980	-2178	-0.2056
1	9.99	1.164e+006	2175	-2624	-0.2255
1	10.89	1.268e+006	2369	-2975	-0.2346
1	11.79	1.373e+006	2563	-3221	-0.2347
1	12.69	1.477e+006	2756	-3350	-0.2268

Figure B2.   Secular drift (in percentage of initial separation) between satellites over 10
days vs. initial φ_1 separation for 320km, $i = 30°$ orbit

Table B2.   Drift results of initial displacements in φ_2 for 320km, 30° orbit over 10 days

Torus angle	Initial sep. (deg)	Initial separation (m)	Oscillation amplitude (m)	Drift (m)	Drift (percent)
2	0.36	4.209e+004	5416	221.6	0.5265
2	5.76	6.731e+005	8.656e+004	4463	0.6631
2	11.16	1.303e+006	1.675e+005	8481	0.6511
2	16.56	1.929e+006	2.483e+005	1.004e+004	0.5206
2	21.96	2.552e+006	3.285e+005	1.132e+004	0.4435
2	27.36	3.168e+006	4.079e+005	1.391e+004	0.439
2	32.76	3.778e+006	4.865e+005	1.532e+004	0.4055
2	38.16	4.379e+006	5.641e+005	1.593e+004	0.3637
2	43.56	4.971e+006	6.402e+005	1.936e+004	0.3896
2	48.96	5.551e+006	7.148e+005	2.418e+004	0.4356
2	54.36	6.12e+006	7.88e+005	2.66e+004	0.4347
2	59.76	6.674e+006	8.594e+005	2.829e+004	0.4238
2	65.16	7.214e+006	9.289e+005	3.129e+004	0.4338
2	70.56	7.738e+006	9.964e+005	3.278e+004	0.4236
2	75.96	8.244e+006	1.062e+006	3.179e+004	0.3856
2	81.36	8.732e+006	1.125e+006	3.234e+004	0.3703
2	86.76	9.201e+006	1.185e+006	3.606e+004	0.3919
2	92.16	9.65e+006	1.243e+006	3.977e+004	0.4122
2	97.56	1.008e+007	1.298e+006	4.122e+004	0.4091
2	103	1.048e+007	1.35e+006	4.142e+004	0.3951

84

Table B3.   Drift results of initial displacements in φ_3 for 320km, 30° orbit over 10 days

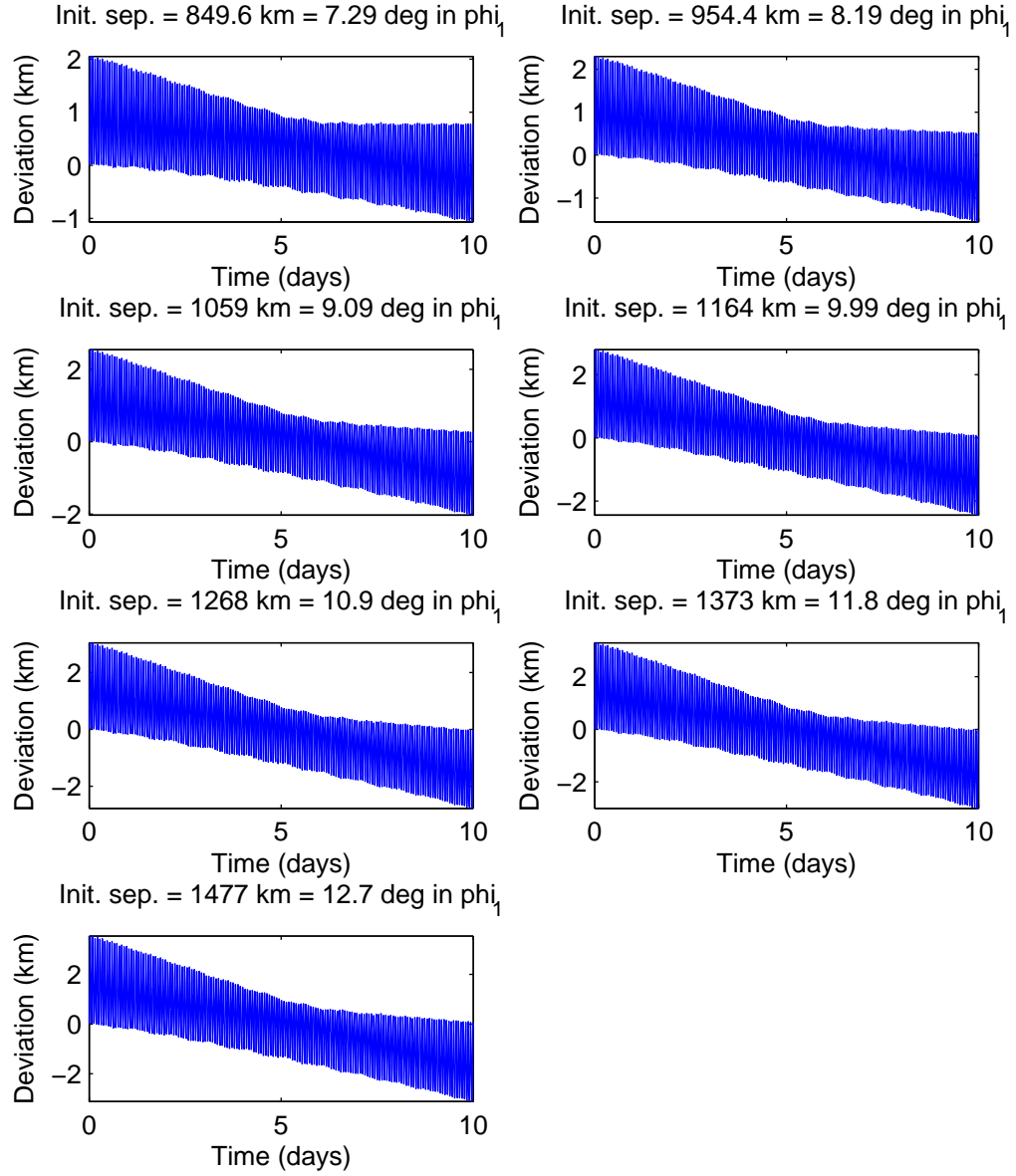| Torus angle	Initial sep. (deg)	Initial separation (m)	Oscillation amplitude (m)	Drift (m)	Drift (percent)
3	0.36	105.6	54.32	-0.7253	-0.6869
3	5.76	1662	868.6	-39.27	-2.363
3	11.16	3159	1681	-151.9	-4.807
3	16.56	4589	2490	40.08	0.8733
3	21.96	5942	3292	-14.83	-0.2496
3	27.36	7211	4088	253.3	3.513
3	32.76	8389	4875	163.7	1.952
3	38.16	9471	5652	-89.62	-0.9463
3	43.56	1.045e+004	6415	298.1	2.852
3	48.96	1.133e+004	7164	-141.6	-1.249
3	54.36	1.211e+004	7898	-51.77	-0.4274
3	59.76	1.279e+004	8613	-410.4	-3.209
3	65.16	1.337e+004	9311	-566	-4.235
3	70.56	1.385e+004	9985	209.5	1.513
3	75.96	1.425e+004	1.064e+004	36.09	0.2533
3	81.36	1.457e+004	1.127e+004	850.5	5.839
3	86.76	1.482e+004	1.187e+004	316.6	2.137
3	92.16	1.502e+004	1.246e+004	28.76	0.1915
3	97.56	1.518e+004	1.301e+004	347.9	2.293
3	103	1.531e+004	1.353e+004	-657.1	-4.291
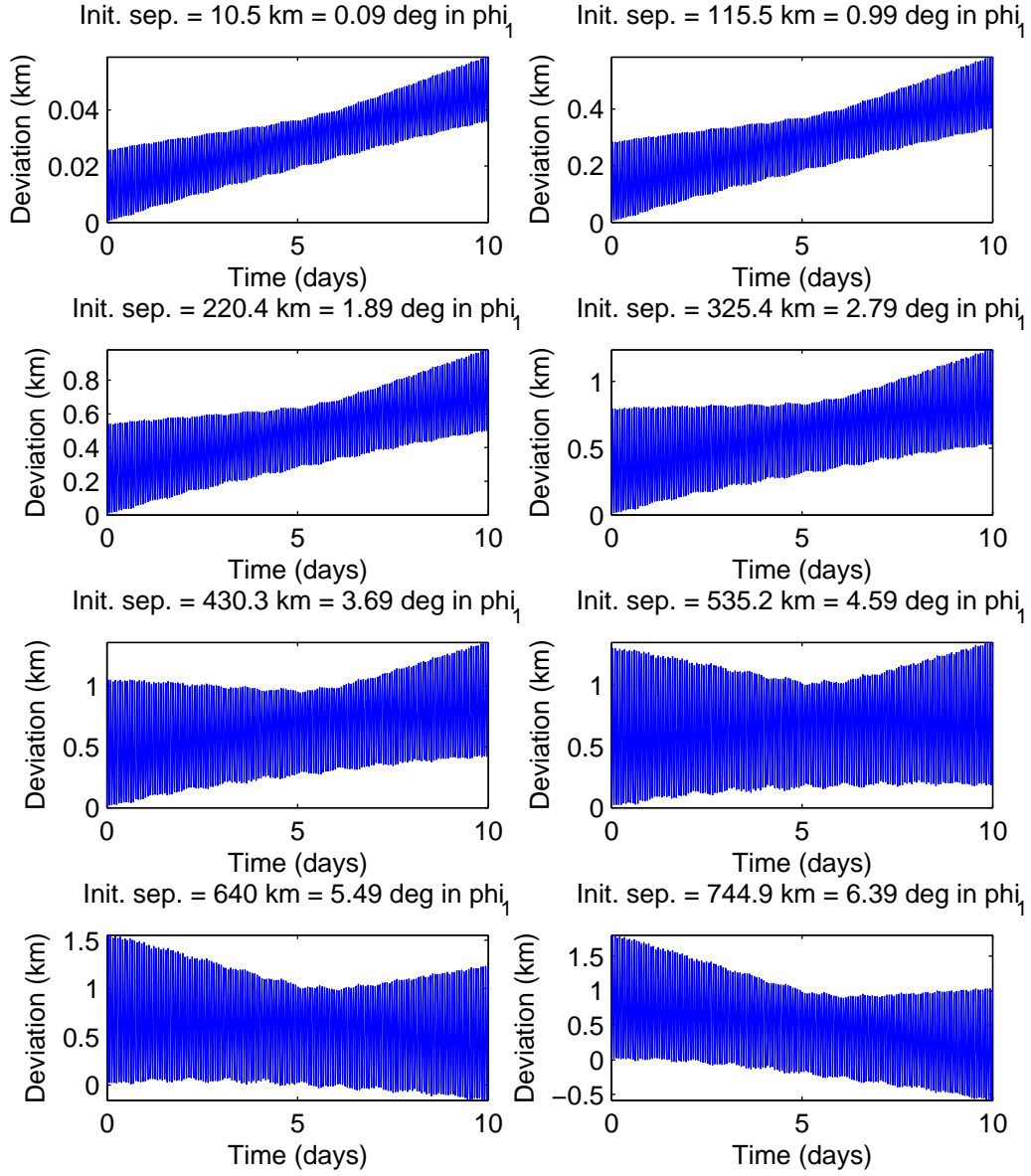
Figure B3.   Satellite separation deviation from initial value over 10 days after varying initial separations in φ_1 for 320km, $i = 30°$ orbit

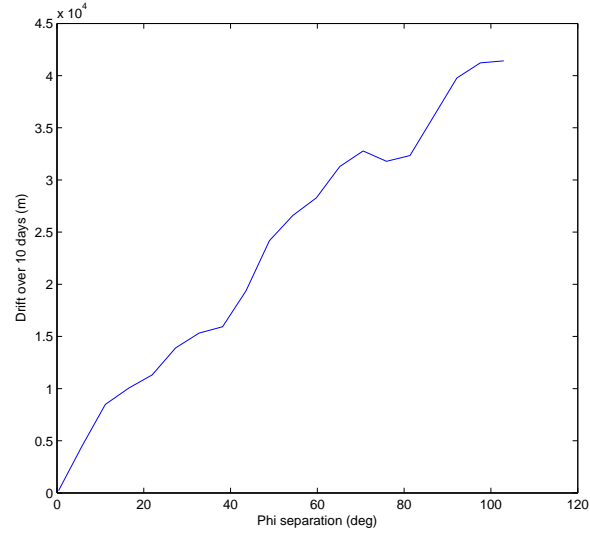Init. sep. = 849.6 km = 7.29 deg in phi$_1$

Init. sep. = 954.4 km = 8.19 deg in phi$_1$

Init. sep. = 1059 km = 9.09 deg in phi$_1$

Init. sep. = 1164 km = 9.99 deg in phi$_1$

Init. sep. = 1268 km = 10.9 deg in phi$_1$

Init. sep. = 1373 km = 11.8 deg in phi$_1$
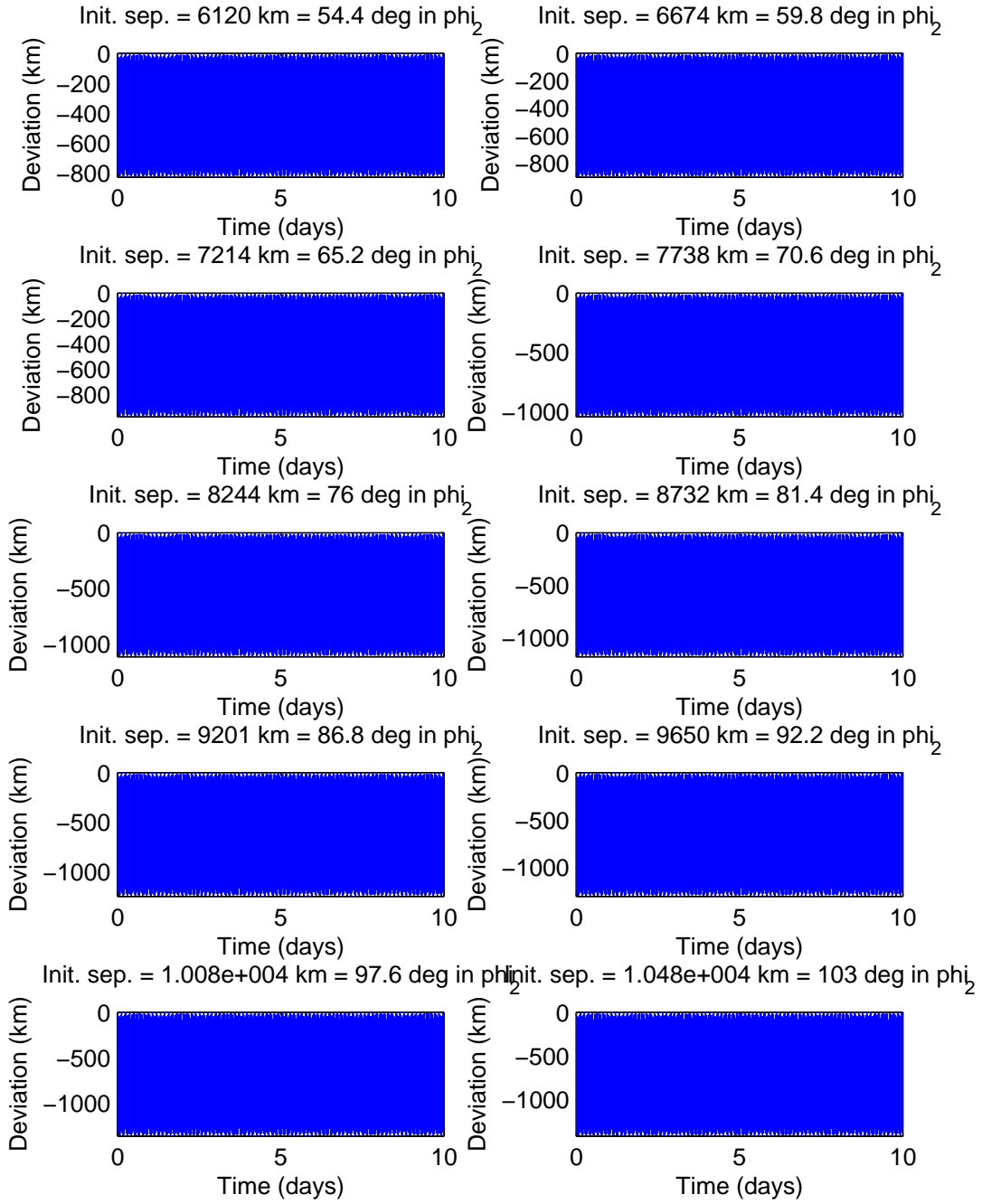
Init. sep. = 1477 km = 12.7 deg in phi$_1$

Figure B4.   Satellite separation deviation from initial value over 10 days after varying initial separations in φ_1 for 320km, $i = 30°$ orbit (contd.)
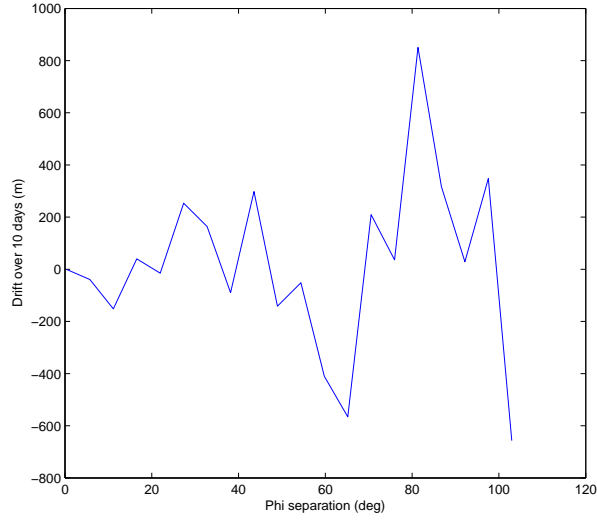
Figure B5.   Secular drift between satellites over 10 days vs. initial φ_2 separation for 320km, $i = 30°$ orbit
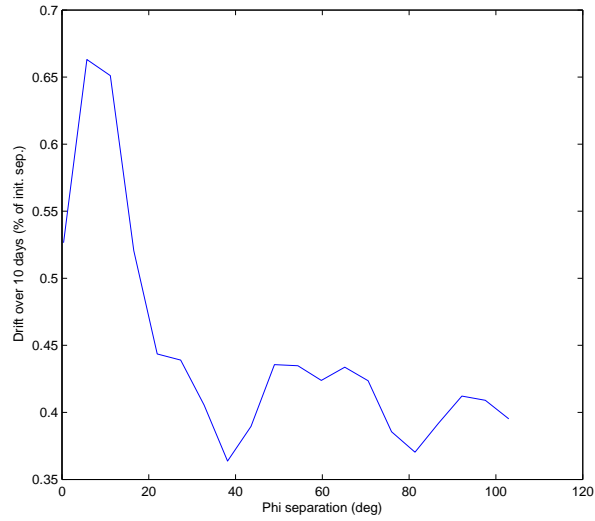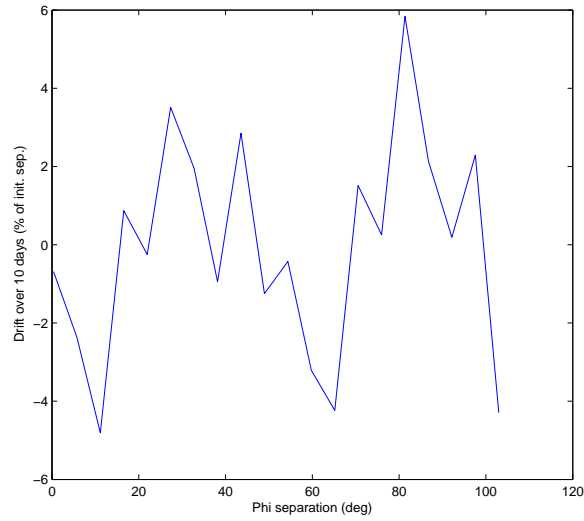

Figure B6.   Secular drift (in percentage of initial separation) between satellites over 10 days vs. initial φ_2 separation for 320km, $i = 30°$ orbit

88
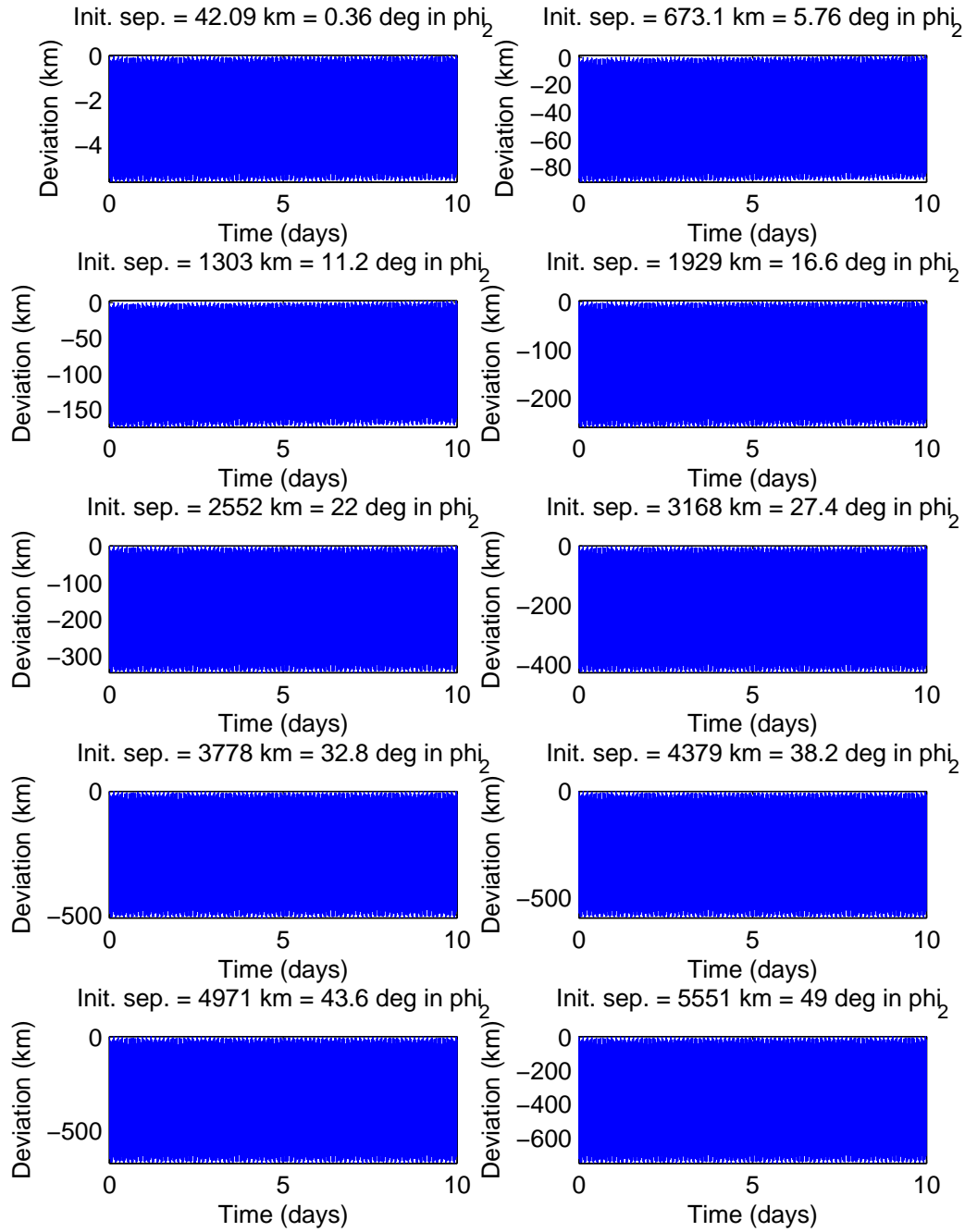
Figure B7.   Satellite separation deviation from initial value over 10 days after varying initial separations in φ_2 for 320km, $i = 30°$ orbit

Figure B8.   Satellite separation deviation from initial value over 10 days after varying initial separations in φ_2 for 320km, $i = 30°$ orbit (contd.)

90

Figure B9.   Secular drift between satellites over 10 days vs. initial φ_3 separation for 320km, $i = 30°$ orbit

Figure B10.   Secular drift (in percentage of initial separation) between satellites over 10 days vs. initial φ_3 separation for 320km, $i = 30°$ orbit
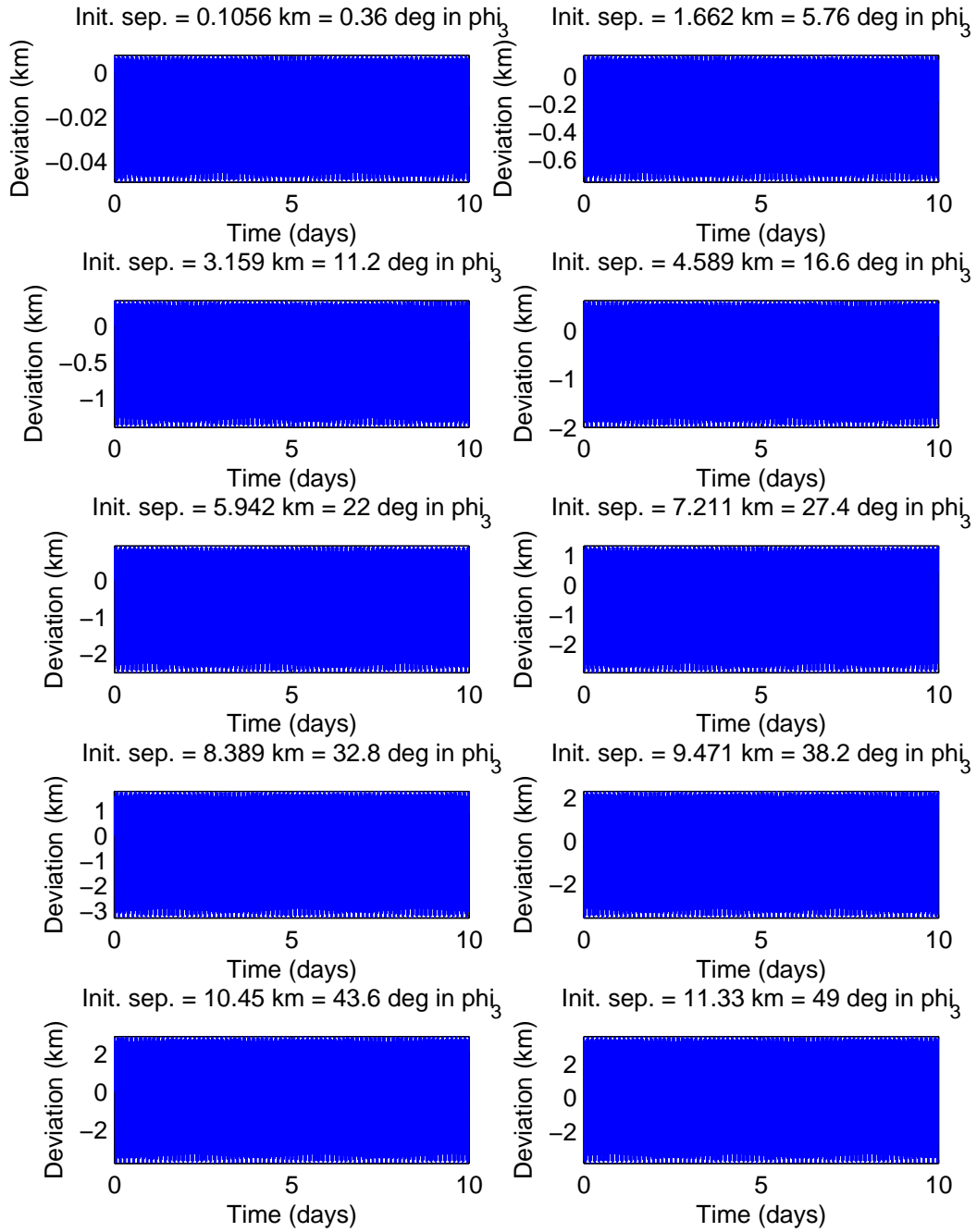
Figure B11.   Satellite separation deviation from initial value over 10 days after varying initial separations in φ_3 for 320km, $i = 30°$ orbit
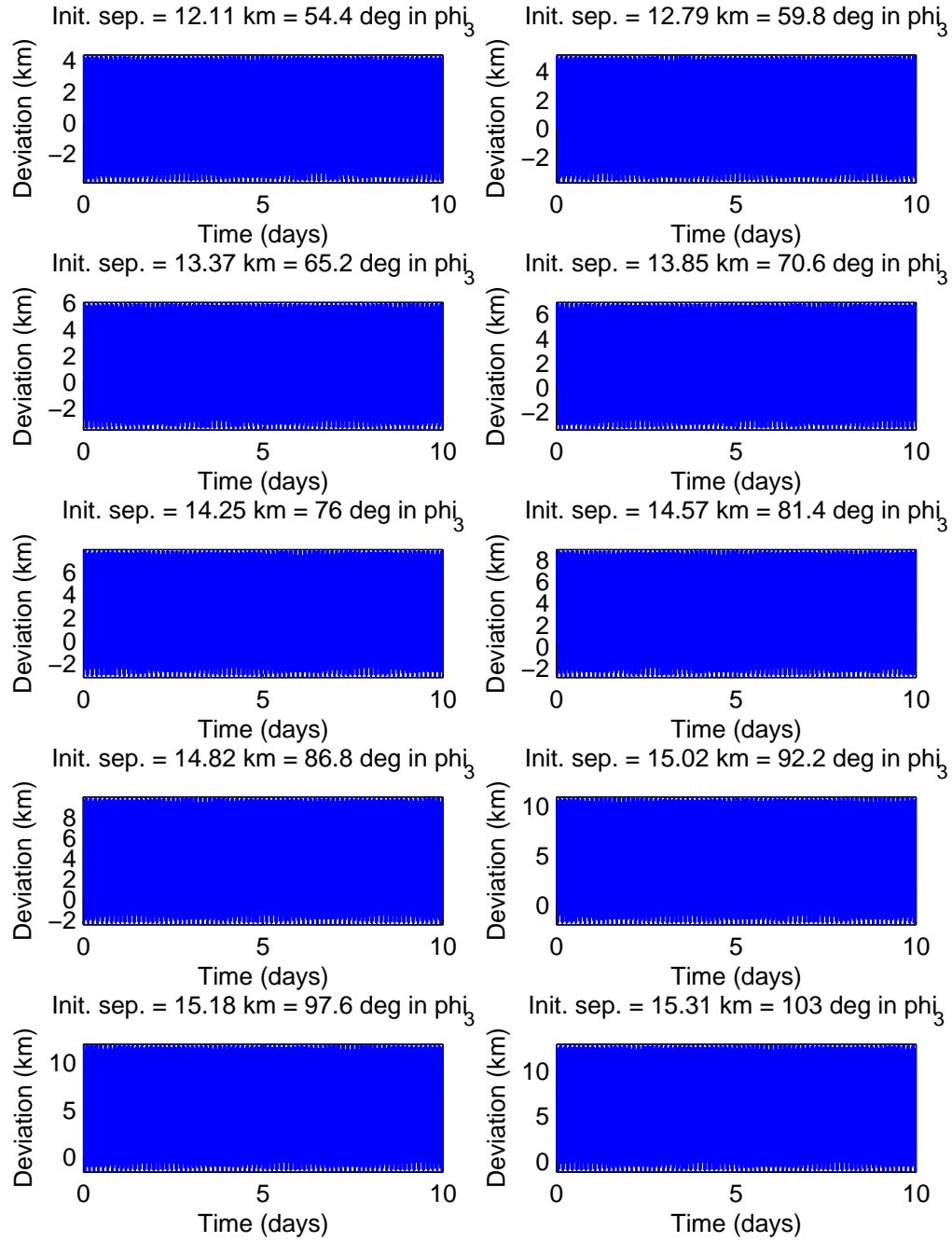
Figure B12.   Satellite separation deviation from initial value over 10 days after varying initial separations in φ_3 for 320km, $i = 30°$ orbit (contd.)

Appendix C. Formation drift survey results, 630km, $i = 15°$
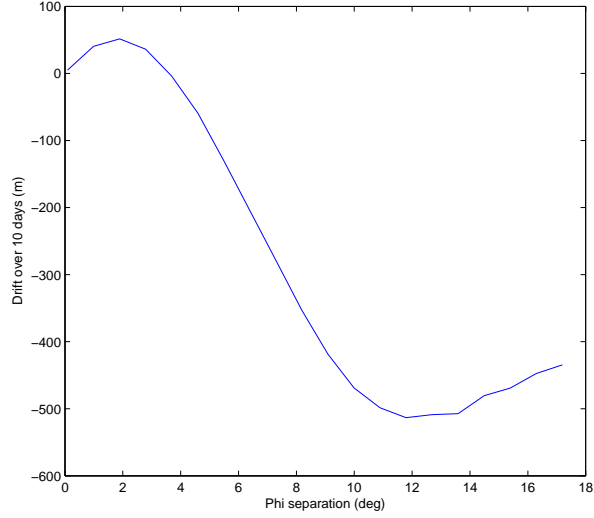

Figure C1.   Secular drift between satellites over 10 days vs. initial φ_1 separation for 630km, $i = 15°$ orbit

Table C1.   Drift results of initial displacements in φ_1 for 630km, $15°$ orbit over 10 days

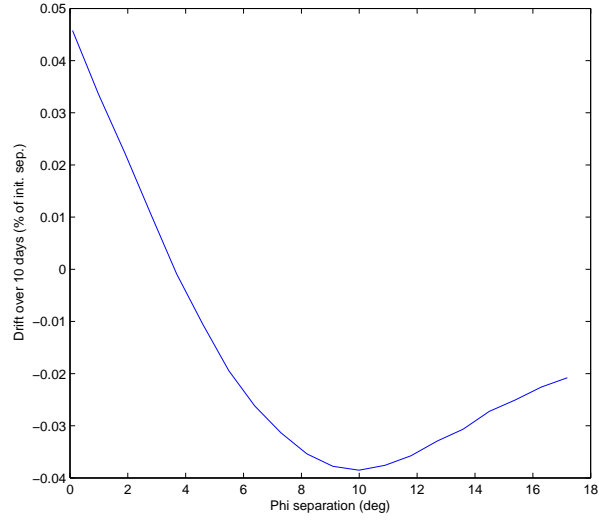| Torus angle	Initial sep. (deg)	Initial separation (m)	Oscillation amplitude (m)	Drift (m)	Drift (percent)
1	0.09	1.098e+004	25.34	5.025	0.04577
1	0.99	1.208e+005	278.8	40.52	0.03354
1	1.89	2.306e+005	532.2	51.61	0.02238
1	2.79	3.404e+005	785.5	36.21	0.01064
1	3.69	4.501e+005	1039	-4.039	-0.0008974
1	4.59	5.599e+005	1292	-58.9	-0.01052
1	5.49	6.695e+005	1544	-130.1	-0.01943
1	6.39	7.792e+005	1797	-204.2	-0.02621
1	7.29	8.888e+005	2049	-278.7	-0.03135
1	8.19	9.984e+005	2300	-353.2	-0.03538
1	9.09	1.108e+006	2551	-418.5	-0.03778
1	9.99	1.217e+006	2801	-468.8	-0.03851
1	10.89	1.327e+006	3051	-498.5	-0.03757
1	11.79	1.436e+006	3300	-513.2	-0.03574
1	12.69	1.545e+006	3548	-508.8	-0.03293

94

Figure C2.   Secular drift (in percentage of initial separation) between satellites over 10
days vs. initial φ_1 separation for 630km, $i = 15°$ orbit

Table C2.   Drift results of initial displacements in φ_2 for 630km, 15° orbit over 10 days

Torus angle	Initial sep. (deg)	Initial separation (m)	Oscillation amplitude (m)	Drift (m)	Drift (percent)
2	0.36	4.404e+004	1449	104.6	0.2376
2	5.76	7.043e+005	2.317e+004	2052	0.2914
2	11.16	1.363e+006	4.485e+004	3744	0.2746
2	16.56	2.019e+006	6.644e+004	4209	0.2085
2	21.96	2.67e+006	8.788e+004	5043	0.1889
2	27.36	3.315e+006	1.091e+005	7678	0.2316
2	32.76	3.953e+006	1.301e+005	9873	0.2498
2	38.16	4.582e+006	1.508e+005	1.005e+004	0.2194
2	43.56	5.201e+006	1.712e+005	1.085e+004	0.2087
2	48.96	5.809e+006	1.912e+005	1.305e+004	0.2246
2	54.36	6.403e+006	2.107e+005	1.477e+004	0.2307
2	59.76	6.983e+006	2.298e+005	1.567e+004	0.2244
2	65.16	7.548e+006	2.484e+005	1.682e+004	0.2228
2	70.56	8.096e+006	2.665e+005	1.826e+004	0.2256
2	75.96	8.626e+006	2.839e+005	1.89e+004	0.2191
2	81.36	9.137e+006	3.007e+005	1.957e+004	0.2142
2	86.76	9.628e+006	3.169e+005	2.126e+004	0.2209
2	92.16	1.01e+007	3.323e+005	2.254e+004	0.2233
2	97.56	1.054e+007	3.47e+005	2.277e+004	0.2159
2	103	1.097e+007	3.61e+005	2.304e+004	0.2101

Table C3.   Drift results of initial displacements in φ_3 for 630km, 15° orbit over 10 days

Torus angle	Initial sep. (deg)	Initial separation (m)	Oscillation amplitude (m)	Drift (m)	Drift (percent)
3	0.36	116.8	57.24	-2.388	-2.046
3	5.76	1853	915.4	2.153	0.1162
3	11.16	3552	1771	138.9	3.91
3	16.56	5203	2623	130.2	2.503
3	21.96	6794	3468	-2.579	-0.03796
3	27.36	8315	4308	-106.8	-1.284
3	32.76	9755	5138	-134.5	-1.379
3	38.16	1.111e+004	5955	394	3.547
3	43.56	1.236e+004	6758	401.5	3.248
3	48.96	1.351e+004	7547	146.1	1.081
3	54.36	1.455e+004	8321	-183.6	-1.262
3	59.76	1.548e+004	9076	-222.1	-1.434
3	65.16	1.63e+004	9809	516.8	3.172
3	70.56	1.699e+004	1.052e+004	553.3	3.256
3	75.96	1.757e+004	1.121e+004	513.6	2.922
3	81.36	1.804e+004	1.187e+004	-726.9	-4.029
3	86.76	1.84e+004	1.251e+004	-571.2	-3.104
3	92.16	1.866e+004	1.312e+004	119.3	0.6394
3	97.56	1.882e+004	1.37e+004	388.4	2.064
3	103	1.89e+004	1.425e+004	180.8	0.9568
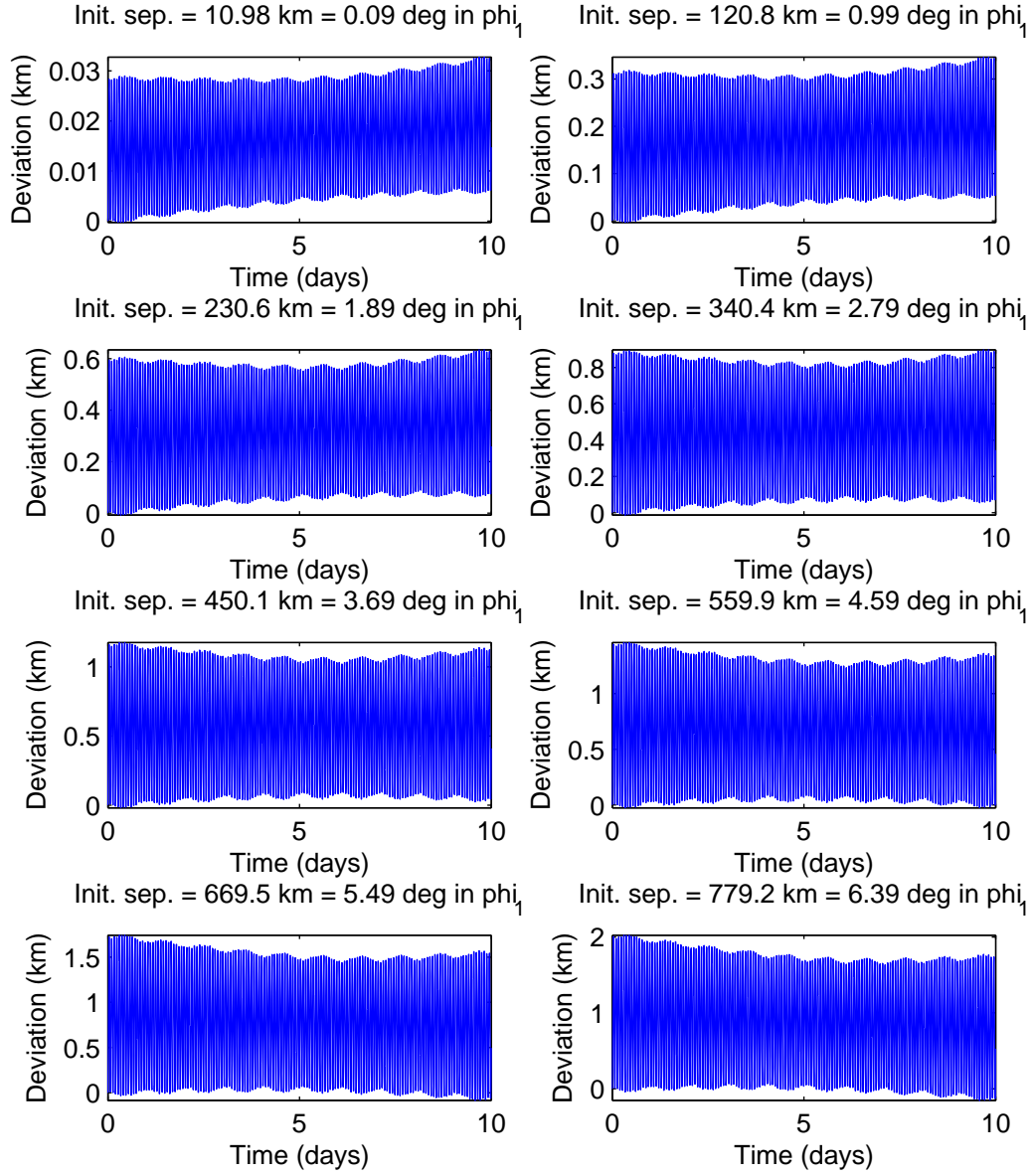
Figure C3.   Satellite separation deviation from initial value over 10 days after varying initial separations in φ_1 for 630km, $i = 15°$ orbit
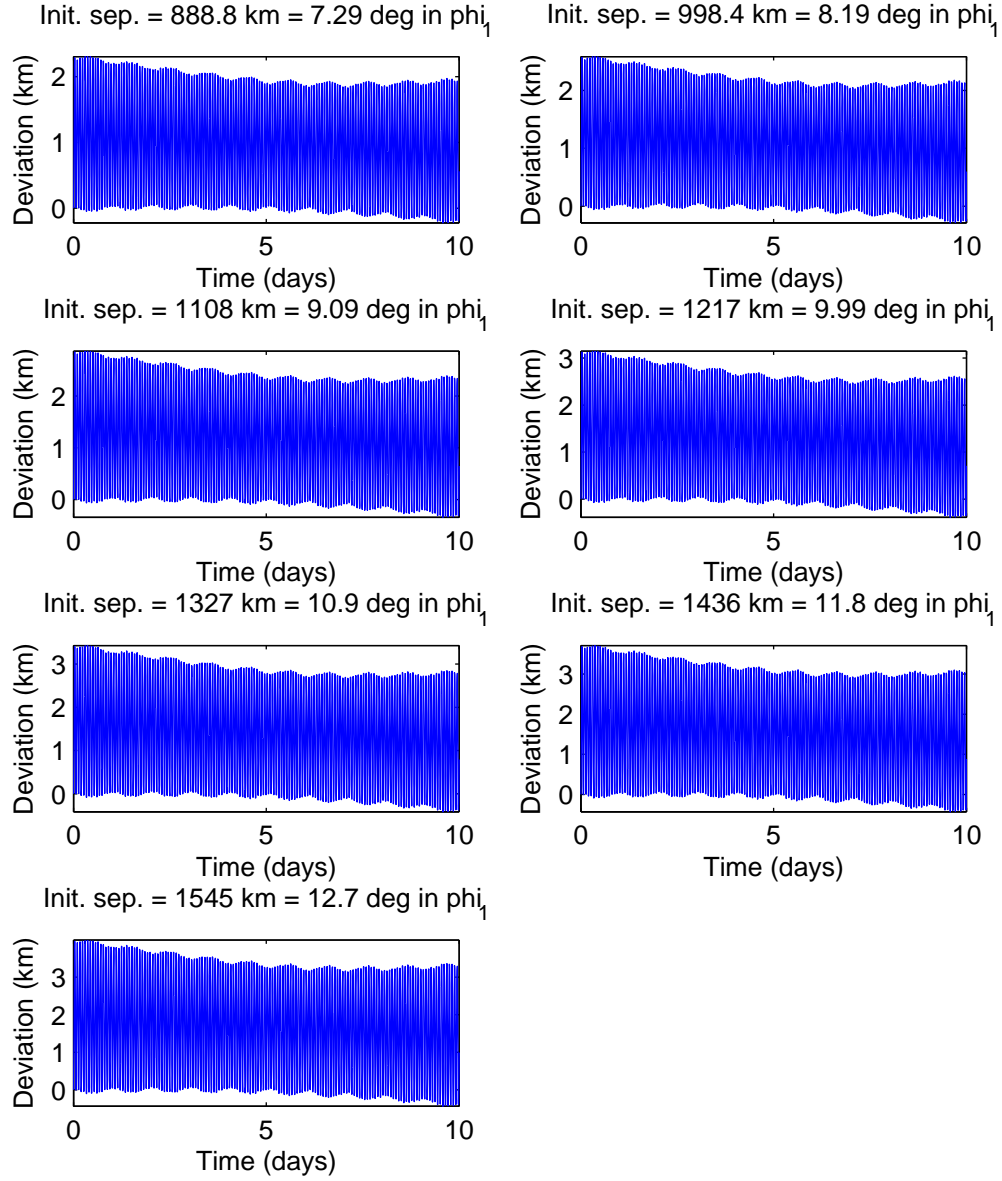
Figure C4. Satellite separation deviation from initial value over 10 days after varying initial separations in φ_1 for 630km, $i = 15°$ orbit (contd.)

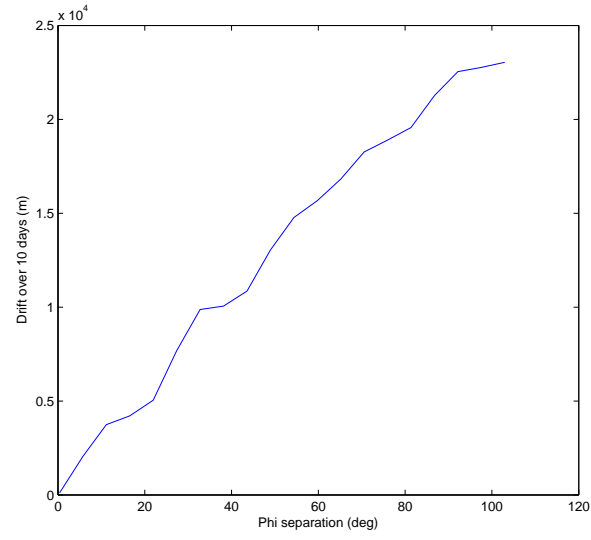Figure C5.   Secular drift between satellites over 10 days vs. initial φ_2 separation for 630km, $i = 15°$ orbit
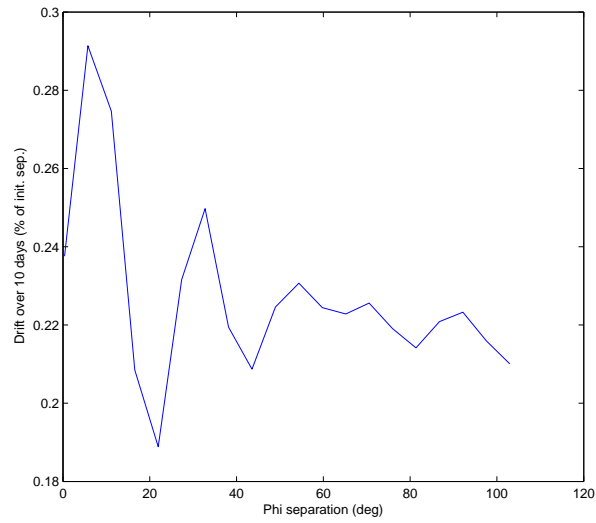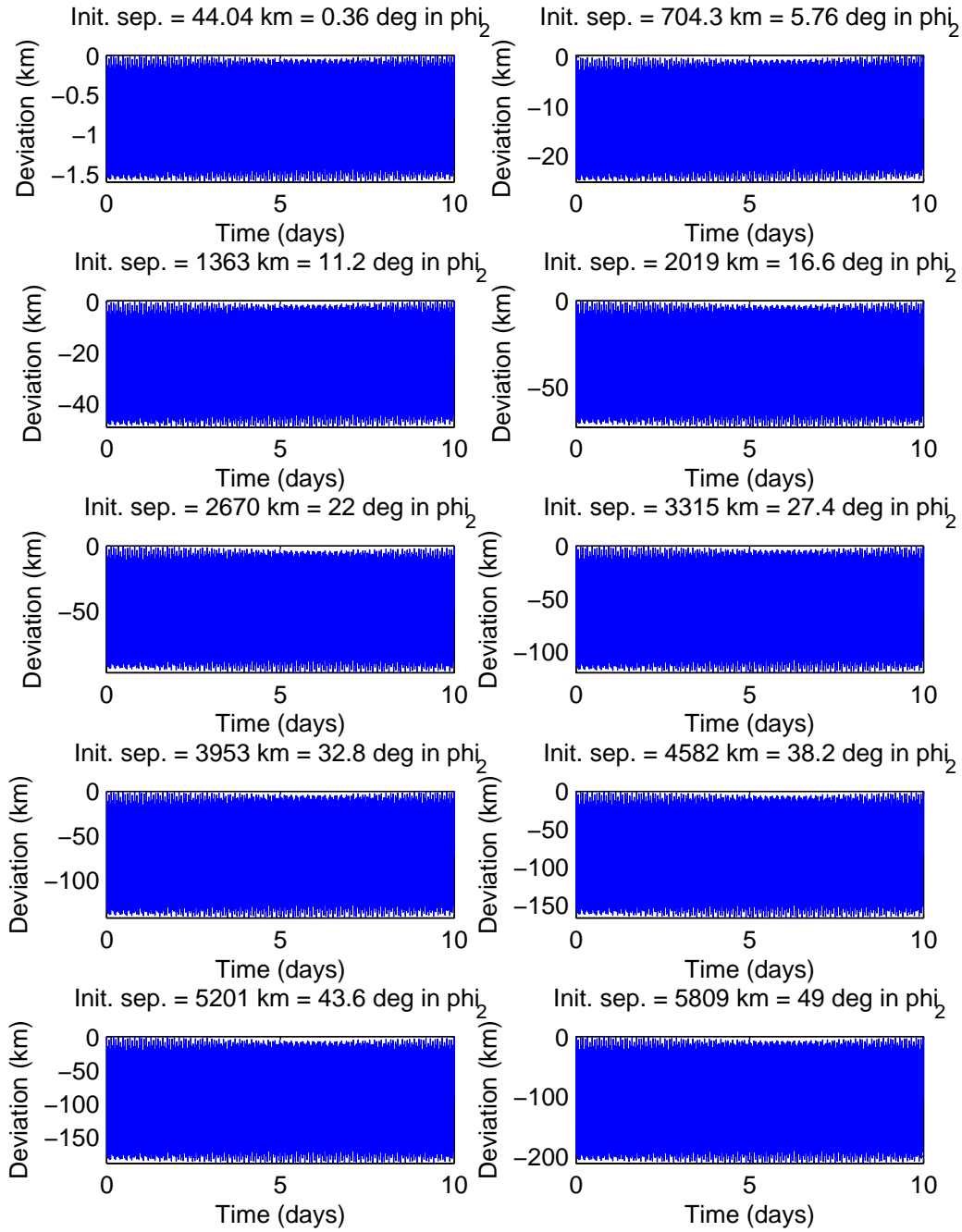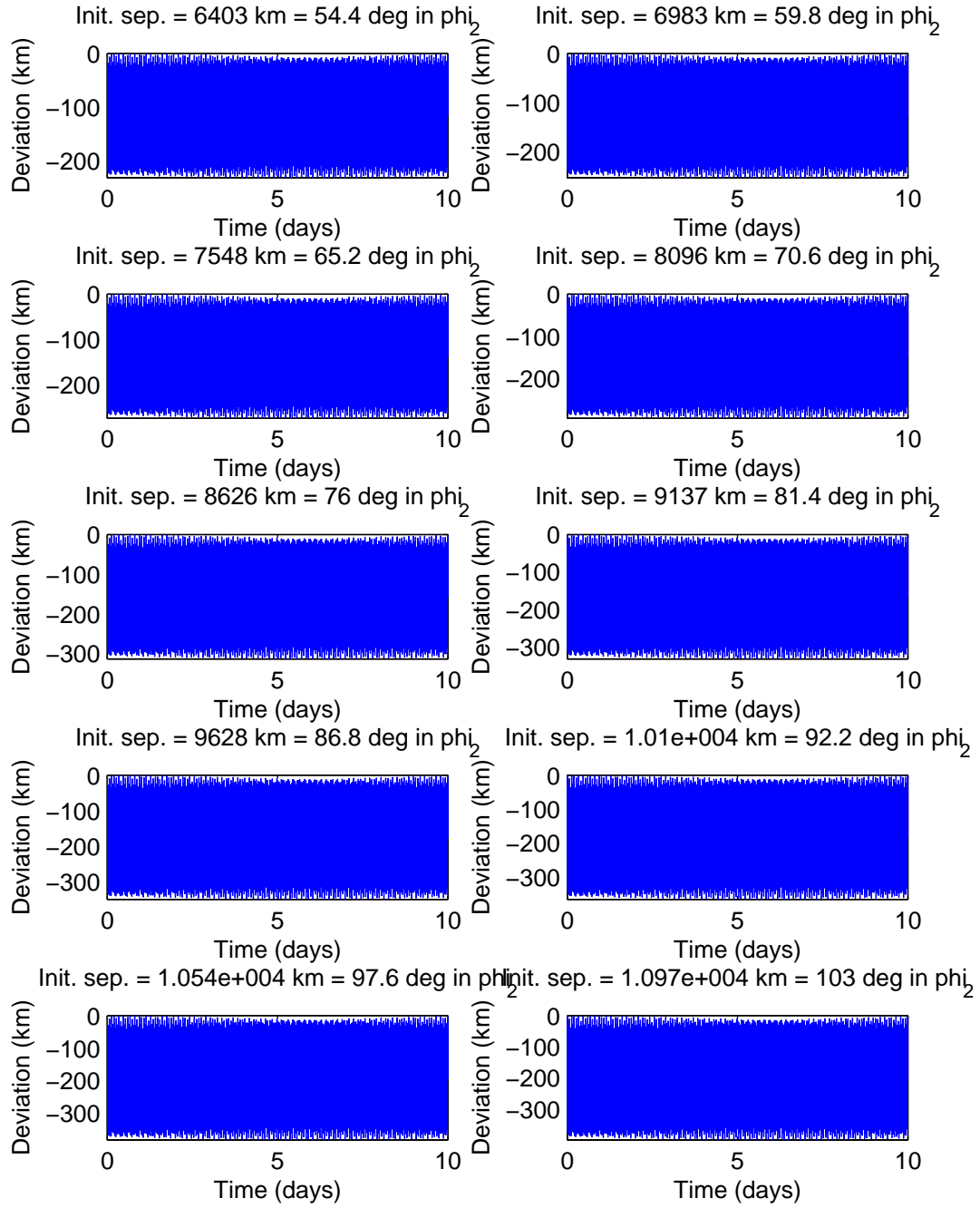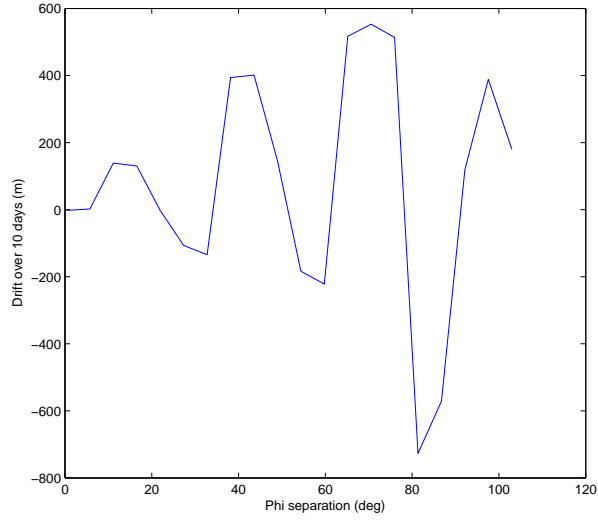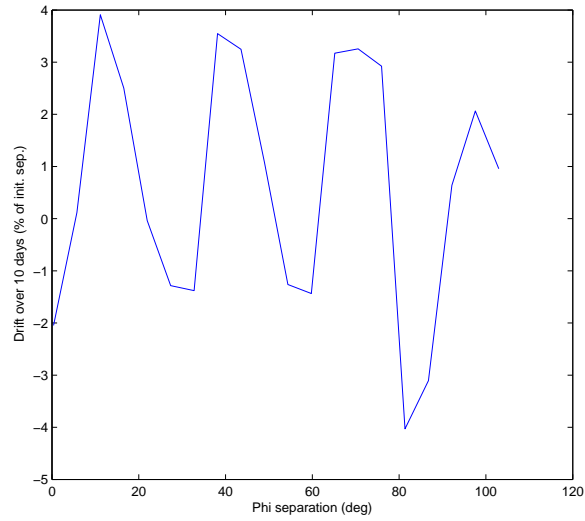

Figure C6.   Secular drift (in percentage of initial separation) between satellites over 10 days vs. initial φ_2 separation for 630km, $i = 15°$ orbit

99

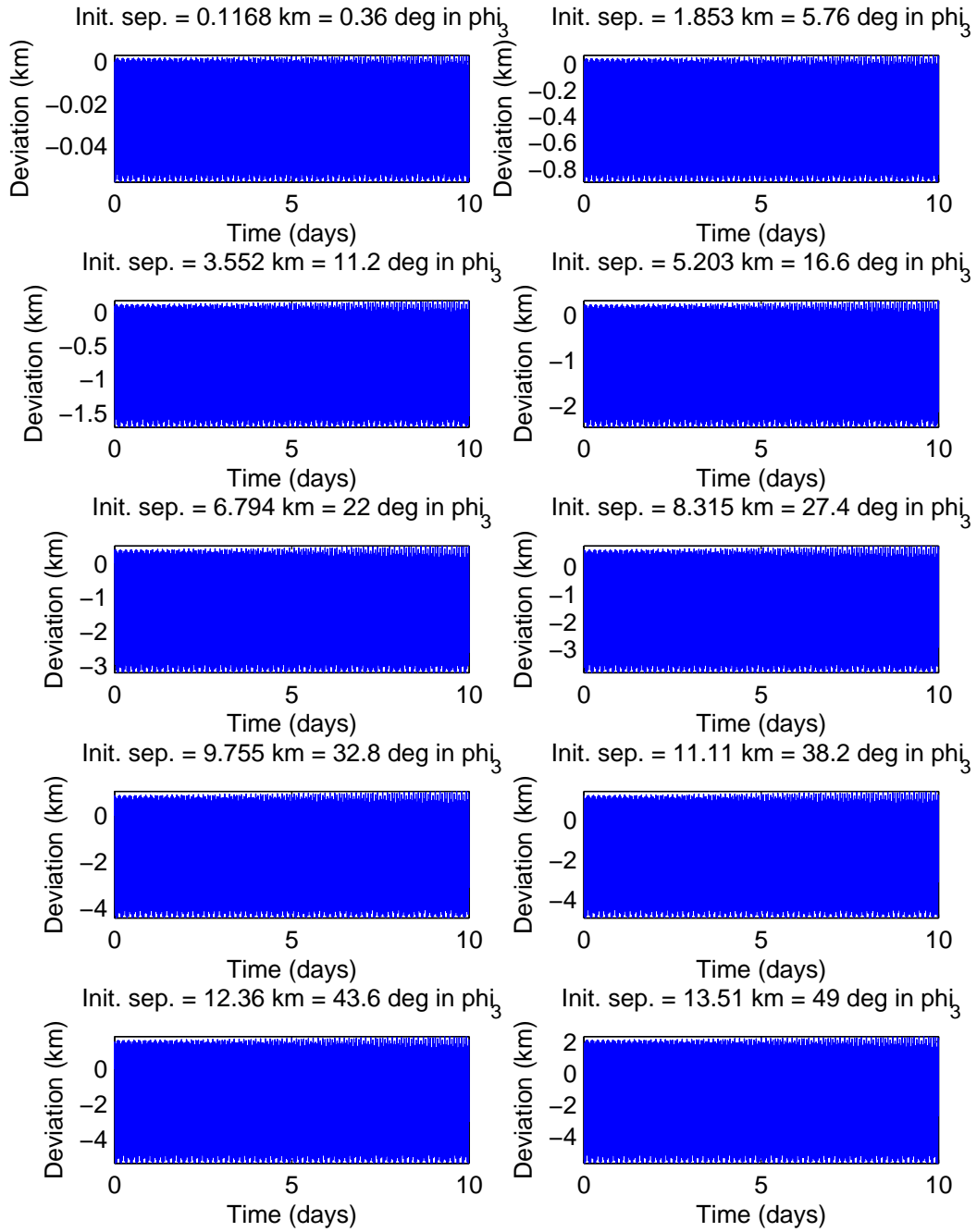Figure C7. Satellite separation deviation from initial value over 10 days after varying initial separations in φ_2 for 630km, $i = 15°$ orbit
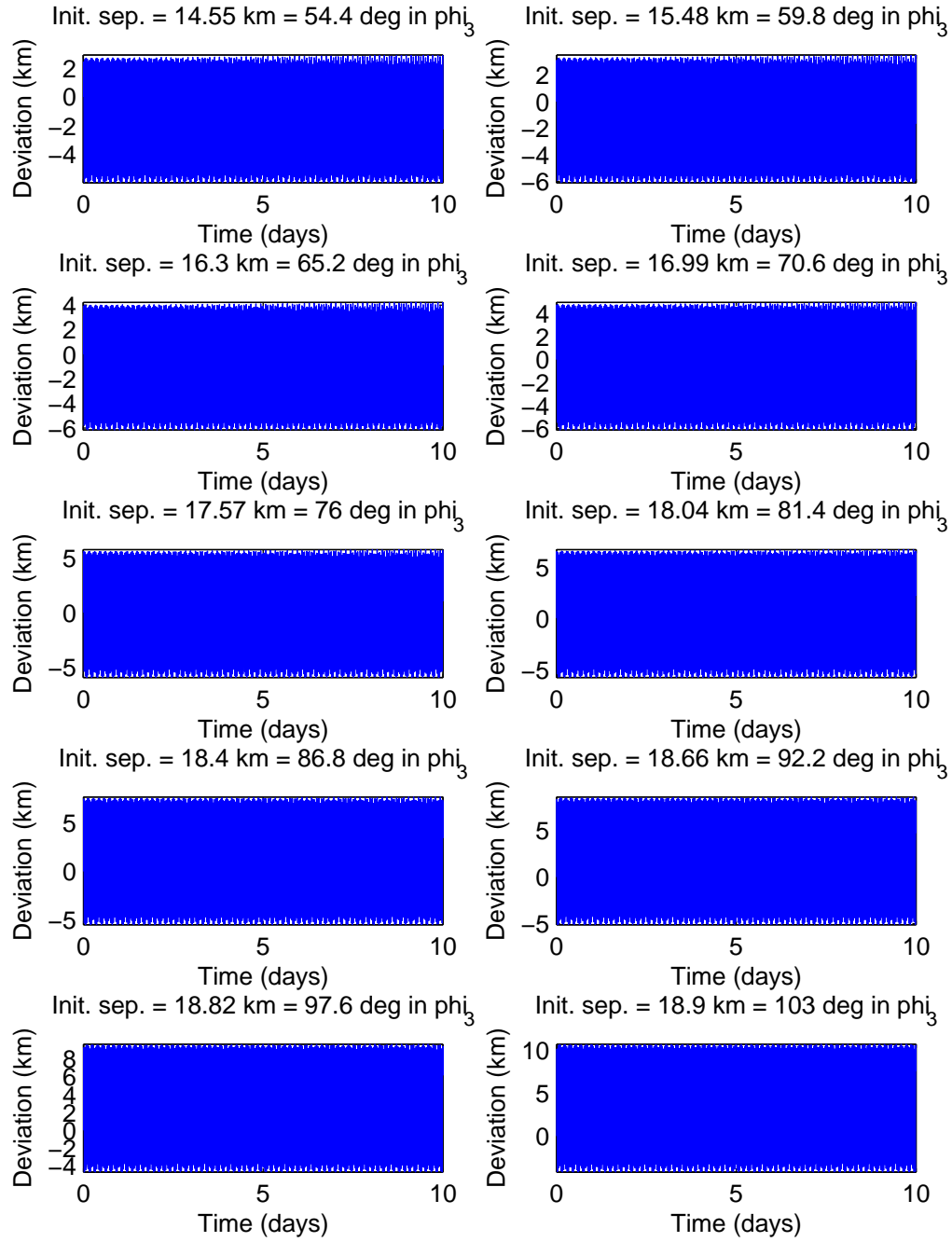
Figure C8.   Satellite separation deviation from initial value over 10 days after varying initial separations in φ_2 for 320km, 630km, $i = 15°$ (contd.)

Figure C9.   Secular drift between satellites over 10 days vs. initial φ_3 separation for 630km, $i = 15°$ orbit

Figure C10.   Secular drift (in percentage of initial separation) between satellites over 10 days vs. initial φ_3 separation for 320km, 630km, $i = 15°$ orbit

Figure C11.   Satellite separation deviation from initial value over 10 days after varying
initial separations in φ_3 for 630km, $i = 15°$ orbit

Init. sep. = 14.55 km = 54.4 deg in phi$_3$

Init. sep. = 15.48 km = 59.8 deg in phi$_3$

Init. sep. = 16.3 km = 65.2 deg in phi$_3$

Init. sep. = 16.99 km = 70.6 deg in phi$_3$

Init. sep. = 17.57 km = 76 deg in phi$_3$

Init. sep. = 18.04 km = 81.4 deg in phi$_3$

Init. sep. = 18.4 km = 86.8 deg in phi$_3$

Init. sep. = 18.66 km = 92.2 deg in phi$_3$

Init. sep. = 18.82 km = 97.6 deg in phi$_3$

Init. sep. = 18.9 km = 103 deg in phi$_3$

Figure C12.   Satellite separation deviation from initial value over 10 days after varying initial separations in φ_3 for 630km, $i = 15°$ orbit (contd.)
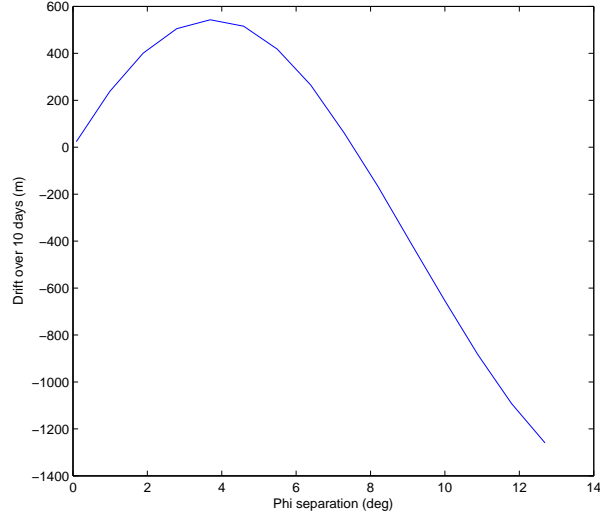
Figure D1.   Secular drift between satellites over 10 days vs. initial φ_1 separation for 630km, $i = 30°$ orbit

Table D1.   Drift results of initial displacements in φ_1 for 630km, 30° orbit

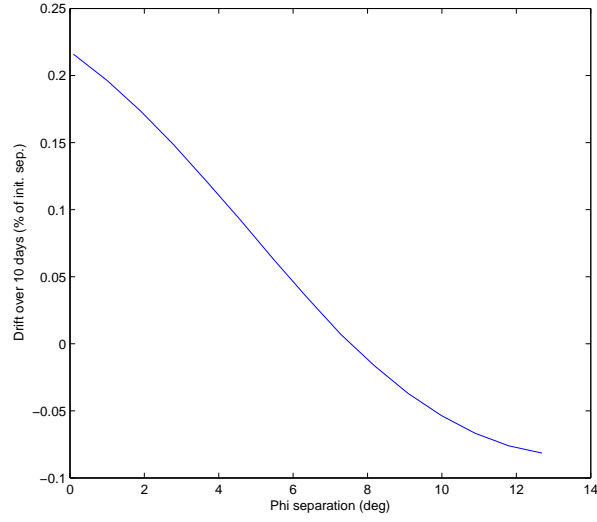| Torus angle	Initial sep. (deg)	Initial separation (m)	Oscillation amplitude (m)	Drift (m)	Drift (percent)
1	0.09	1.098e+004	18.44	23.72	0.216
1	0.99	1.208e+005	202.8	237.5	0.1966
1	1.89	2.307e+005	387.2	401	0.1739
1	2.79	3.405e+005	571.5	504.9	0.1483
1	3.69	4.503e+005	755.8	542.9	0.1206
1	4.59	5.601e+005	940.1	515.4	0.09203
1	5.49	6.698e+005	1124	418.6	0.0625
1	6.39	7.795e+005	1308	265.3	0.03403
1	7.29	8.891e+005	1492	60.94	0.006854
1	8.19	9.987e+005	1676	-164	-0.01643
1	9.09	1.108e+006	1860	-410.1	-0.03701
1	9.99	1.218e+006	2043	-651.9	-0.05353
1	10.89	1.327e+006	2225	-884.9	-0.06667
1	11.79	1.436e+006	2407	-1092	-0.07603
1	12.69	1.546e+006	2588	-1260	-0.08151

105

Figure D2.   Secular drift (in percentage of initial separation) between satellites over 10 days vs. initial φ_1 separation for 630km, $i = 30°$ orbit

Table D2.   Drift results of initial displacements in φ_2 for 630km, 30° orbit over 10 days

| Torus angle	Initial sep. (deg)	Initial separation (m)	Oscillation amplitude (m)	Drift (m)	Drift (percent)
2	0.36	4.403e+004	5694	-46.43	-0.1054
2	5.76	7.042e+005	9.105e+004	-474.3	-0.06735
2	11.16	1.363e+006	1.763e+005	-1955	-0.1434
2	16.56	2.019e+006	2.612e+005	-5070	-0.2512
2	21.96	2.67e+006	3.456e+005	-7336	-0.2748
2	27.36	3.315e+006	4.29e+005	-7749	-0.2338
2	32.76	3.953e+006	5.115e+005	-8775	-0.222
2	38.16	4.582e+006	5.93e+005	-1.133e+004	-0.2473
2	43.56	5.201e+006	6.731e+005	-1.326e+004	-0.2549
2	48.96	5.808e+006	7.517e+005	-1.392e+004	-0.2397
2	54.36	6.403e+006	8.286e+005	-1.479e+004	-0.2311
2	59.76	6.983e+006	9.037e+005	-1.615e+004	-0.2313
2	65.16	7.548e+006	9.768e+005	-1.758e+004	-0.2329
2	70.56	8.096e+006	1.048e+006	-1.955e+004	-0.2415
2	75.96	8.626e+006	1.116e+006	-2.179e+004	-0.2526
2	81.36	9.136e+006	1.182e+006	-2.301e+004	-0.2519
2	86.76	9.627e+006	1.246e+006	-2.346e+004	-0.2437
2	92.16	1.01e+007	1.307e+006	-2.451e+004	-0.2428
2	97.56	1.054e+007	1.364e+006	-2.633e+004	-0.2497
2	103	1.097e+007	1.419e+006	-2.791e+004	-0.2545

Table D3.   Drift results of initial displacements in φ_3 for 630km, 30° orbit over 10 days

| Torus angle	Initial sep. (deg)	Initial separation (m)	Oscillation amplitude (m)	Drift (m)	Drift (percent)
3	0.36	101.3	52.6	-1.822	-1.798
3	5.76	1594	841.3	32.33	2.028
3	11.16	3030	1628	84.19	2.779
3	16.56	4399	2411	64.15	1.459
3	21.96	5693	3188	-107.9	-1.895
3	27.36	6905	3960	-116	-1.679
3	32.76	8030	4722	192.3	2.395
3	38.16	9062	5472	284	3.134
3	43.56	9998	6210	290.5	2.906
3	48.96	1.084e+004	6936	-406.4	-3.751
3	54.36	1.158e+004	7648	-384.6	-3.323
3	59.76	1.222e+004	8342	-3.641	-0.0298
3	65.16	1.277e+004	9016	209.4	1.64
3	70.56	1.323e+004	9669	87.26	0.6597
3	75.96	1.36e+004	1.03e+004	297.4	2.186
3	81.36	1.391e+004	1.091e+004	-90.39	-0.6499
3	86.76	1.415e+004	1.15e+004	64.09	0.4529
3	92.16	1.435e+004	1.206e+004	334.6	2.332
3	97.56	1.451e+004	1.259e+004	-271.5	-1.872
3	103	1.465e+004	1.31e+004	70.78	0.4831
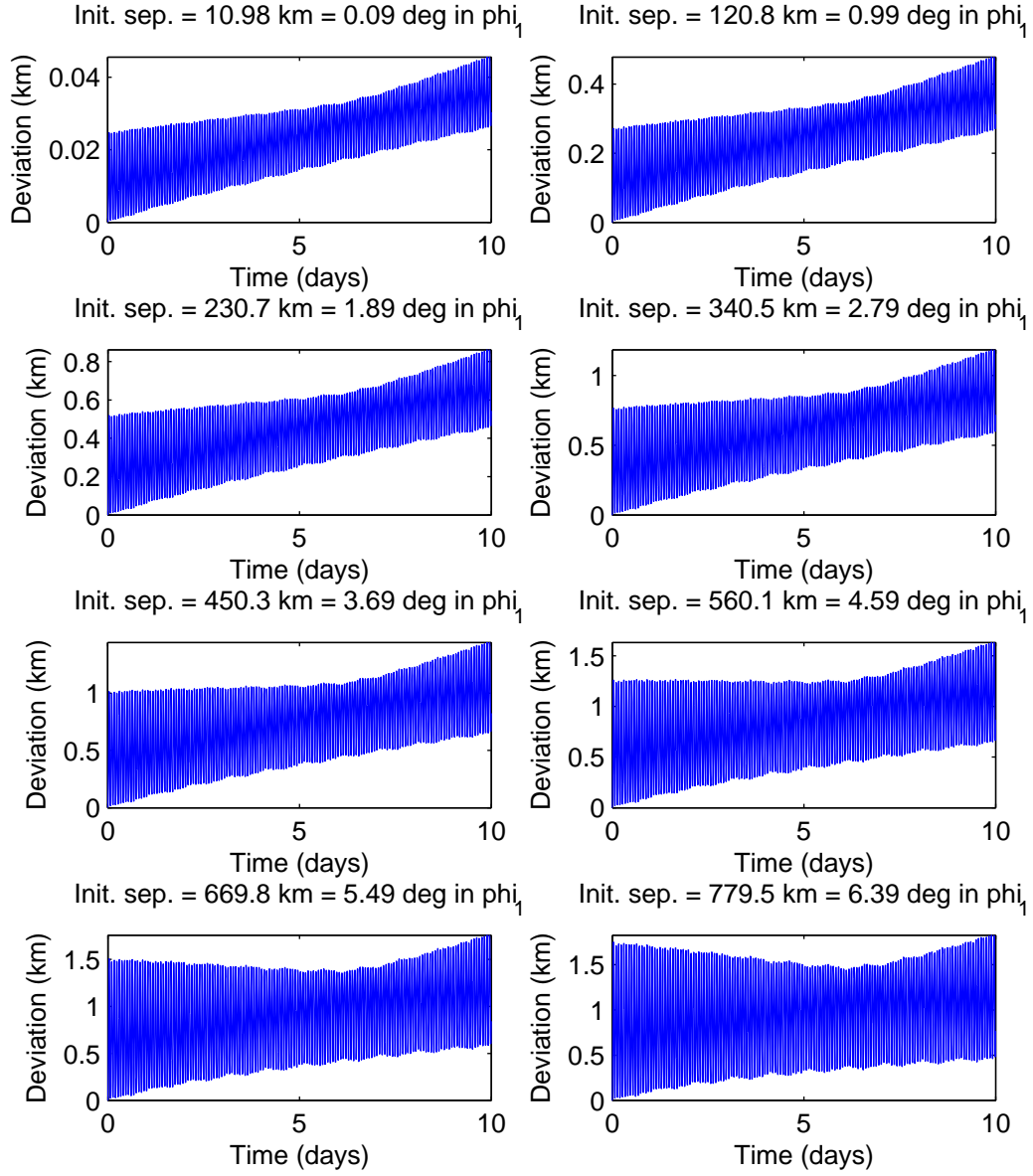
Figure D3.   Satellite separation deviation from initial value over 10 days after varying initial separations in φ_1 for 630km, $i = 30°$ orbit
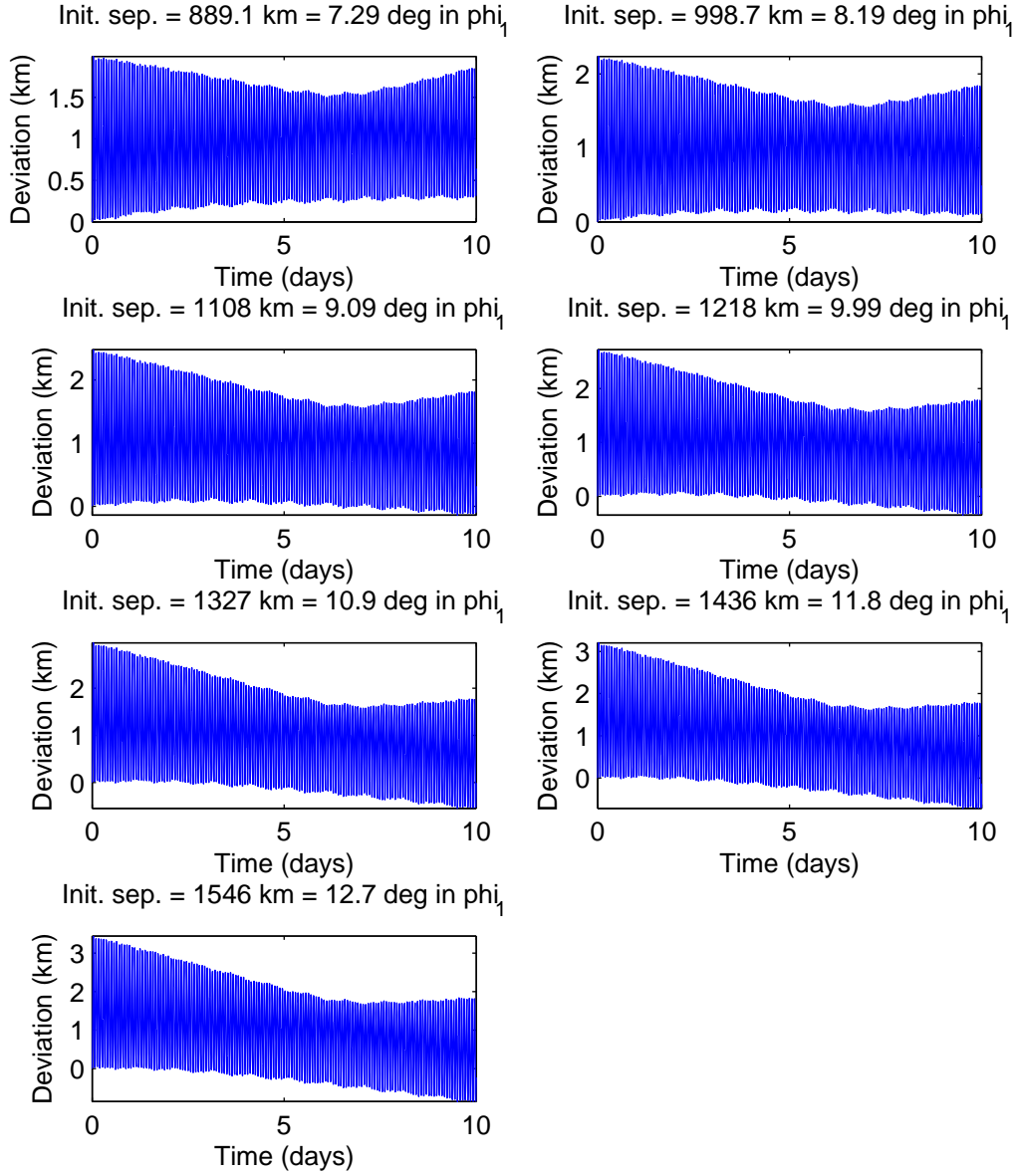
Figure D4. Satellite separation deviation from initial value over 10 days after varying initial separations in φ_1 for 630km, $i = 30°$ orbit (contd.)
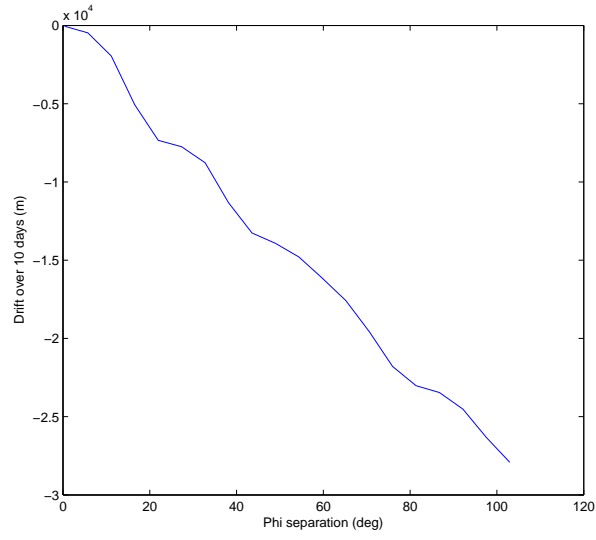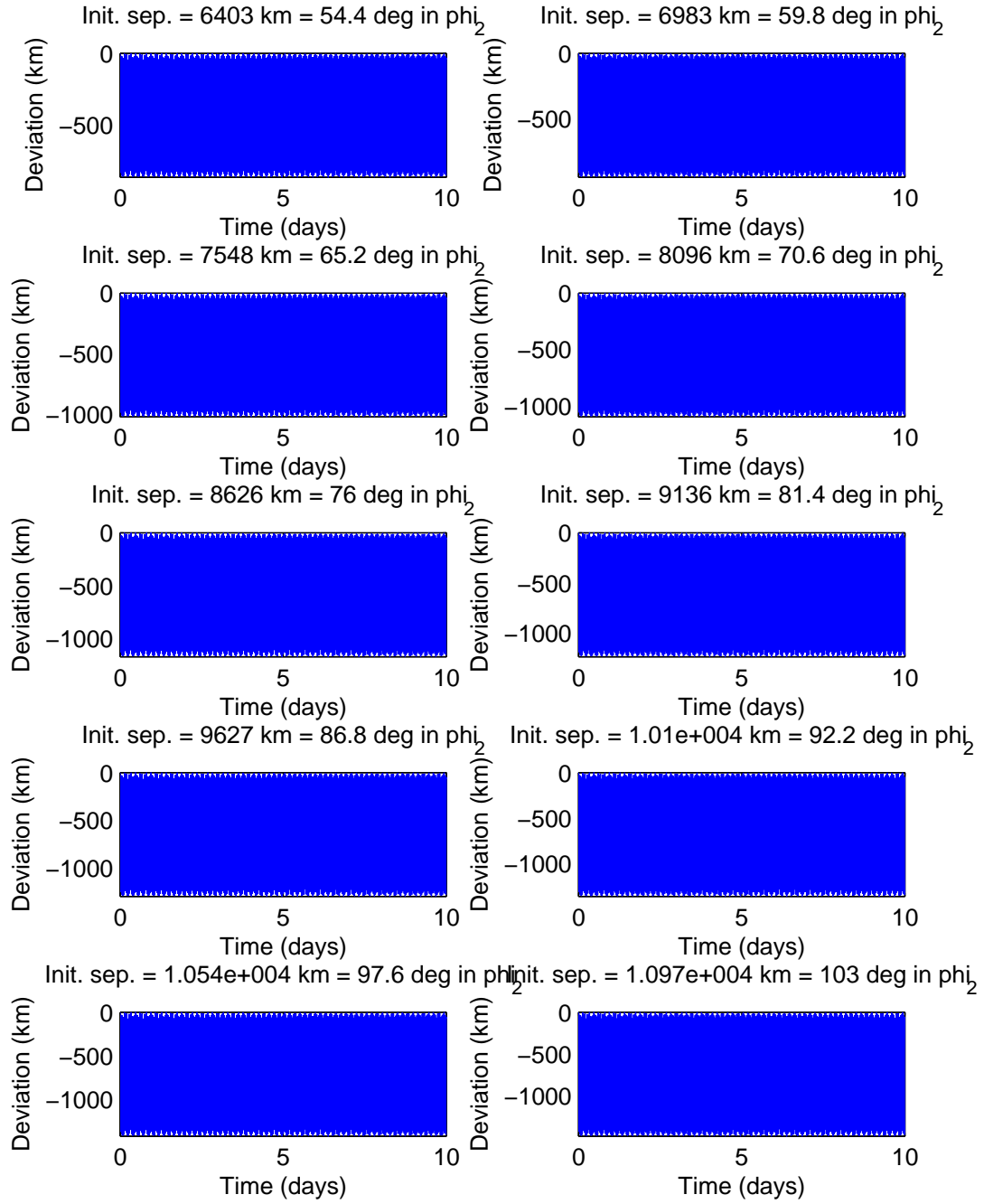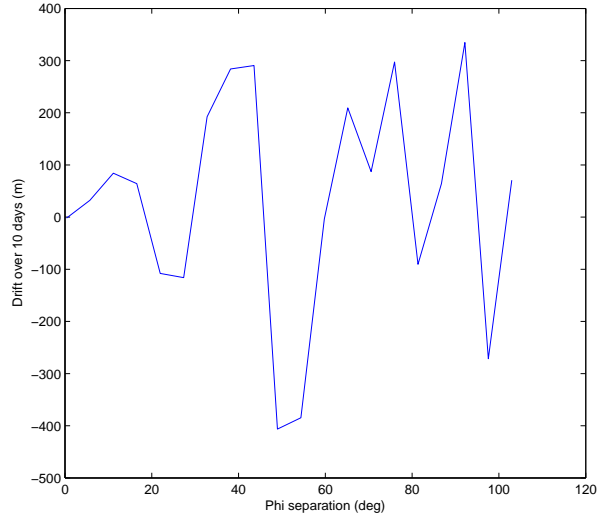
Figure D5.   Secular drift between satellites over 10 days vs. initial φ_2 separation for 630km, $i = 30°$ orbit
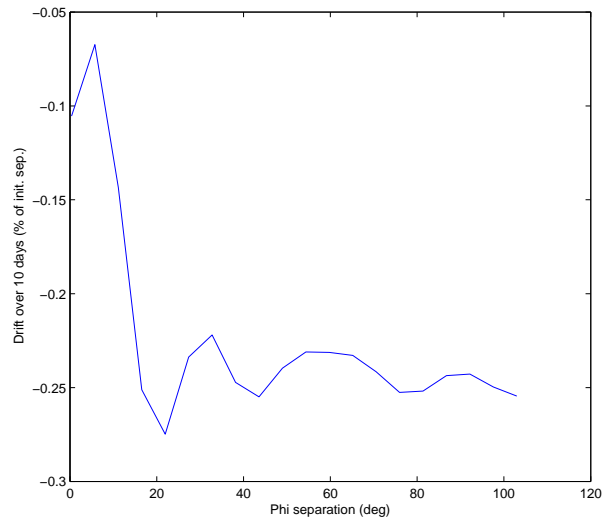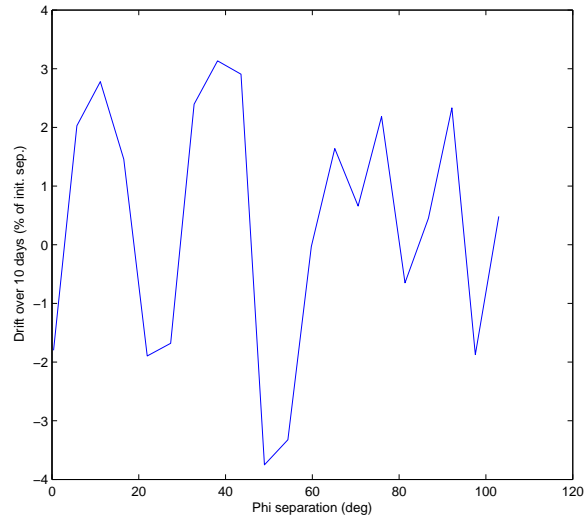

Figure D6.   Secular drift (in percentage of initial separation) between satellites over 10 days vs. initial φ_2 separation for 630km, $i = 15°$ orbit
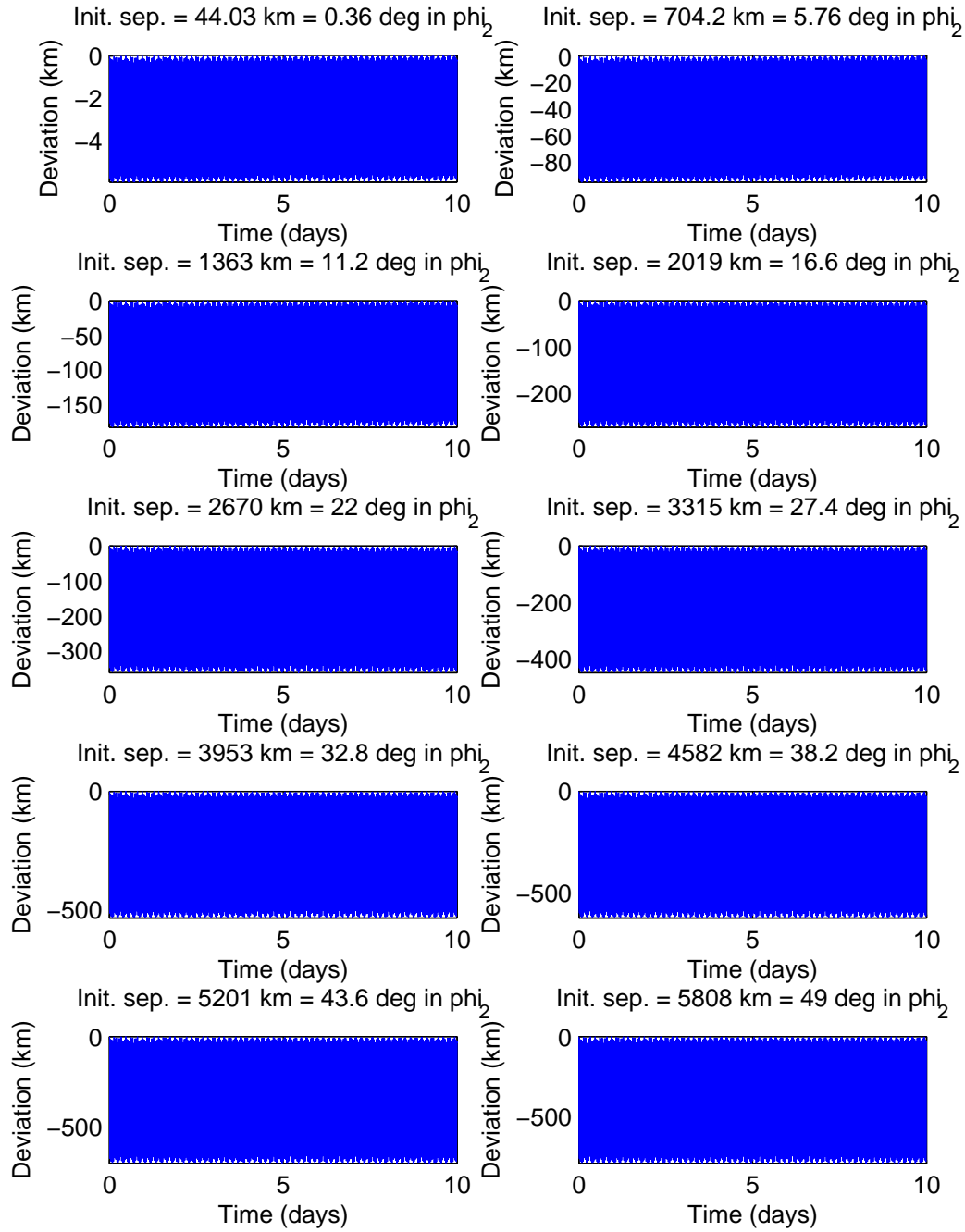
Figure D7. Satellite separation deviation from initial value over 10 days after varying initial separations in φ_2 for 630km, $i = 30°$ orbit

111

Figure D8.   Satellite separation deviation from initial value over 10 days after varying initial separations in φ_2 for 320km, 630km, $i = 30°$ (contd.)

112

Figure D9.   Secular drift between satellites over 10 days vs. initial φ_3 separation for 630km, $i = 30°$ orbit

Figure D10.   Secular drift (in percentage of initial separation) between satellites over 10 days vs. initial φ_3 separation for 320km, 630km, $i = 30°$ orbit
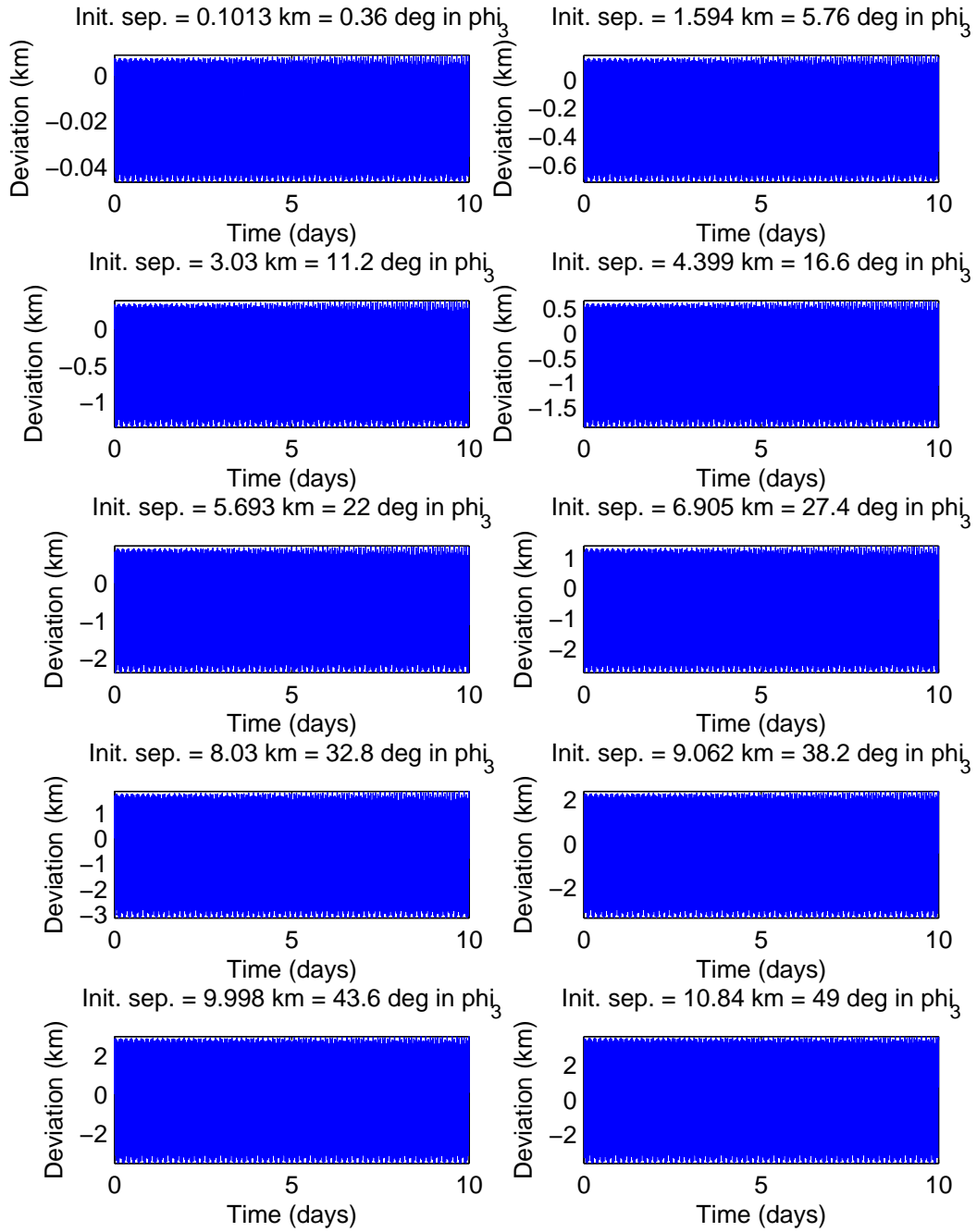
Figure D11.   Satellite separation deviation from initial value over 10 days after varying initial separations in φ_3 for 630km, $i = 30°$ orbit
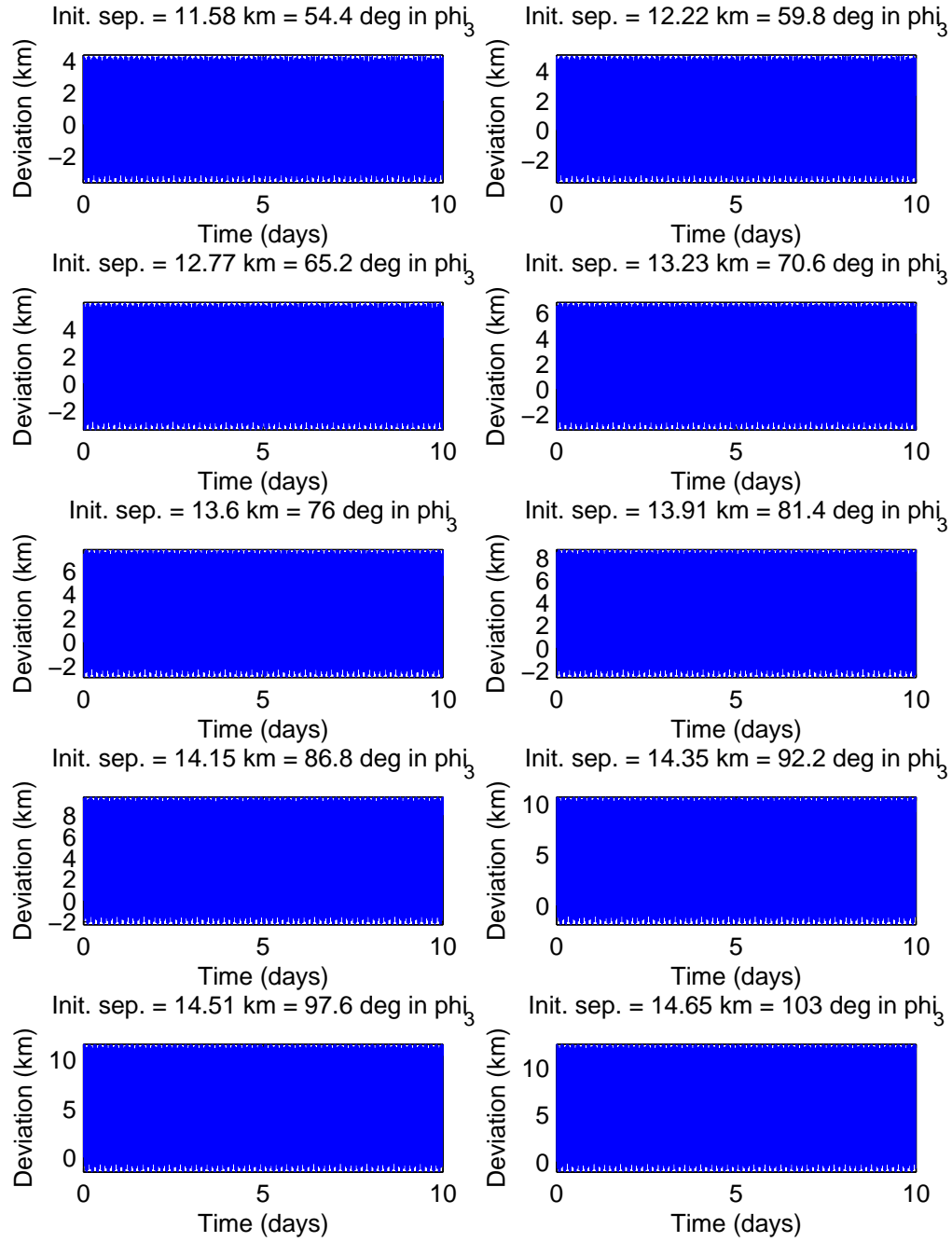
Figure D12.   Satellite separation deviation from initial value over 10 days after varying
initial separations in φ_3 for 630km, $i = 30°$ orbit (contd.)

115
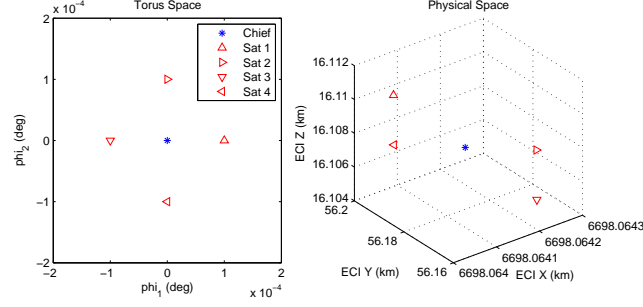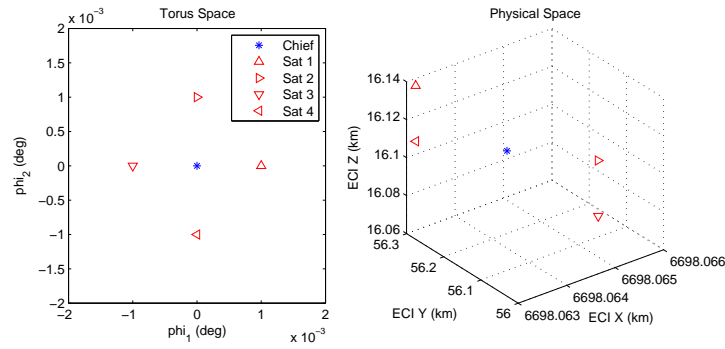
Figure E1.   Initial position in torus space and inertial cartesian space of satellite cluster for tight formation analysis in 320km, $15°$ orbit, $\delta\varphi = 0.0001°$
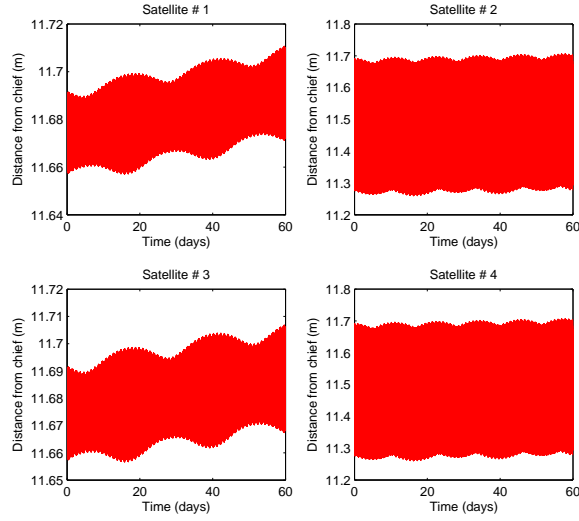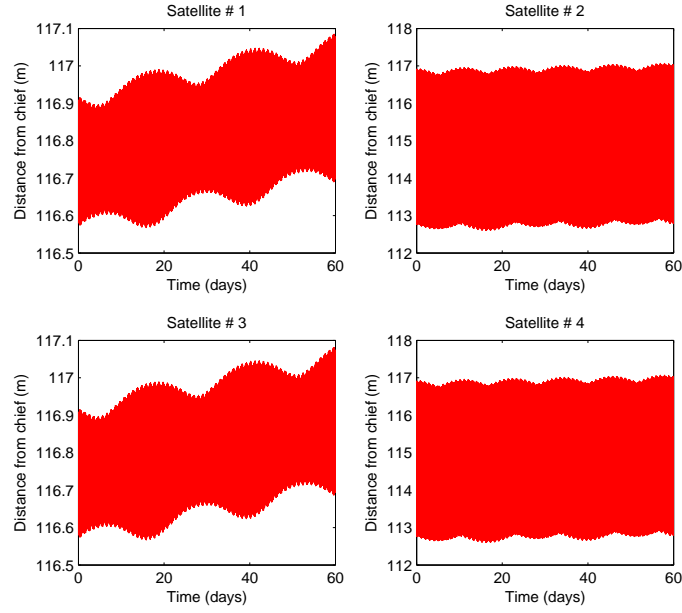

Figure E2.   Cluster distance from chief satellite for tight formation analysis in 320km, $15°$ orbit, $\delta\varphi_0 = 0.0001°$
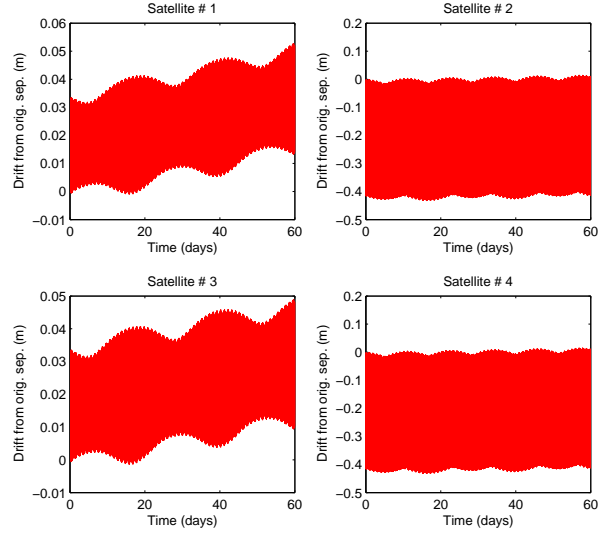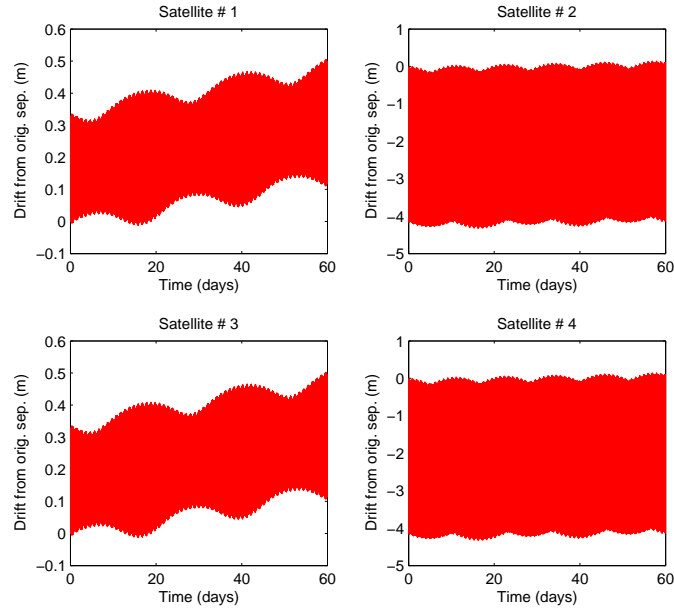
Figure E3.   Cluster drift from initial separations for tight formation analysis in 320km, 15° orbit, $\delta\varphi_0 = 0.0001°$

Figure E4.   Initial position in torus space and inertial cartesian space of satellite cluster for tight formation analysis in 320km, 15° orbit, $\delta\varphi = 0.001°$

117

Figure E5. Cluster distance from chief satellite for tight formation analysis in 320km, 15° orbit, $\delta\varphi_0 = 0.001°$

Figure E6. Cluster drift from initial separations for tight formation analysis in 320km, 15° orbit, $\delta\varphi_0 = 0.001°$
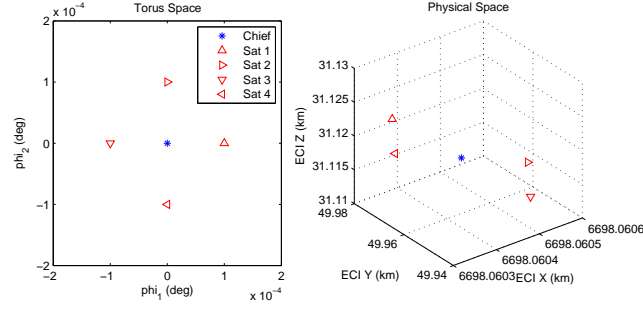
Figure E7.   Initial position in torus space and inertial cartesian space of satellite cluster for tight formation analysis in 320km, 30° orbit, $\delta\varphi = 0.0001°$
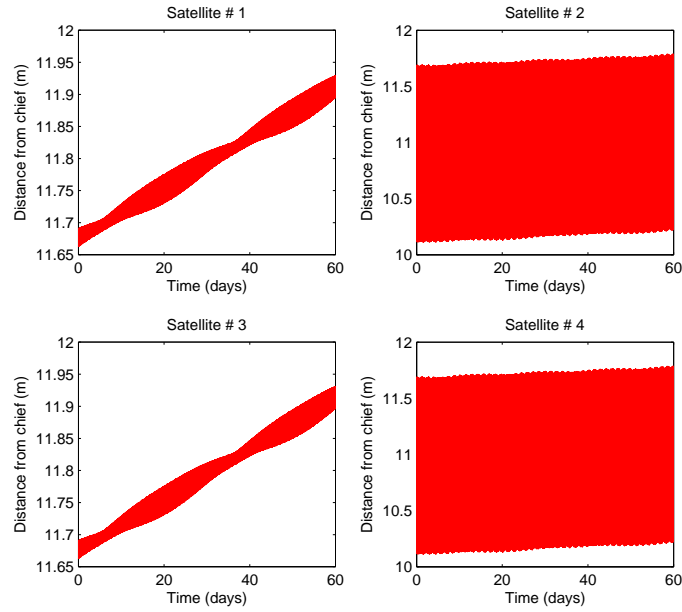

Figure E8.   Cluster distance from chief satellite for tight formation analysis in 320km, 30° orbit, $\delta\varphi_0 = 0.0001°$

119
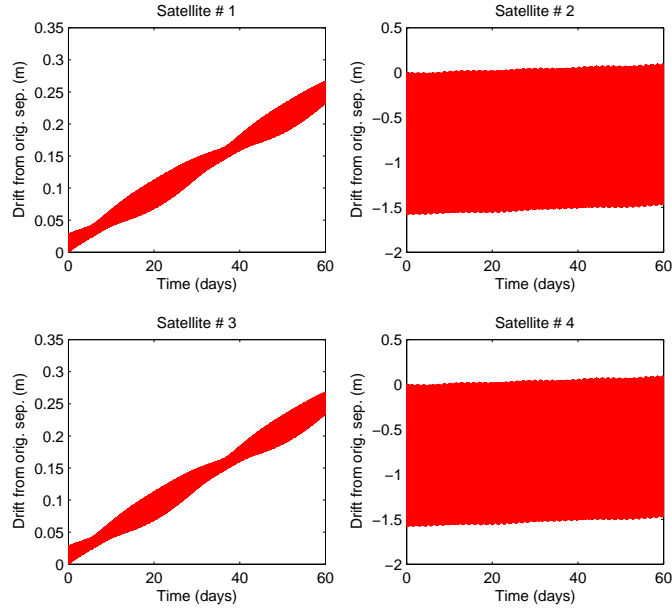
Figure E9.   Cluster drift from initial separations for tight formation analysis in 320km, 30° orbit, $\delta\varphi_0 = 0.0001°$
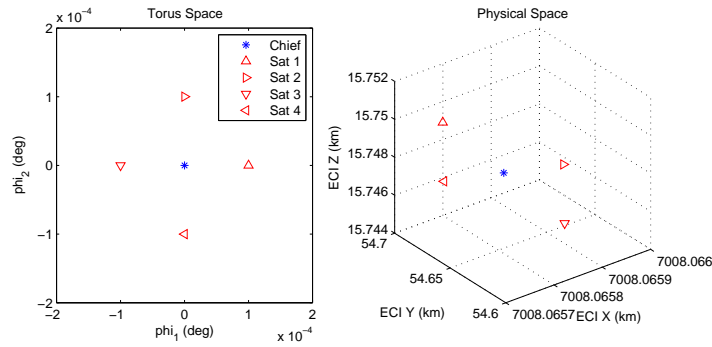

Figure E10.   Initial position in torus space and inertial cartesian space of satellite cluster for tight formation analysis in 630km, 15° orbit, $\delta\varphi = 0.0001°$

Figure E11.   Cluster distance from chief satellite for tight formation analysis in 630km, 15° orbit, $\delta\varphi_0 = 0.0001°$

Figure E12.   Cluster drift from initial separations for tight formation analysis in 630km, 15° orbit, $\delta\varphi_0 = 0.0001°$

Figure E13.   Initial position in torus space and inertial cartesian space of satellite cluster for tight formation analysis in 630km, 30° orbit, $\delta\varphi = 0.001°$
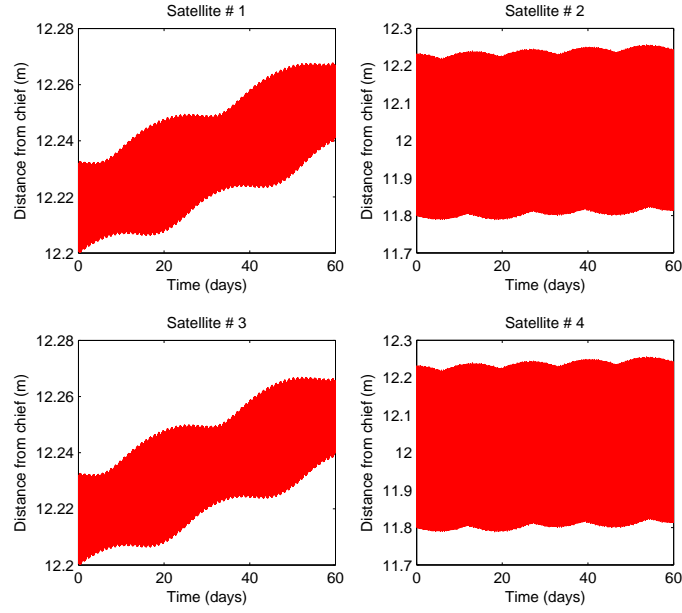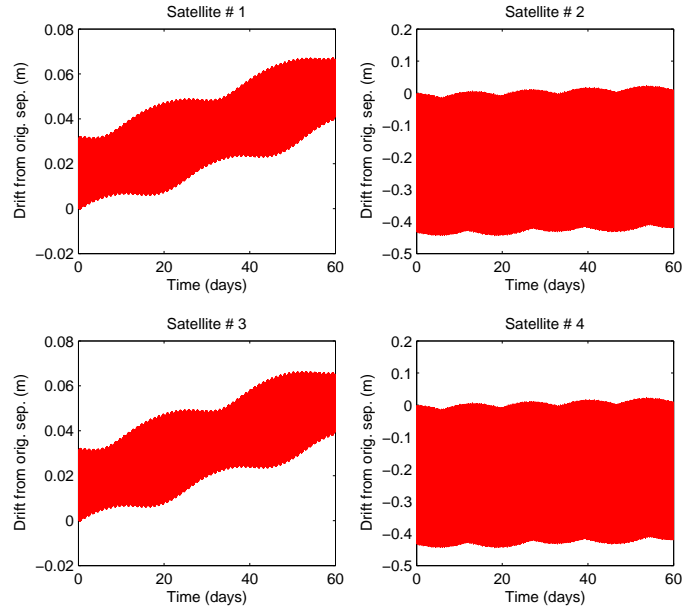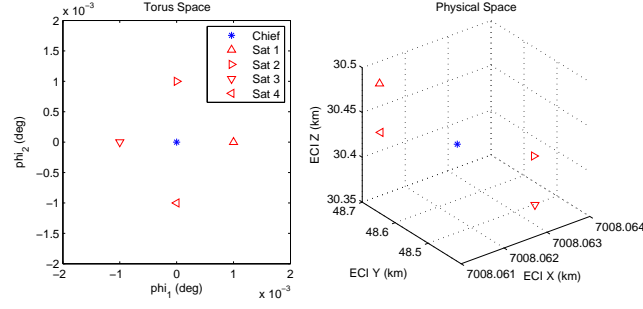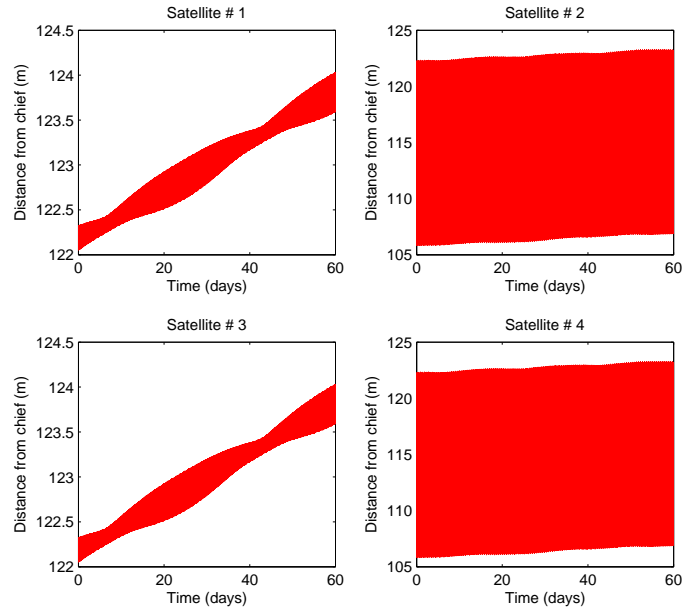

Figure E14.   Cluster distance from chief satellite for tight formation analysis in 630km, 30° orbit, $\delta\varphi_0 = 0.001°$

122
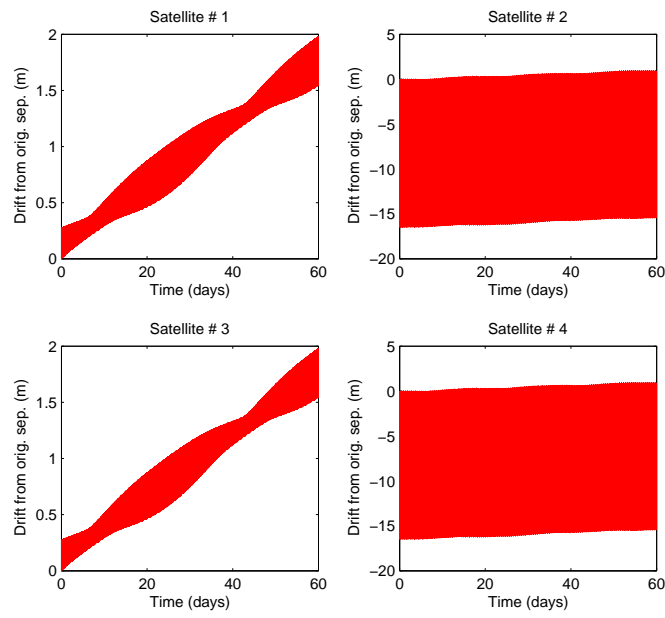
Figure E15.   Cluster drift from initial separations for tight formation analysis in 630km, 30° orbit, $\delta\varphi_0 = 0.001°$

Bibliography

1. Arnold, V. "Proof of Kolmogorov's Theorem on the Preservation of Quasi-Periodic Motions Under Small Perturbations of the Hamiltonian," *Rus. Math. Surv.*, *18(N6)*:9–36 (1963).

2. Bainum, P. "Breakwall Memorial Lecture: Review of Astrodynamics, 1958-2001 - A Personal Perspective." *IAF Paper 01-A201*. Number 52nd in IAF, International Astronautical Conference. Oct 1-5 2001. Toulouse, France.

3. Celletti, Alessandra and Luigi Chierchia. "KAM Stability Estimates in Celestial Mechanics," *Planet. Space Sci.*, *46(11/12)*:1433–1440 (1998).

4. Celletti, Alessandra and Luigi Chierchia. "KAM Stability for a Three-Body Problem of the Solar System," *Z. angew. Math. Phys.*, *57*:33–41 (2006).

5. Gabella, W. E., R. D. Ruth and R. L. Warnock. "Beam Dynamics with the Hamilton-Jacobi Equation." *Proceedings of the 13th IEEE Particle Accelerator Conference, Chicago, Illinois*. 20-23 Mar 1989. SLAC-PUB-4927.

6. Ginn, Jeffery Scott. *Spacecraft Formation Flight: Analysis of the Perturbed J2-Modified Hill-Clohessy-Wiltshire Equations*. MS thesis, The University of Texas at Arlington, 2006.

7. Kaasalainen, M. and J. Binney. "Torus Construction in Potentials Supporting Different Orbit Families," *Mon. Not. R. Astr. Soc.*, *268*:1033 (1994).

8. Kolmogorov, A. N. "On the Conservation of Conditionally Periodic Motions Under Small Perturbations of the Hamiltonian," *Dokl. Akad. Nauk. SSR*, *98*:527–530 (Jan 1954).

9. Laskar, Jaques. "Frequency Map Analysis and Quasiperiodic Decompositions." *Proceedings of Porquerolles School*. 1–31. Sept 1990.

10. Laskar, Jaques. "Introduction to Frequency Map Analysis." *Hamiltonian Systems with Three or More Degrees of Freedom* edited by C. Simo, 134–150, Kluwer Academic Publishers, 1999.

11. Little, Bryan D. *Application of KAM Theorem to Earth Orbiting Satellites*. MS thesis, Air Force Institute of Technology, 2009.

12. Martin, M. and S. Kilberg. "TECHSAT 21 and Revolutionizing Space Missions using Microsatellites." *American Institute of Aeronautics and Astronautics*. 2001. SSC01-1-3.

13. McGill, Colin and James Binney. "Torus Construction in General Gravitational Potentials," *Mon. Not. R. Astr. Soc.*, *244*:634–645 (1990).

14. Meirovitch, Leonard. *Methods Of Analytical Dynamics* (Dover Edition). McGraw-Hill Book Company, NY, 1970,1998.

15. Moser, J. K. "On Invariant Curves of Area Preserving Mappings of an Annulus," *Nachr. der Akad. Wiss. Göttingen, Math. Phys.*, *Kl. II*:1–20 (Jan 1962).

16. Prince, P.J. and J.R. Dorman. "High order embedded Runge-Kutta formulae," *J.Comp. Appl. Math.*, *7*:67–75 (1981).

17. Schaub, H. and K. T. Alfriend. "J2-Invariant Relative Orbits for Spacecraft Formations," *Celestial Mechanics and Dynamical Astronomy*, *79*:77–95 (2001).

18. Schweighart, S. A. and R. J. Sedwick. "Development and Analysis of a High-Fidelity Linearized J2 Model for Satellite Formation Flying." *AIAA Space 2001 - Conference and Exposition, Albuquerque, NM*. Aug. 28-30 2001.

19. Vallado, David A. *Fundamentals of Astrodynamics and Applications* (2nd Edition). Microcosm Press and Kluwer Academic Publishers, 2001.

20. Warnock, R. L., R. D. Ruth and K. Ecklund. "Construction and Fourier Analysis of Invariant Surfaces From Tracking Data." *Proceedings of the 13th IEEE Particle Accelerator Conference, Chicago, Illinois*. 20-23 Mar 1989. SLAC-PUB-4927.

21. Warnock, Robert. "Close Approximations to Invariant Tori in Nonlinear Mechanics," *Physical Review Letters*, *66*(14):1803–1806 (Apr. 8 1991).

22. Warnock, Robert and Ronald Ruth. "Stability of Nonlinear Hamiltonian Motion for a Finite But Very Long Time," *Physical Review Letters*, *66*(8):990–993 (Feb. 25 1991).

23. Wiesel, William E. *Modern Astrodynamics* (1st Edition). Aphelion Press, 2003.

24. Wiesel, William E., "Earth Satellellite Orbits as KAM Tori." Presented as paper AAS 07-423 at the AAS/AIAA Astrodynamics Specialist Conference, August 2007.

25. Wiesel, William E. "KAM Tori Construction Algorithms." Unpublished, 2008.

REPORT DOCUMENTATION PAGE

Form Approved
OMB No. 0704–0188

1. REPORT DATE (DD–MM–YYYY)	2. REPORT TYPE	3. DATES COVERED (From — To)
10 09 2009	Master's Thesis	01 Oct 07--10 Sep 09

4. TITLE AND SUBTITLE

Formation Flight of Earth Satellites on KAM Tori

5a. CONTRACT NUMBER

5b. GRANT NUMBER

5c. PROGRAM ELEMENT NUMBER

6. AUTHOR(S)

Craft, Christopher T., 1st Lt, USAF

5d. PROJECT NUMBER
#

5e. TASK NUMBER

5f. WORK UNIT NUMBER

7. PERFORMING ORGANIZATION NAME(S) AND ADDRESS(ES)
Air Force Institute of Technology
Graduate School of Engineering and Management (AFIT/ENY)
2950 Hobson Way
WPAFB OH 45433-7765

8. PERFORMING ORGANIZATION REPORT NUMBER

AFIT/GA/ENY/09-S01

9. SPONSORING / MONITORING AGENCY NAME(S) AND ADDRESS(ES)

INTENTIONALLY LEFT BLANK

10. SPONSOR/MONITOR'S ACRONYM(S)

11. SPONSOR/MONITOR'S REPORT NUMBER(S)

12. DISTRIBUTION / AVAILABILITY STATEMENT
APPROVED FOR PUBLIC RELEASE; DISTRIBUTION UNLIMITED

13. SUPPLEMENTARY NOTES
This material is declared a work of the U.S. government and is not subject to copyright protection in the United States.

14. ABSTRACT

Kolmogorov, Arnold and Moser (KAM) theory provides that orbits of satellites whose dynamics are representable by an integrable Hamiltonian plus a small, real perturbation lie on tori in phase space and remain on the KAM tori for all time, unless acted upon by a non-conservative force. A refined technique for constructing KAM tori for Earth-orbiting satellites is developed and implemented using numerically integrated orbital data for hypothetical satellites and involving methods of Fourier analysis and spectral decomposition. Definition of satellite formations on the KAM tori is performed and analyses conducted to investigate both constellations with large separations and clusters with small separations. Cluster formations with physical secular drift rates on the order of nanometers to micrometers per second are obtained. A brief discussion of effects of non-conservative forces (such as atmospheric drag) on KAM tori is given.

15. SUBJECT TERMS
KAM, torus, tori, satellite, formation, cluster, constellation

16. SECURITY CLASSIFICATION OF:			17. LIMITATION OF ABSTRACT	18. NUMBER OF PAGES	19a. NAME OF RESPONSIBLE PERSON
a. REPORT	b. ABSTRACT	c. THIS PAGE	UU	145	William E. Wiesel, Ph. D.; Instructor, AFIT
U	U	U			19b. TELEPHONE NUMBER (Include Area Code) (937)255-3636 x4312; william.wiesel@afit.edu

Standard Form 298 (Rev. 8–98)
Prescribed by ANSI Std. Z39.18